分类号_____ 密级_____

UDC _____ 编号_____

华中师范大学

博士学位论文

200GeV 金金碰撞中两粒子方位角关联对反应平面的依赖性

学位申请人姓名：冯傲奇

申请学位专业方向：粒子物理与原子核物理

指导教师姓名：吴元芳、王富强

博士学位论文
DOCTORAL DISSERTATION

博士学位论文

200GeV 金金碰撞中两粒子方位角关联对反应平面的依赖性

论文作者：冯傲奇

指导老师：吴元芳　教　授

王福强　副教授

学科专业：粒子物理与原子核物理

研究方向：相对论重离子碰撞

华中师范大学物理科学与技术学院

2008 年 5 月

博士学位论文

DOCTORAL DISSERTATION

Central China Normal University

Wuhan, CHINA

Di-hadron Azimuthal Correlations Relative to Reaction Plane in Au + Au Collisions at $\sqrt{s_{NN}}$ = 200 GeV

A dissertation submitted

for the degree of

Doctor of Philosophy in Physics

by

Aoqi Feng

Co-supervisors: Yuanfang Wu, Fuqiang Wang

2008

华中师范大学学位论文原创性声明和使用授权说明

原创性声明

本人郑重声明：所呈交的学位论文，是本人在导师指导下，独立进行研究工作所取得的研究成果。除文中已经标明引用的内容外，本论文不包含任何其他个人或集体已经发表或撰写过的研究成果。对本文的研究做出贡献的个人和集体，均已在文中以明确方式标明。本声明的法律结果由本人承担。

作者签名:　　日期:　　年　月　日

学位论文版权使用授权书

本学位论文作者完全了解学校有关保留、使用学位论文的规定，即：学校有权保留并向国家有关部门或机构送交论文的复印件和电子版，允许论文被查阅和借阅。本人授权华中师范大学可以将本学位论文的全部或部分内容编入有关数据库进行检索，可以采用影印、缩印或扫描等复制手段保存和汇编本学位论文。同时授权中国科学技术信息研究所将本学位论文收录到《中国学位论文全文数据库》，并通过网络向社会公众提供信息服务。

作者签名:　　导师签名:
日期:　　年　月　日　　日期:　　年　月　日

本人已经认真阅读“CALIS 高校学位论文全文数据库发布章程”,同意将本人的学位论文提交“CALIS 高校学位论文全文数据库”中全文发布,并可按“章程”中的规定享受相关权益。同意论文提交后滞后：□半年；□一年；□二年发布。

作者签名:　　导师签名:
日期:　　年　月　日　　日期:　　年　月　日

博士学位论文

DOCTORAL DISSERTATION

Dedicated to my dear father and mother.

谨献给我最亲爱的父母！

摘 要

夸克和胶子被认为是物质最基本的组成单元之一。量子色动力学（QCD）则是描述夸克和胶子之间强相互作用的一个成功的规范理论。QCD有两个显著的基本特征：1)渐进自由：横动量交换越大或夸克之间的距离越小，夸克之间的相互作用越弱；2)夸克禁闭：夸克只能禁闭在强子物质内，目前还没有观测到孤立的夸克。格点QCD的计算表明在高温度或高密度的环境里，普通的强子气体会转变成为另外一种夸克胶子解禁闭的QCD物质相－－夸克胶子等离子体（QGP）。位于美国布鲁克海汶国家实验室的相对论重离子对撞机（RHIC）通过对撞两束接近光速的金离子来期望产生这种高能量密度的物质，以模拟宇宙大爆炸后微秒量级左右的物质组成。经过几年的运行和实验数据分析，目前为止观察到的实验现象－－强椭圆流和喷注焠火－－预示着RHIC产生的物质性质极类似于一种由强相互作用夸克胶子等离子体组成的理想流体。在研究RHIC重离子碰撞所产生的这种物质的性质中，从喷注碎裂产生的高横动量(p_T) 粒子是一种理想的探针。通常人们通过对粒子的单举分布产额以及这些粒子的强子对关联的研究来探测RHIC所产生的物质的性质。然而，在这两种方法中，由于单举粒子产额的研究对RHIC所产生的物质核心部分不很敏感，而强子对关联的测量则由于多引入了一个粒子的信息，将为我们研究产生物质的特性提供更为丰富更有价值的信息。

RHIC上重要的有关强子对关联的测量包括：1）对两个高横动量粒子的方位角关联的测量。其中一个高横动量的粒子称作“触发粒子”（trigger particle），它被认为是来自于喷注中的一个横动量很高的粒子，因此它的方向可以认为就是喷注轴的方向。另外的一个横动量相对低一些的粒子称作“伴随粒子”（associated particles)，它们可能来自于喷注中的其他粒子（信号），也可能来自于各向异性流或者共振态衰变（均为背景）。通过测量触发粒子和伴随粒子的方位角关联并扣除背景粒子的贡献，就可以得到来自于喷注的关联结果。这一测量发现：在金金的中心碰撞中，高横动量粒子在背对背方向的关联消失了（伴随粒子产额压低）。而这一压低现象在基本的质子质子对撞中却没有发现。这说明，双喷注中背向（与触发粒子背对背的方向）的喷注在金金的中心对撞中消失了。这可以用喷注淬火理论来解释：背向的喷注在经

过金金中心碰撞所产生的高温高密物质时，由于胶子辐射损失了大量的能量，因此不能被观测到。这一现象被认为是喷注淬火理论的一个重要的证据。2)对较低横动量伴随粒子与一个高横动量触发粒子的角关联的研究。这一研究发现在金金中心碰撞中，背向的低横动量粒子的分布比在质子质子碰撞中要变宽很多。这一结果与预期的背向喷注在介质中的能量损失是一致的：来自于喷注的背对背方向的高横动量粒子，在穿过RHIC金金碰撞产生的高温高密物质时，损失了能量，并且这些损失的能量“传递”给了低横动量的粒子，因此使得背对背方向上较低横动量强子对关联的产额分布变宽。3）RHIC实验的STAR实验组第一次测量了强子对关联相对于反应平面的依赖。并发现背向高横动量粒子产额在垂直于反应平面的方向上有较强的压低，而在靠近反应平面的方向上却没有观测到强压低现象。这一结果似乎暗示了喷注的能量损失可能与路径长度有关：在靠近反应平面的方向，背对背方向的喷注穿过物质时所经过路径比较短，能量损失较少；而在垂直于反应平面的方向上穿过的路径则要长很多，因此能量损失也大。4）“脊”的发现：最近STAR实验组在研究二维的$\Delta\phi \times \Delta\eta$（触发粒子和伴随粒子方位角夹角以及赝快度间隔）的强子对关联时发现了一个新现象：在质子质子碰撞中，触发粒子的近端，小的$\Delta\phi$和$\Delta\eta$区间上有关联，从图像上则表现为在触发粒子近端的一个峰。它是来自于喷注的。而在金金碰撞中，这一关联在$\Delta\eta$方向上的很大范围内都存在，从图像上看则表现为在小的$\Delta\phi$, 大的$\Delta\eta$区间有一个很宽的平台。而来自于喷注的峰则位于这一平台之上。这一二维图像很像一个大的山脉，一个山峰立于一个平坦的山脊之上。因此，人们把在$\Delta\eta$方向上的这一长程关联称为“脊”（ridge）。对于脊的产生机制目前尚不清楚仍在探索之中。

在这篇论文中，通过分析RHIC实验上STAR探测器获取的大样本的质心系能量为200GeV金金最小无偏碰撞和中心碰撞数据，我们测量了强子对关联并研究它随高横动量触发粒子相对于反应平面方位角的变化。同时我们也分析了最小无偏的200GeV氘金碰撞数据中的强子对关联，其结果将和金金碰撞的结果进行比较。

我们根据触发粒子相对于反应平面的方位角方向($\phi_s = |\phi^{trig} - \Psi_{EP}|$)把横向的$\phi$ 平面均分成6个小区间，然后分别研究强子对关联在触发粒子落入每个小区间时的分布，从而更细致地研究强子对关联对介质路径长度的依赖性。反应平面通过STAR标准的重建方法得到，但是落在与关联粒子横动量p_T^{assoc}相同p_T区间的粒子将不被用做

反应平面的重建以避免自相关。高阶的各向异性流v_4的贡献在以前的强子对关联的背景研究中都没有考虑。而这里我们通过研究表明它的贡献在相对于反应平面强子对关联的背景研究中不可忽略。因此，我们修正了流本底的计算公式，把v_4的贡献考虑进去。对于流参数的选取，我们采用了STAR通过反应平面方法和4粒子累积关联方法得到的结果的平均值。两者之间的差别是系统误差的主要来源。流本底通过改进的Zero-Yield-At-Minumum(ZYAM)方法来归一化。在每个p_T^{assoc}和ϕ_s区间分别计算流本底，然后从原始的强子关联分布中扣除流的贡献，从而得到我们感兴趣的与喷注相关的强子对关联分布。我们分别研究了20-60%中心度和0-5%中心度的金金碰撞数据，以及最小无偏的氘金碰撞的数据。对于触发粒子近端关联分布的研究，我们分别计算了在大的和小的$\Delta\eta$区间（被认为分别来自于脊的贡献以及脊和喷注共同贡献）中强子对关联的分布，从而来区分在近端关联中喷注和脊的贡献，并研究它们随ϕ_s的变化趋势。在这里，我们把离触发粒子比较近的方向（$\Delta\phi \sim 0°$）称为近端（near-side），把背对着触发粒子的方向（$\Delta\phi \sim 180°$）称为背端（away-side）.

研究发现，相比于来自最小无偏的氘金数据的关联结果，金金碰撞中强子对关联的近端和背端分布都受到很强的来自于RHIC所产生的介质的修正。这种修正依赖于触发粒子相对于反应平面的方向以及关联粒子的横动量p_T^{assoc}。强子对关联分布随ϕ_s的变化趋势在5%的中心碰撞和20-60%非中心碰撞中比较相似，但在20-60%中心度碰撞中变化比较得快。

从触发粒子在反应平面方向到它垂直于反应平面方向，强子对关联的背向分布逐渐变宽，同时它也随p_T^{assoc}的增加而变宽。在20-60%中心度碰撞中，当触发粒子沿着反应平面的方向时，背向关联的分布呈现一个单峰结构，随着触发粒子偏向垂直于反应平面方向时，单峰结构逐渐变成越来越明显的双峰结构。在0-5% 中心碰撞中，即使在触发粒子沿着反应平面的方向，背向关联的分布已经呈现出双峰结构，而且双峰结构也随着触发粒子偏向垂直于反应平面方向时而变得越来越明显。这种背向结构的修正趋势反映出路径长度对于硬散射出来的背向部分子在穿过介质时的修正的重要性。这在性质上与喷注淬火理论的预言一致。

近端关联分布随着触发粒子沿着反应平面变化到垂直于反应平面时，它的关联幅度会降低。而通过把近端关联分成脊和喷注的关联来分别研究时，发现这种降低几乎

全是来自于脊的产额的随着ϕ_s 的增加而减少。而喷注的产额则基本不随ϕ_s变化（或者可以认为略微随着ϕ_s增加而增加）。在20-60%中心度中，脊的产额在垂直于反应平面方向上几乎降为0，而在0-5%中心碰撞中，从反应平面内变化到垂直于反应平面的各个角度，脊的产额都比较的显著。在20-60%中心度中，从反应平面内变化到垂直于反应平面时，喷注的产额有略微的增加。这些现象似乎表明如下一个脊产生图像：近端的喷注，在沿着反应平面的方向上与介质发生较强的相互作用，损失了一定的能量，从而使得观测到的喷注产额减少，并且生成了大$\Delta\eta$范围内的的脊；而在垂直于反应平面的方向上，喷注受到的介质影响最小，从而产生的脊也较少。对于0-5%中心碰撞，喷注和脊的产额随ϕ_s的变化趋势基本相似，只是由于初始碰撞时的几何结构更接近圆形，于是在各个ϕ_s 角度上都有一定的脊的贡献，喷注和脊的幅度在各个ϕ_s角度上的变化也小很多。

这篇论文中的主要的结果是选择触发粒子横动量$3 < p_T^{trig} < 4$ GeV/c。在将来更多统计量时，选择更高横动量的触发粒子来研究是必需的，因为它们有更多的可能来自于喷注的碎裂。在不久的将来，STAR探测器将升级TPC的数据获取系统至DAQ1000。届时，我们将可以采集至少10倍于这篇论文所有的2004年运行采集的数据，从而使得我们可以利用高p_T触发粒子来进一步研究粒子关联。

关键词：相对论重离子碰撞，夸克－胶子等离子体，强子对关联，反应平面，喷注，脊。

Abstract

Quarks and gluons are the basic building blocks of the matter. And Quantum ChromoDynamics (QCD) is believed to be a successful theory to describe the strong force between the color charge carriers —— quarks and gluons. According to asymptotic freedom —— one of key features of QCD, quarks and gluons are confined in hadrons and no free quarks and gluons are observed. Lattice QCD predicts a phase transition at high temperature or high density from the normal hadron gas state to a state with quarks and gluons which are deconfined from hadrons —— the Quark Gluon Plasma (QGP). The Relativistic Heavy Ion Collider (RHIC) located at Brookhaven National Laboratory (BNL) was designed to collide high energy heavy ions to create such a high temperature and high density matter, simulating the evolution of the early universe in the first few seconds after the Big Bang. After several years of measurements accumulation, the matter created RHIC has been proved to be more like a medium most resemble of properties of a perfect liquid of strongly interacting quark gluon plasma. The two pillars for this discovery are the observed strong elliptic flow and jet quenching. To quantify the property of the medium created at RHIC, high transverse momentum (p_T) particles, which are presumably from jet fragmentations, are ideal penetrating probes. Usually people use high p_T single hadron yields and di-hadron correlations with a high p_T trigger particle to study the medium created at RHIC. While suppression of high p_T single hadron yields has limited sensitivity to the medium core, di-hadron correlation measurements will provide richer and more valuable information about the properties of the created medium.

The disappearance of back-to-back jet from the first high p_T di-hadron correlation measurement at RHIC has been recognized as an evidence of the jet quenching discovery. The following analysis by correlating low p_T particles associated with the high p_T trigger particle shows the broadening in the away side, which is consistent with the jet energy dissipation in the medium. The first di-hadron analysis with respect to the reaction

plane shows the away-side suppression happens out-of-plane while it is not significant in-plane. This indicates the possible path length effect in the jet energy loss. Recently, a new phenomenon of the long range $\Delta\eta$ correlation——so called "Ridge" has been observed in the near side di-hadron correlation, but the origin of ridge phenomenon is still not understood yet [Arm04, Vol06, Maj04, Won07, Hwa05].

In this thesis, we present STAR results of di-hadron azimuthal correlations with a high p_T trigger particle relative to reaction plane and a lower p_T particle associated with the trigger particle in $\sqrt{s_{NN}} = 200$ GeV Au + Au collisions at RHIC. The large data sample (which is about 10 times more than previous analysis): Au + Au minimum bias events and Au + Au central events collected during year 2004 run were used in this analysis. The minimum bias d + Au collision data collected in year 2003 were used for the baseline comparison.

The di-hadron azimuthal angle correlation was calculated according to the azimuthal angle of the trigger particle relative to the reaction plane ($\phi_s = |\phi^{trig} - \Psi_{EP}|$). Reaction plane was reconstructed using the standard event plane method. Particles falling in the p_T bin of associated particles (p_T^{assoc}) were eliminated in the event plane reconstruction to avoid the auto-correlation. The v_4 contribution in the flow background, which had not been taken into account, was found to be not negligible in the di-hadron correlation analysis relative to the reaction plane. We re-evaluated the flow background formula to include the v_4 contribution. The flow parameters were taken from the averaged STAR measurements using the standard event plane method and the four particle cumulant method. The difference between two methods is the most significant systematic error contribution in the results. The normalization of the flow background was calculated using an improved method based on the Zero-Yield-At-Minimum (ZYAM). The flow background was calculated in each p_T^{assoc} bin and ϕ_s bin, and it was subtracted from the raw di-hadron correlation distributions to extract the correlation function we are interested. Both the mid-central 20-60% and the top 5% central Au + Au collisions were investigated, and the minimum bias d + Au collision data were presented for

baseline comparison. The correlation functions are also obtained from small and large $|\Delta\eta$ regions separately, in attempt to isolate the jet and ridge contributions to the near-side correlation strength and study their behavior in ϕ_s.

The di-hadron correlations are strongly modified in Au + Au collisions with respect to minimum bias d + Au collisions. The modification strongly depend on the trigger particle orientation relative to the event plane and evolve with associated p_T^{assoc}. The qualitative trend of the correlation function with ϕ_s appears similar in central and mid-central collisions; quantitatively, the ϕ_s dependence of the correlation function is stronger in the middle central collisions. The p_T^{assoc} dependences of the correlation function are similar in the two centrality selections.

The away-side correlation broadens from in-plane to out-of-plane, and broadens with increasing associated p_T^{assoc} for most ϕ_s slices. For 20-60% Au + Au collisions, the away-side correlation starts as a single peak in the reaction plane, and becomes a stronger and stronger double-peak structure as the trigger particle moves from in-plane to out-of-plane. For top 5% central Au + Au , the away-side correlation already shows a double-peak structure in the reaction plane, and the double-peak becomes stronger and stronger from in-plane to out-of-plane. The trends of the away-side modification underscore the importance of the path-length that the away-side parton transverses in the medium. The away-side medium path-length in the reaction plane direction in 20-60% Au + Au collisions is quite modest and not enough to generate significant modification to jet correlation, while that in the top 5% collisions is long enough to cause significant jet modification. The strongest modification is found for trigger particles perpendicular to the reaction plane where the away-side medium path-length is the longest, and this path-length appears to be not very different in 20-60% and top 5% Au + Au collisions.

The near-side correlation amplitude decreases from in-plane to out-of-plane. The decrease was found to entirely come from the decrease in the long range $\Delta\eta$ correlation (ridge). The ridge yield decreases to ~ 0 at out-of-plane in the 20-60% centrality, while significant ridge yields persist from in-plane to out-of-plane in top 5% collisions. The

jet contribution to the near-side correlation is extracted from the difference of small and large $\Delta\eta$ correlations, subject to small experimental systematic uncertainties. The jet contribution in the 20-60% centrality appears to somehow increase from in-plane to out-of-plane. The near-side jet parallel to the reaction plane appears to have suffered significant interactions with the medium, which reduce the real jet correlated multiplicity and produce a long range $\Delta\eta$ ridge containing a large number of hadrons. The near-side jet perpendicular to the reaction plane, on the other hand, appears to suffer minimal medium modification, generating small amount of ridge. The top 5% results are qualitatively similar, but the significant ridge contribution persists over all ϕ_s, and the variations of the jet and ridge magnitudes in ϕ_s is significantly smaller, consistent with the more spherical collision geometry.

The main results presented in this thesis are with $3 < p_T^{trig} < 4$ GeV/c. The results from trigger particles with higher p_T is necessary to check the results since they are more probably coming from jet fragmentation. In the future RHIC run with the TPC DAQ1000 upgrade, we are able to accumulate more than ten times statistics of the data sample in Run IV, used in this thesis. It provides us the possibility of investigating the correlations with high p_T trigger particles in the future.

Keywords: Relativistic heavy ion collisions, STAR experiment, Quark Gluon Plasma, Di-hadron correlation, Reaction plane, Ridge

Table of Contents

List of Figures

List of Tables

CHAPTER 1

Introduction

1.1 Quantum Chromodynamics

To the present human being's knowledge, matter is fundamentally made of leptons, quarks and force mediators. The forces between fundamental components are grouped into four kinds: gravitation, electromagnetic interaction, weak interaction, and strong interaction. Since 1970's, the later three forces have been unified into the *Standard Model* (SM), consisting of the electroweak unification theory which describes the elctromagnetic and weak interactions, and the *Quantum Chromodynamics* (QCD) which describes the strong forces.

QCD is a fundamental gauge theory for quarks and gluons - the strong force mediators. They carry a property analogous to electric charge called *color*. QCD [DKS03] is a non-Abelian gauge field theory based on the gauge group $SU(3)_C$, with gauge bosons - color octet gluons for factors and a unique group coupling constant g_s. The subscript C denotes the quantum number - color. There are three colors in QCD, namely Blue, Green, Red. Quarks belong to a color triplet representation in the $SU(3)_C$ symmetry, but hadronic states are assumed to be color singlets in QCD. Owing to the non-abelian character of the color group, the invariant QCD Lagrangian requires gauge (gluon) self-interactions, which do not appear in *Quantum ElectroDynamics* (QED) - the gauge theory describing electromagnetic interaction. In other words, whereas photons carry no electric charge, gluons do carry color charge. So they can interact directly with each other.

Generally speaking, QCD is a non-perturbative gauge theory in most cases. It can be calculated using a computer-assisted method - *Lattice QCD* [Gup98]. In this calculation, the spacetime is discretized and replaced by a lattice with lattice spacing equal to a. The quark fields are only defined at the elements of the lattice and the gauge fields are defined on the links of the lattice. The action is rewritten in such a way that the limit $a \to 0$ formally gives the original continuous action. Lattice QCD has been widely used for reliable QCD calculations. The precision of Lattice QCD calculations are limited by the lattice spacing or the computing power.

1.1.1 QCD running coupling constant α_s and Asymptotic freedom

The renormalized QCD coupling shows a scale dependent coupling $\alpha_s(\mu)$ (running coupling), similar to that in QED. However, the QED running coupling increases with energy scale, while the gluon self-interactions lead to a complete different behavior in QCD. $\alpha_s(\mu)$ can be written as Equation 1.1:

$$\alpha_s(\mu) \equiv \frac{g_s^2(\mu)}{4\pi} \approx \frac{4\pi}{\beta_0 \ln(\mu^2/\Lambda_{QCD}^2)} \tag{1.1}$$

Where $\beta_0 = 11 - \frac{2}{3}n_f$, n_f is the number of quarks with mass less than the energy scale μ. When $\beta_0 > 0$, this solution illustrates the *asymptotic freedom* property: $\alpha_s \to 0$ as $\mu \to \infty$. The larger energy transfer is equivalent to the shorter distance, according to the uncertainty principle. So the strong force becomes smaller at shorter distance, which is well known as the *Asymptotic Freedom*. Its discovery has been awarded the Nobel Prize in Physics 2004. On the other hand, this solution also shows strong coupling at $\mu \sim \Lambda_{QCD}$, so QCD is non-perturbative in this case. α_s needs to be determined from experiment. The world averaged α_s at the fixed-reference $\mu_0 = M_Z$ is $\alpha_s(M_Z) = 0.1187 \pm 0.002$ [Yao06], and the QCD scale $\Lambda_{QCD} \sim 200$ MeV. Figure 1.1 shows the measured α_s at different momentum transfer scale μ compared with Lattice QCD calculations.

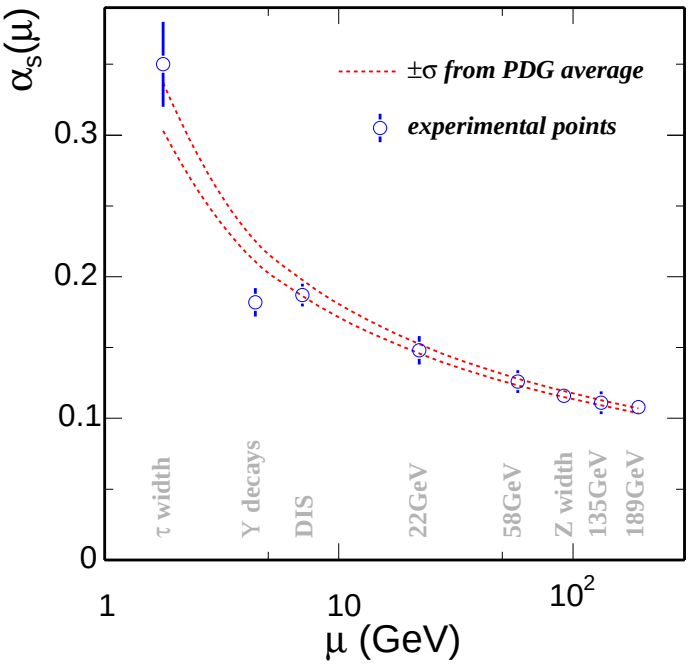

Figure 1.1: Measured QCD running coupling constant α_s from different experiments compared with Lattice QCD calculations.

1.1.2 Perturbative QCD (pQCD)

Perturbation theory can be used with QCD for interactions involving large momentum transfers (*i.e. hard processes*). Physics quantities, such as cross sections, can be calculated to a truncated series, known as *Leading Order* (LO), *Next-to-Leading Order* (NLO) *etc.*. There are plenty of experiments on high energy processes which offer quantitative tests of pQCD. Figure 1.2 left plot shows the inclusive jet cross section measurements at various energies from PDG [Yao06] compared with NLO pQCD calculations. The pQCD calculation shows nice agreements with high energy UA1, UA2, CDF data etc. Recently, there was also a measurement on the inclusive jet cross section measurement from the STAR collaboration at RHIC [Abe06], shown in Figure 1.2 right plot, and the NLO pQCD calculation agrees with the data points well.

In QCD, assuming factorization, the cross section of an inclusive process $A + B \rightarrow$

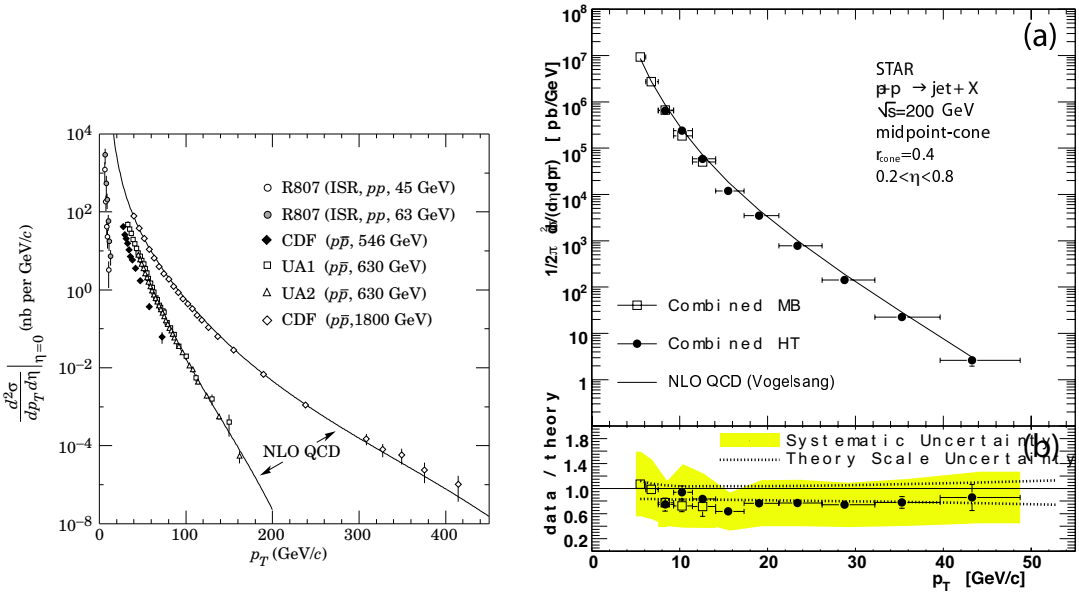

Figure 1.2: Differential cross-sections for single jet production at pseudo-rapidity $\eta = 0$ as a function of the jet transverse momentum p_T in proton (anti-)proton collisions compared with NLO pQCD calculations. Left: Measurements and calculations at ISR, SPS and Tevatron energies. Right: Measurements and calculations at RHIC energy.

$C + ...$ can be written as:

$$E_C \frac{d\sigma_{AB\to C}}{d^3p} = K \sum_{abcd} \int dx_a dx_b f_{a/A}(x_a, Q_a^2) \frac{d\sigma}{dt}(ab \to cd) \frac{D_{c/C}(z_c, Q_c^2)}{\pi z_c} \tag{1.2}$$

The middle term $\frac{d\sigma}{dt}(ab \to cd)$ can be calculated in pQCD from Feynman diagrams. The first term $f_{a/A}(x_a, Q_a^2)$ or $f_{b/B}(x_b, Q_b^2)$ is the hadron *Parton Distribution Function* (PDF) and the last term $D_{c\to C}(z, Q_c^2)$ is the *Fragmentation Function* (FF) that describes the transition from a parton to a hadron. For leptons, these two terms do not contribute in this formula. Hence, we can measure PDFs through lepton-nucleon deep inelastic scattering interactions and FFs through high energy e^+e^- collisions.

1.1.3 Confinement and chiral symmetry breaking

In QCD, quark must be confined in hadrons because quarks have color quanta, while hadrons are color-neutral to us. This can also be expected from the QCD coupling $\alpha_s(\mu)$. When two quarks are separated to a large distance, which corresponds to a small energy scale, the coupling becomes strong, *i.e.* intuitively, more and more self-coupled gluons hold the quarks not to be isolated. It is quite different in QED because there is no self coupling between photons, so that we can observe isolated electric charges.

Phenomenogically, the binding potential between a quark pair is often defined as the Cornell potential

$$V(r) \sim -\alpha/r + \sigma r \tag{1.3}$$

The first term is analogous to the electric potential between two electric charges, but between two color charges. The second term is introduced to hold the two quark without separating from each other. In this approximation, infinite amount of energy are needed to observe the isolated quark, or the deconfined quark. We have never seen deconfined quarks in normal temperature and density.

In the absence of quark masses, the QCD Lagrangian can be split into two independent sectors: the left- and right-handed components [Pic95]. This Lagrangian is invariant

under chiral symmetry transformations then. This symmetry, which is the extension of classical $SU(3)$, is a global $SU_L(n_f) \times SU_R(n_f)$ symmetry for n_f massless quark flavors. However, it is spontaneously broken in the vacuum in the Nambu-Goldstone's way to realize this symmetry and this breaking gives rise to $(n_f^2 - 1)$ massless Goldstone particles. Thus we can identify the π, K, η with the Goldstone modes of QCD: their small masses being generated by the quark-mass matrix which explicitly breaks the global chiral symmetry of the QCD Lagrangian.

1.1.4 QCD Phase transition

QCD matter is mostly observed as nuclei or hadron gas in our normal condition. Recent advances in the formulation of thermaldynamical lattice QCD at finite temperature and density however, suggests that when sufficiently high temperature and energy density are reached, quarks becomes effectively deconfined, or QCD predicts a phase transition to a new matter, named *Quark Gluon Plasma* (QGP), with new (color) *degrees of freedom* (d.o.f.), which could be manifested by a rapid increase in entropy density, hence in pressure with increasing temperature. Meanwhile, in this new matter the broken chiral symmetry in normal QCD matter will be restored and consequently, masses of scalar mesons and vector mesons will decrease [Kar02a]. Lattice QCD calculations provide quantitative predictions on this phase transition: the critical temperature of this phase transition is $T_c \sim 150 - 180$ MeV, and the energy density at the critical point is $\varepsilon_c(T_c) \sim 1 - 3$ GeV/fm^3 (~ 0.17 GeV/fm^3 for nuclear matter) [Kar02b]. The appearance of these color d.o.f. can be illustrated by a sharp increase in pressure with temperature, shown in Figure 1.3 [KLP00].

The arrows indicate the Stefan-Boltzmann limits, which are for the systems with massless, non-interacting quarks and gluons. The insert plot shows the ratio of p/p_{SB} as a function of T for 3 different flavor configurations. The similarity of the three curves indicates that besides the effect of quark masses, there should be interactions in the newly formed system, which is different from the original weakly interacting QGP scenario.

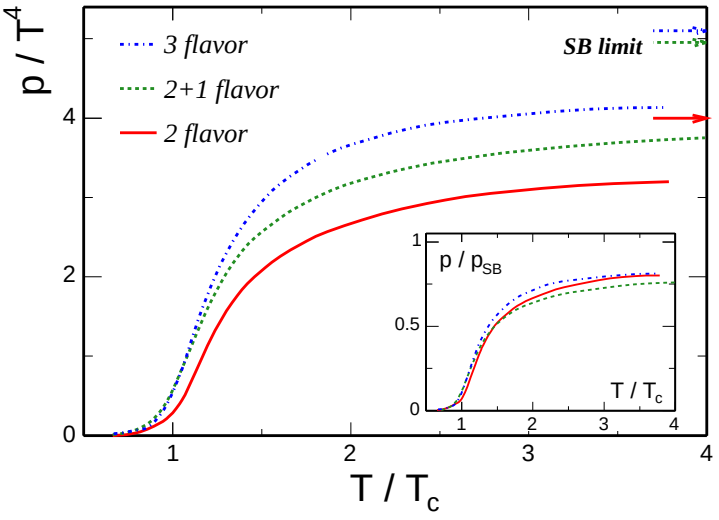

Figure 1.3: Lattice QCD calculations for the evolution of p/T^4 with the increase of temperature T for 3 different flavor configurations. The arrows indicate the SB limit for each case. The insert plot shows the ratio of p/p_{SB} as a function of T.

Lattice QCD calculations of the potential between two heavy-mass quarks also offer evidence of deconfinement.

Figure 1.4 shows a recent calculation of the heavy-mass quark-antiquark pair Cornell potential in different temperature conditions [KLP00]: with the increase of temperature, the rampart of the potential between two quarks, which causes confinement, will bend down and thus liberate quarks from the trap. In addition, the continuous bending without sudden change indicates a crossover transition at high temperature and vanishing net quark density. In an extreme high density of color charges, color charges could be screened in a similar way as electric charges known as Debye screening: the long-range interaction is shortened in dense medium of charges. In this situation, the potential with color screening is given by [Sat00]

$$V(r) = -\alpha/r + \sigma r[\frac{1-\exp(-\mu r)}{\mu r}] \tag{1.4}$$

where μ is the color screening mass. When μ is sufficiently high, the potential remains a finite constant as r increases, which also leads to the deconfinement of the quark pair system.

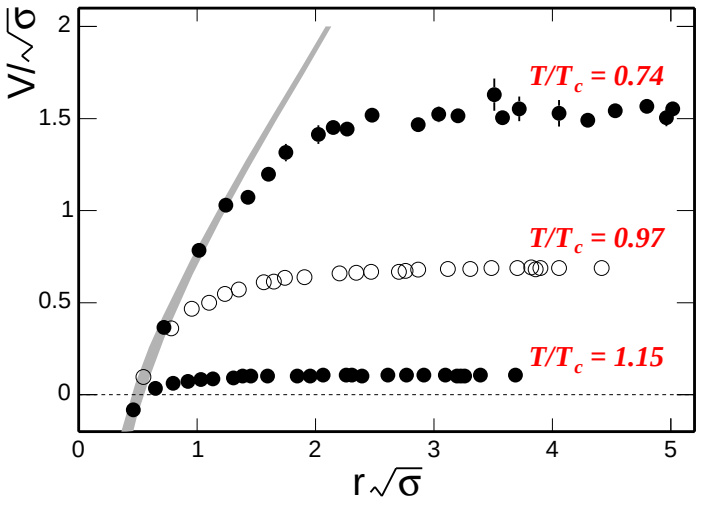

Figure 1.4: Lattice calculations for the heavy-mass quark potential in different temperature cases. The band depicts the Cornell potential of $V(r) = -\alpha/r + \sigma r$ with $\alpha = 0.25 \pm 0.05$.

1.2 Heavy Ion Collisions

Experimentally, to search for this new kind of matter, a large amount of energy needs to be packed into a limited space volume. Heavy ion collisions have been proposed as a more effective way because the initial energy density increases as a power law function with the atomic number while only logarithmically with collision energy [Lin96]. One of the prime motivations for building the Relativistic Heavy Ion Collider (RHIC) is to create and study such a kind of matter made of deconfined quarks and gluons (*i.e. Quark Gluon Plasma* (QGP)). The temperatures and densities reached are expected to be similar to those thought to have prevailed in the very early universe, prior to the formation of protons and neutrons.

Figure 1.5 shows the QCD phase diagram. The grey shadows depict the first order phase transition boundaries, while at high temperature and low density, the phase transition from hadron gas to QGP is expected to be a cross-over from Lattice QCD [FK02]. The red dot labeled "3cr point" is the end point of first order phase transition, or critical point. The blue dots depict the freeze-out conditions of several collider energies from

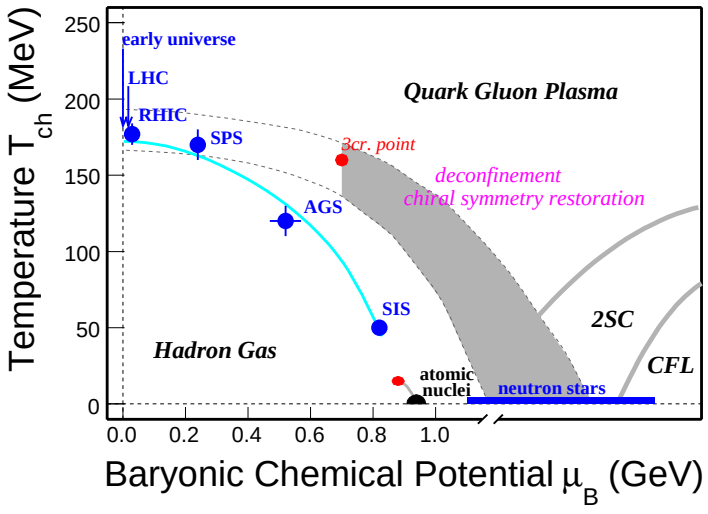

Figure 1.5: QCD phase diagram. The grey shadows depict first-order phase transition boundaries. The red dots depict the critical points and "3cr point" is calculated from Lattice QCD [FK02]. The blue dots depict the freeze-out conditions of several collider energies from statistical fit [Bra01].

statistical model fit [Bra01].

Since year 2000 the first Au + Au collision was displayed, RHIC has conducted many very successful runs. The heavy ion collisions at RHIC constitute an exploration into the unknown and one should be ready to be surprised. Plenty of exciting physics results reveal that the matter created at RHIC is quite different from what we observed before: It cannot be described by hadronic degrees of freedom and illustrates many of the signatures in a QGP scenario. These measurements provide strong hints for the discovery of a strongly interacting QGP [Adc04].

Figure 1.6 illustrates the space-time evolution of a heavy ion collision at RHIC to our knowledge now. The collision starts with two highly Lorentz contracted nuclei colliding with each other, and there will be four possible stages following that: a pre-equilibrium stage, an equilibrated-deconfined-parton stage, an interacting-hadron stage and finally a free-hadrons stage. The experiments can only detect hadrons in the free-hadron stage of the collisions evolution. Probing the early stage of the collision evolution with particles

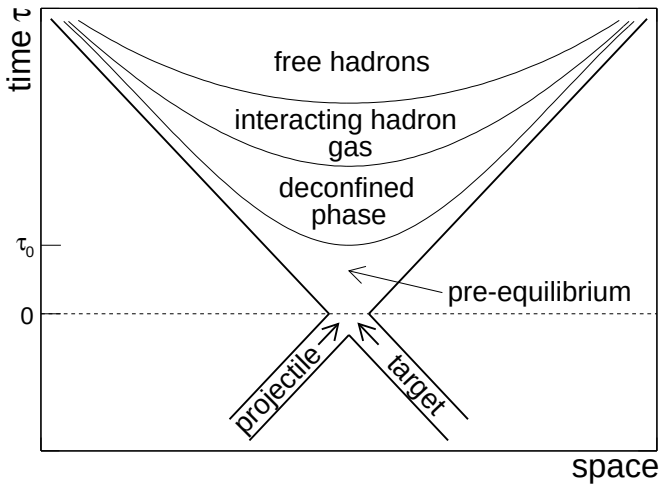

Figure 1.6: Space-time evolution of a heavy ion collision at RHIC.

measured in the final stage is a significant challenge. Penetrating probes, who aren't affected by the later stage interactions, will be essential to study the property of the matter in the early stage. Jets from initial hard scattering are ideal probes.

1.2.1 Initial condition

The initial condition of the heavy ion collisions at RHIC is one of the most fundamental quantities, which need to be addressed to answer whether the energy densities reach the deconfinement phase transition. Because baryon number is conserved and the rapidity distributions are only slightly affected by rescattering in the late stage of collisions, the measured net baryon $(B - \bar{B})$ distribution can reveal the energy loss of initial participants and allow us to estimate the degree of nucleon stopping power. Measurements from the BRAHMS collaborations at RHIC [Bea04] show that $73 \pm 6^{+12}_{-26}$ GeV of the initial 100 GeV per participant is deposited and available for excitations, which is quite significant. Figure 1.7 shows rapidity loss $\langle \delta y \rangle = \langle y \rangle - y_p$ for different energies from AGS to RHIC [Bea04].

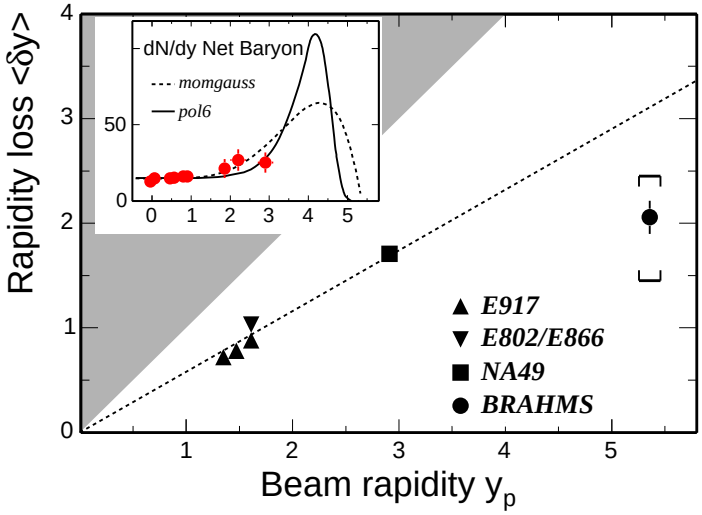

Figure 1.7: The rapidity loss as a function of beam rapidity. The shadow indicates an unphysical region and the dashed line depicts the phenomenological scaling $\langle \delta y \rangle = 0.58 y_p$. The insert plot shows the measured data points of net baryon distribution from BRAHMS and different extrapolations to full rapidity.

The initial Bjorken energy density [Bjo83] can be calculated using:

$$\epsilon_{Bj} = \frac{1}{A_\perp \tau} \frac{dE_T}{dy} \tag{1.5}$$

where τ is the formation time of the medium and $A_\perp$ is the nuclei transverse overlap region area. The formation time is not known but is generally taken to be approximately 1 fm/c. The density of normal nuclear matter is approximately 0.16 GeV/fm^3. Lattice calculations predict that the phase transition to deconfined quarks and gluons occurs $\sim$ 1 GeV/fm^3. For the top RHIC energy ($\sqrt{s_{NN}}$ = 200 GeV), the PHENIX dE_T/dy measurement [Adl04] indicates an initial energy density of $\sim$ 5 GeV/fm^3 ($\tau \approx$ 1 fm/c, $A_\perp = \pi R^2$, $R \approx 1.2A^{1/3}$ fm) for central Au + Au collisions, exceeding the critical energy density thought necessary for the phase transition.

In most cases when nuclei collide off-axis, the transverse overlap region will be asymmetric. Figure 1.8 shows the overlap density for Au nuclei colliding with impact parameter b = 5 fm. A Woods-Saxon distribution is used for the density profile of the Au nuclei. Most observables in heavy ion collisions are integrated over the azimuthal angle and they

are insensitive to the azimuthal asymmetry of the initial source. In this thesis, we discuss measurements sensitive to the conversion of the initial spatial anisotropy. The particles produced in-plane and out-of-plane traverse different lengths in the medium source. The detail technique will be discussed in Chapter 3.

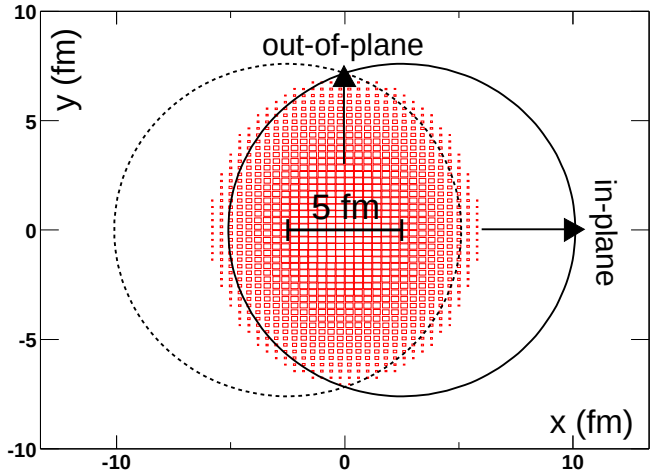

Figure 1.8: The overlap density for Au nuclei colliding off-axis for impact parameter b = 5 fm. The beam directions are in and out of the of the page. The reaction plane is by the beam axis and the vector connecting the centers of the two nuclei.

1.2.2 Bulk property and collective motion

The bulk matter created in heavy ion collisions is essential for discovery and study of the new QGP phase. Its property can be studied via particle yields, momentum spectra, anisotropic parameters etc. Different probes can reveal the system information at different evolution stages. In this section, I will introduce the coupious production of the majority of the particles in the low and intermediate momentum ($p_T <\sim 5$ GeV/c).

1.2.2.1 Particle spectra and freeze-out

Hadron spectra, especially in the soft sector, reflect the properties of the bulk system. Since difference hadrons have different production (hadronization) mechanisms, systematic analysis of specified particle transverse momentum spectra can reveal the characteristics of the system during evolution at different stages. Figure 1.9 shows the identified particle (π^-,K^-,$\bar{p}$,Λ,Ξ,Ω,ϕ) p_T spectra measured in central Au+Au collisions [Ada04a, Ada04b, Ada05a, Cas04] as well as the Blast Wave thermal model [SSH93] fits to the data points.

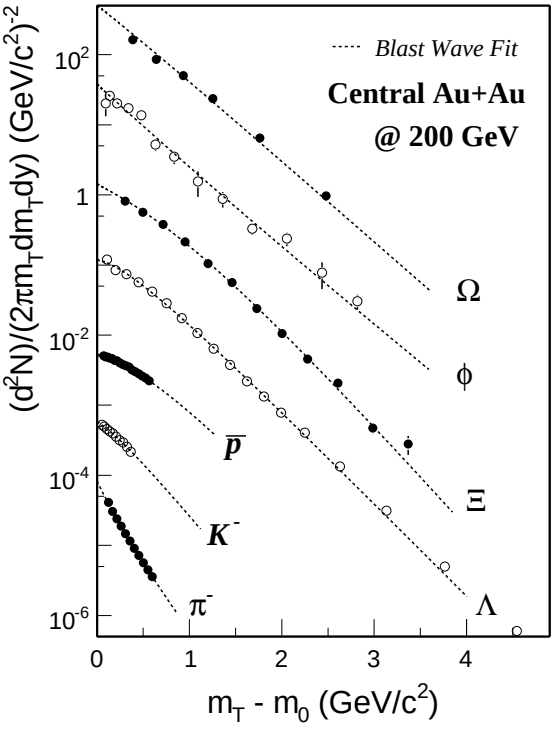

Figure 1.9: Identified particle spectra in central Au+Au collisions at $\sqrt{s_{NN}} = 200$ GeV and the Blast Wave fit results. The BW fits were done for π^-, K^-, $\bar{p}$ simultaneously and for other particles separately.

The bulk system after the nuclei collide evolves dramatically: the volume expands and the density becomes more and more dilute, but the particle collective velocity develops larger and larger. The data points on that plot show the slopes of particle spectra

changes for different particles (masses), indicating the strong collective motion of final state particles. The dashed lines depict the fit results from the Blast Wave thermal model [SSH93]. In the Blast Wave thermal model, local thermal equilibrium is assumed. "Blast wave" means that particles freeze out from the system surface simultaneously when dense matter becomes dilute enough. Under the assumption of simple cylindrical source and boost invariance in rapidity, there are only two parameters to drive the particles spectra: freeze-out temperature T_{fo} and average transverse velocity $\langle\beta_T\rangle$. Figure 1.10 shows the fit parameters T_{fo} versus $\langle\beta_T\rangle$ for different particles in Au + Au collisions. Simultaneous fit to the light hadrons (π^-, K^-, $\bar{p}$) gives larger flow velocity and small freeze-out temperature in central collisions than peripheral collisions, indicating that light hadrons freeze out later with stronger collectivity in central collisions. The fit to multi-strange hadrons (Ω and ϕ) in central Au + Au collisions shows higher freeze-out temperature and lower transverse velocity compared to light hadrons, indicating those particles leave the system at the earlier stage than light hadrons. Since multi-strange hadrons are expected to have much smaller hadronic scattering cross sections and their transverse momentum distributions will not change much after the chemical freeze-out. The kinetic freeze-out temperature from the fit to multi-strange hadrons is consistent with the chemical freeze-out temperature T_{ch}, which is close to the critical temperature T_c, meaning the temperature of the system created in the collisions is greater than T_c and hence the phase transition may take place at RHIC energy.

1.2.2.2 Anisotropic flow

As mentioned above, in non-central heavy ion collisions, the initial overlapping region of the two nuclei is anisotropic in coordinate space. This leads to anisotropic pressure gradient distributions in the dense matter and subsequently is converted to an anisotropy in the final state momentum space via rescattering. The dynamic expansion of the system will wash out the coordinate-space-anisotropy, while the momentum-space-anisotropy will persist during the evolution of the system [KH03]. Hence the measurement of the

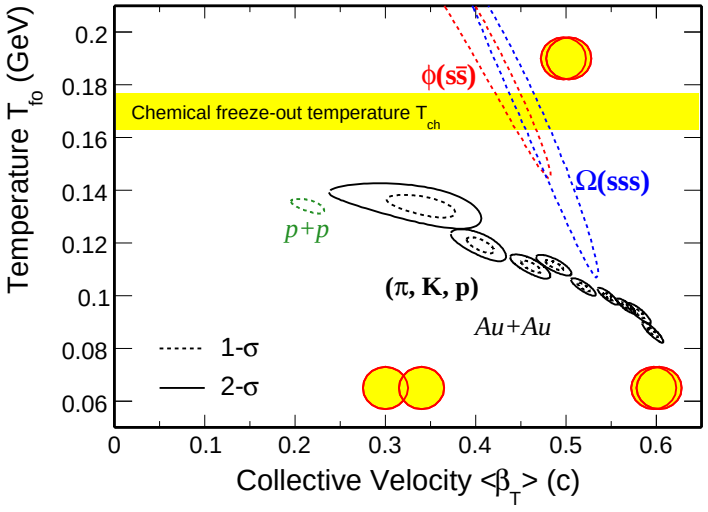

Figure 1.10: Blast-wave parameters T_{fo} vs. $\langle\beta_T\rangle$ contour plot from the simultaneous fits to stable hadrons (π, K, p) spectra in Au + Au collisions and $p + p$ collisions and separate fits to multi-strange hadrons $\phi(s\bar{s})$, $\Omega(sss)$ spectra in central Au + Au collisions. The contours of π, K, p fits in Au + Au are for peripheral collisions in the left and central collisions in the right. The contours of ϕ and Ω are for central Au + Au collisions.

particle azimuthal anisotropy with respect to (w.r.t) the reaction plane can reveal the dynamics at early stage of the collisions.

The final state particle spectrum in momentum space can be expanded into a Fourier series in terms of the particle azimuthal angle ϕ w.r.t. the reaction plane Ψ_{rp}, shown as Equation 1.6.

$$E\frac{d^3N}{dp^3} = \frac{d^2N}{2\pi p_T dp_T dy}(1 + \sum_{n=1}^{\infty} 2v_n \cos[n(\phi - \Psi_{rp})]) \tag{1.6a}$$

$$v_n = \langle\cos[n(\phi - \Psi_{rp})]\rangle \tag{1.6b}$$

where v_n is the n-th harmonic Fourier coefficient. The first and second harmonic coefficients v_1, v_2 are called directed and elliptic flow. Due to the approximate elliptic shape of the overlapping region, the elliptic flow v_2 is the largest harmonic flow observed in mid-rapidity. Because of the quenching of coordinate-space-anisotropy, elliptic flow can reveal early information about the system and because it depends on rescattering,

elliptic flow is sensitive to the degree of thermalization of the system in the early stage.

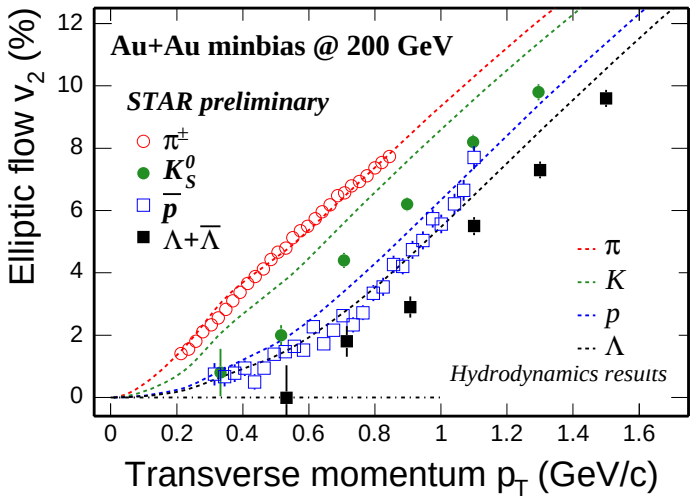

Figure 1.11: Elliptic flow v_2 of identified particles as a function of p_T at low p_T region compared with hydrodynamic model predictions.

The identified particle $v_2(p_T)$ shows strong p_T dependence. Figure 1.11 shows the measurements and the hydrodynamic model predictions for $p_T < 2$ GeV/c [Ada05d]. In this low p_T region, the measurements show v_2 has larger values for lower mass particles. While hydrodynamic models, which assume ideal relativistic fluid flow and negligible relaxation time compared to the time scale of the equilibrated system, successfully reproduce such a mass ordering observation and reasonably describe the v_2 magnitudes. This agreement implies early thermalization, *i.e.* strongly interacting matter with a very short mean free path dominates the early stages of the collisions.

A recent publication on the ϕ meson elliptic flow measurement shows the ϕ mesons have a finite and comparable v_2 as other mesons [Abe07]. We learned from the particle yield analysis that ϕ meson cannot be coupiously produced from the hadronic rescatterings [Ada05a], thus ϕ elliptic flow will only come from the partonic rescatterings. The finite v_2 for ϕ meson suggests that a partonic matter with strong collectivity has been produced at RHIC.

1.2.2.3 Coalescence

In elementary collisions, due to small produced multiplicity, fragmentation is the dominant hadronization scheme for produced particles. While in high energy heavy ion collisions, the system is so dense and occupied with tons of particles. Once the wave functions of different particles are close enough in coordinate and momentum spaces, they may coalesce and form hadrons [LK02, MV03].

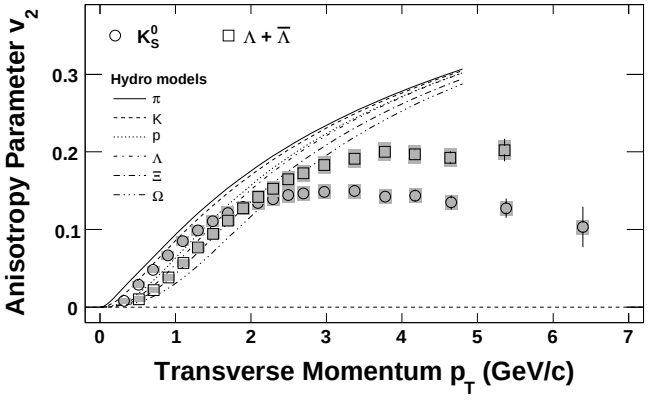

Figure 1.12: v_2 of K^0_S and Λ in a large p_T range in Au + Au minimum bias collisions. At $\sim 2-3$ GeV/c, v_2 of both particles starts to saturate and deviate from hydrodynamic predictions.

Figure 1.12 shows identified particle v_2 versus p_T in a larger p_T range. v_2 for mesons and baryons saturates above a certain p_T ($\sim 2-3$ GeV/c), and start deviating from the hydrodynamic model predictions. In addition, v_2 of mesons and baryons are different at intermediate p_T (2-5 GeV/c). Figure 1.13 shows by scaling both v_2 and $(m_T - m_0)$ with *the Number of the Constituent Quarks* (NCQ) in the corresponding hadron (n_q = 2 for mesons and 3 for baryons), all particles fall onto one universal curve, shown on the right panel. This meson/baryon grouping phenomenon was also observed in the nuclear modification factor R_{CP} at intermediate p_T ($1.5 < p_T/(\text{GeV}/c) < 5$) [Ada04b, Sor03]. Coalescence models [LK02, MV03] which assume hadrons are formed through coalescing of constituent quarks provide a viable explanation for these observations. This indicates the flow developed during a sub-hadronic (partonic) epoch, and offers a strong evidence

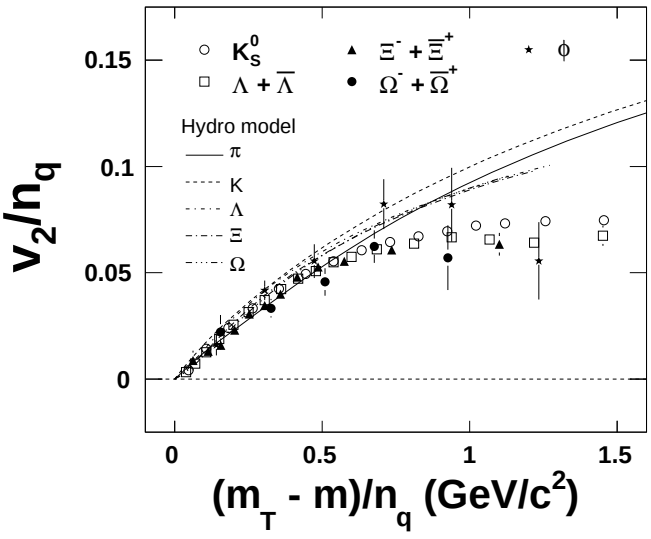

Figure 1.13: v_2/n_q vs. $(m_T - m_0)/n_q$ for different particles. All measured particle v_2 seems to follow the NCQ scaling.

of deconfinement at RHIC.

1.2.3 Jet quenching

As emphasized several times above, due to strongly dynamic evolution of the system, penetrating probes would be ideal to gain early stage information. In heavy ion collisions at RHIC energy, high p_T ($p_T >\sim 5$ GeV/c) particles are believed to be produced mainly from the initial QCD hard-scattering processes [Adl02a]. These energetic particles can be used as unique probes by studying their interactions with the medium since jet quenching scenario predicts that the high transverse momentum partons will interact with the medium and lose a large fraction of their energy in the medium prior to forming hadrons and it's further indicates that the energy loss depends on the gluon density and the path-length that the away-side parton traverses.

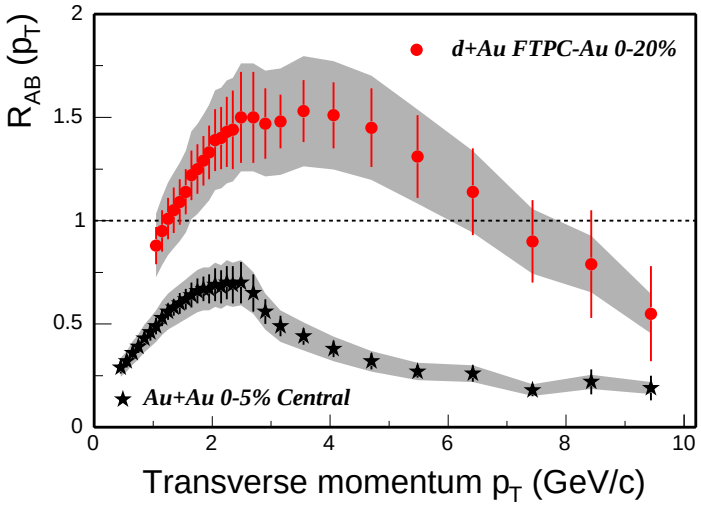

Figure 1.14: Nuclear modification factor in central Au + Au and d + Au collisions.

1.2.3.1 Single hadron production suppression

One of the most striking phenomena observed at RHIC is the single hadron production suppression at high p_T in central Au + Au collisions. Experimentally, the widely used observable quantity of particle energy loss is called the nuclear modification factor R_{AB}, the difference between the spectrum in A+B collisions w.r.t. a $p + p$ collision reference, is extensively used. It is defined as:

$$R_{AB}(p_T) = \frac{d^2N_{AB}/dp_T dy}{T_{AB} d^2\sigma_{pp}/dp_T dy} \tag{1.7}$$

where $T_{AB} = \langle N_{bin} \rangle / \sigma_{pp}^{inel}$ is the nucleus overlap function, calculated from a Glauber model [Won94]. N_{bin} represents the number of binary collisions in a nucleus-nucleus collision. For high p_T particles, they are mainly from the initial hard scattering, and less affected by the nuclear effects such as the shadowing, the Cronin effects *etc.*, their spectra in central Au + Au collisions are expected to be scaled with the number of binary collisions ($R_{AB} = 1$). However, the experimental result [Ada03] in Figure 1.14 shows that there is a strong suppression relative to the binary scaling expectation at high p_T in the central Au + Au collisions. This suppression is not seen in d + Au collisions, the control experiment, in which there is supposed to be no jet medium interaction in the

final states. This suggests the suppression in central Au + Au is due to the final state interactions rather than initial state effect and thus a very dense matter must be created in central Au + Au collisions at RHIC. This phenomenon is well known as so-called "jet quenching".

1.2.3.2 Di-hadron correlations

The single particle production suppression may be attributed to the surface bias on the particle selection. This ambiguity can be cleared by analyzing the back-to-back di-hadron production. Figure 1.15 shows the high p_T di-hadron correlations with a trigger particle $4 < p_T^{trig} < 6GeV/c$ and associate particles $2 < p_T^{assoc} < p_T^{trig}$ for $p + p$ (black line), central d + Au (red circles) and central Au + Au (blue stars) collisions. The correlated hadron yield at high p_T, while not much changed on the near-side in all three systems, is strongly suppressed on the away side in central Au + Au relative to p + p and d + Au [Ada03]. The suppression in Au + Au collisions may be caused by an initial or a final state effect. However, the contrast between d + Au and central Au + Au collisions indicates that the cause of the disappearance of back-to-back jet correlation in Au + Au is associated with the medium produced in Au + Au but not in d + Au collisions. It's a final state effect. This lends strong support for the partonic energy loss picture (jet quenching).

Due to momentum conservation, the disappearance of away-side fast partons must result in an excess of softer emerging hadrons. Figure 1.16 left plot shows di-hadron azimuthal angle correlation for $p_T^{trig} > 4$ GeV/c and $p_T^{assoc} > 0.15$ GeV/c [Ada05b]. The plot exhibits jet-like peaks that are much broader for central Au + Au collisions than for $p + p$ collisions, which is consistent with dissipation of jet energy to the medium. The right plot in Figure 1.16 shows the centrality dependence of the $\langle p_T \rangle$ of the associated away-side charged hadrons (threshold lowered to 0.15 GeV/c), compared with that of inclusive hadrons [Ada05b]. This also offers a hint of the attainment of thermalization via the frequent soft parton-parton interactions in the early collision stages. But how

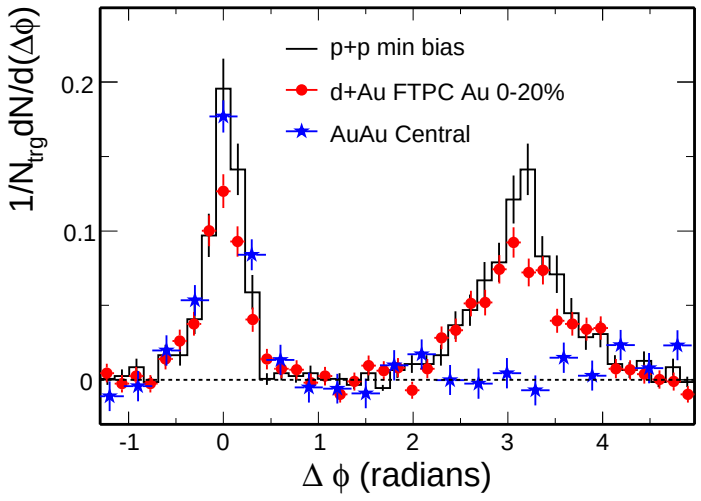

Figure 1.15: High p_T di-hadron azimuthal correlations in $p + p$, d + Au and Au + Au collisions. The figure is from reference [Ada03].

strong those partons interact is still a crucial open question, that needs to be answered quantitatively to address the evidence of early thermalization of the system.

In non-central collisions, the suppression of the away side particle production in di-hadron azimuthal correlations should depend on the relative orientation of the back-to-back pair with respect to the reaction plane according to jet quenching. In the first analysis by the STAR Collaboration, shown in Figure 1.17, the suppression of the back-to-back high p_T correlations for out-of-plane triggers is observed to be stronger compared to in-plane triggers, which is consistent with a path-length dependent jet quenching picture [Ada04c]. In this thesis, I will report the detail analysis on the di-hadron correlations with respect to the reaction from a large amount of data sample collected in Run IV.

Most recently, in the di-hadron $\Delta\eta \times \Delta\phi$ 2-Dim correlation analysis, enhanced near-side ($\Delta\phi \sim 0$) correlated yield at large $\Delta\eta$ has been observed in various trigger particle p_T and associate particle p_T selections [Put07], shown in Figure 1.18. This phenomenon is well known as the *Ridge* effect. The ridge persists even at the trigger $p_T \sim 9$ GeV/c, well into the kinematic region where jet fragmentation is thought to be dominant, suggesting it is associated with jet production. But the origin of its production mechanism is still

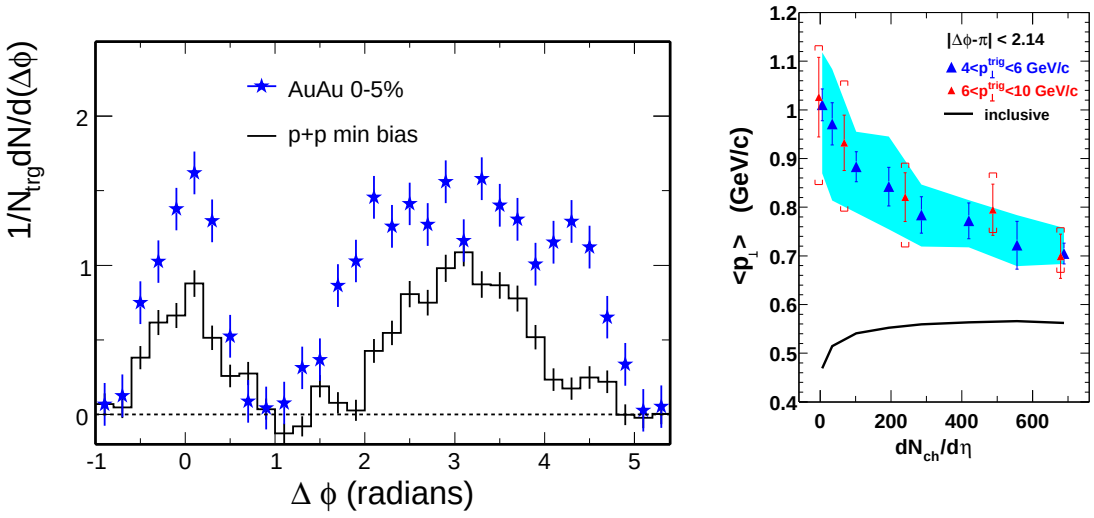

Figure 1.16: Left: Di-hadron azimuthal correlations with a high p_T trigger and low p_T associated particles in $p+p$, $d+$Au and Au + Au collisions. Right: The $\langle p_T \rangle$ of away side jet evolves with the change of multiplicities in $p+p$ (open triangle) and Au + Au (solid triangles) collisions.

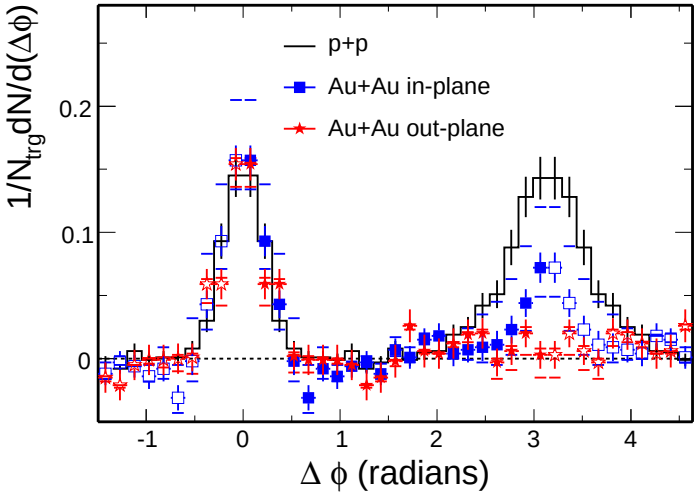

Figure 1.17: Di-hadron azimuthal correlations for in-plane and out-of-plane in $p+p$, $d+$ Au and Au + Au collisions.

under investigation.

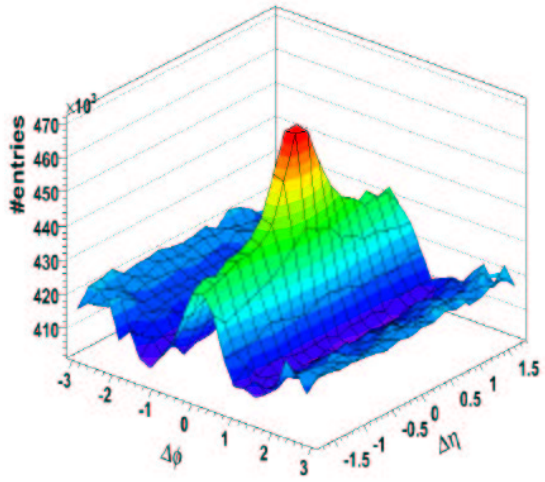

Figure 1.18: Raw $\Delta\eta \times \Delta\phi$ di-hadron correlation function in central Au + Au collisions for $3 < p_T^{trig} < 4$ GeV/c and $p_T^{assoc} > 2$ GeV/c. A large $\Delta\eta$ correlation - ridge is observed.

1.3 Thesis Outline

In this thesis, we present the measurement of di-hadron correlations with respect to (w.r.t.) the reaction plane for Au + Au collisions at $\sqrt{s_{NN}} = 200$ GeV. With the large amount of data sample collected in RHIC Run IV (about 10 times more than the statistics reported in [Ada04c]), and the large acceptance of the TPC which allows us to achieve sufficient event plane resolutions, we present the di-hadron correlations with the trigger particle azimuthal angle w.r.t the reaction plane. This allows us to study the path-length dependence of the parton energy loss in the dense medium from the away-side correlations, and characterize the properties of the ridge phenomenon from the near side correlations. This information will be helpful for understanding the medium characteristics created in heavy ion collisions.

In Chapter 2 we will discuss the facilities used to study heavy ion collisions. The Relativistic Heavy Ion Collider (RHIC) and the detector system - the Solenoidal Tracker At RHIC (STAR) will be described. Chapter 3 contains details of the analysis methods including the anisotropic flow and reaction plane measurements, especially the detail of flow background subtraction in di-hadron correlations. In Chapter 4, we present the results of di-hadron correlations, and in Chapter 5, we discuss these results, focusing on away-side and near-side respectively, and draw conclusions. In Chapter 6, we summarize this analysis and present an outlook for the future work. In the appendices, we include the definition of useful kinematic variables used in this thesis, di-hadron correlation results for each p_T^{trig} and p_T^{assoc} bin, a list of my presentation list and publication list, and the acknowledgement.

CHAPTER 2

Experimental Set-up

2.1 RHIC accelerator

The data used in this thesis is from collisions that were carried out at the Relativistic Heavy Ion Collider (RHIC) at Brookhaven National Laboratory (BNL). RHIC is designed to accelerate and collide heavy ions and polarized protons with high luminosity. The purpose of this extraordinary new accelerator is to seek out and explore new high-energy forms of matter and thus continue the centuries-old quest to understand the nature and origins of matter at its most basic level. RHIC is also designed to deliver polarized proton beams up to center-of-mass energy 500 GeV to carry on vigorous spin scientific programs.

Figure 2.1 shows a diagram of the RHIC machine complex, including a Tandem Van de Graaff facility, a linear proton accelerator, the booster synchrotron, the Alternative Gradient Synchrotron (AGS), and ultimately the RHIC synchrotron ring. For Au beam operations, the Au ions with charge $Q = -1e$ are created using the Pulsed Sputter Ion Source. Then they are accelerated through the Van de Graaff facility and a series of stripping foils, and the Au ions at the exit are with a kinetic energy of 1 MeV/nucleon and a net charge of $Q = +32e$. A bending magnet is used to make the charge selection on the ions. The ions are then injected into the booster synchrotron and accelerated to an energy of 95 MeV/nucleon. After the Au ions leave the booster, they are further stripped to $Q = +77e$ and transferred into the AGS, where they are accelerated to 8.86 GeV/nucleon and sorted into four final bunches. Finally, the ions are injected into

RHIC and stripped to the bare charge state of $Q = +79e$ during the transfer. For $p + p$ operations, protons are injected from the 200 MeV Linac into the booster, followed by acceleration in the AGS and injection into RHIC. Siberian Snakes are used in the AGS and RHIC to preserve the polarization.There are two beam lines throughout the entire acceleration procedure, including two Tandem Van de Graaffs. This allows for two different types of ions, on in each beam line, with which we can get asymmetric collisions, such as deuteron and gold which has been run at RHIC.

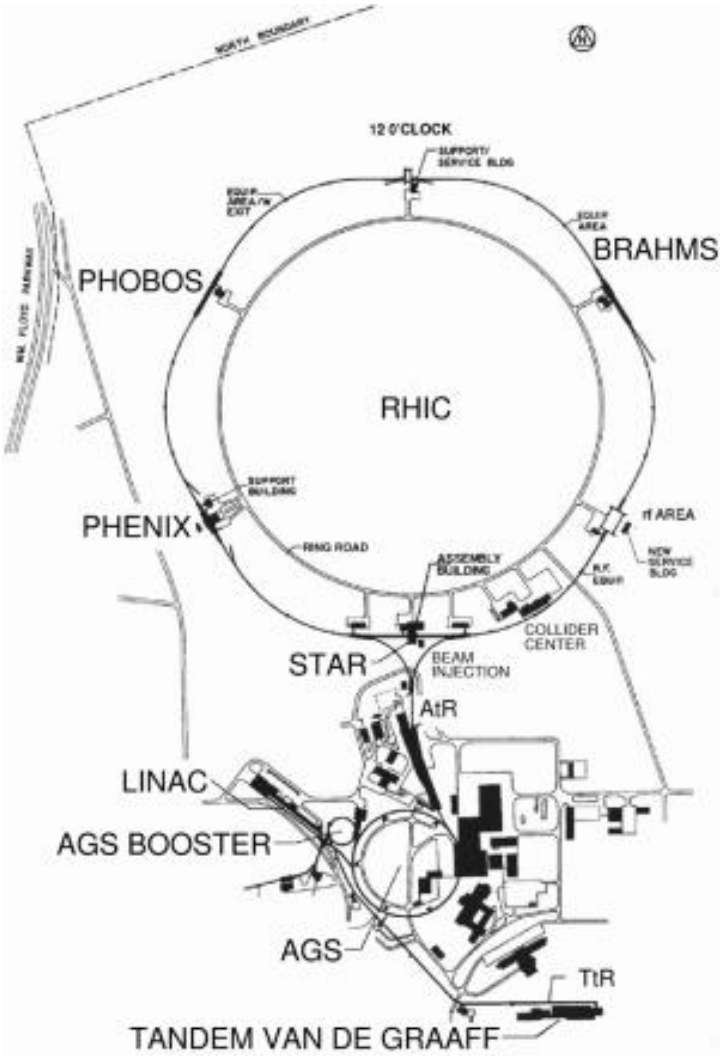

Figure 2.1: Schematic of the RHIC complex. RHIC's two 3.8-kilometer rings collide relativistic heavy ions and polarized protons at six intersection points.

RHIC consists of two concentric super-conducting storage rings that are called blue and yellow rings, respectively. Each ring has its own dependent set of bending and focusing magnets as well as ratio frequency cavities, but both share a common horizontal plane in the tunnel. The RHIC rings have a 3.834 km circumference and has a total of 1700 superconducting magnets cooled to < 4.6 K. The rings have six interaction points, and 4 of them are equipped with detectors. They are two large experiments STAR (6 o'clock), PHENIX (8 o'clock) and two small ones PHOBOS (10 o'clock) and BRAHMS (2 o'clock), respectively.

So far it has collided protons (A=1), deuterons (A=2), copper nuclei (A=63), and gold nuclei (A=197) at various energies ($\sqrt{s_{NN}}$ = 200, 130, 62.4 and 22 GeV). There are future plans to do low energy scans ($\sqrt{s_{NN}} \sim$ 5-20 GeV) with Au + Au collisions to search for the first order phase transition boundary and the critical ending point in the QCD phase diagram.

2.2 STAR detector

The Solenoidal Tracker at RHIC (STAR) is a specially designed detector to track thousands of particles simultaneously produced by each ion collision at RHIC. It has a full 2π azimuthal symmetric acceptance, high precision tracking, momentum determination and particle identification in a large range around mid-rapidity. STAR consists of several subsystems and a main tracker - the *Time Projection Chamber* (TPC) located in a 0.5 T homogenous solenoidal analyzing magnet.

Figure 2.2 shows the cutaway view of the STAR detector. The main tracker - TPC covers the $|\eta| < 1.5$ and 2π in azimuth. The details of TPC detector will be discussed in the next section. There are inner detectors: a three layer *Silicon Vertex Tracker* (SVT) surrounded by an additional layer *Silicon Strip Detector* (SSD) close to the beam pipe, which provides additional high precision space points on track so that it improves the position resolution and allows us to reconstruct the secondary vertex of weak decay

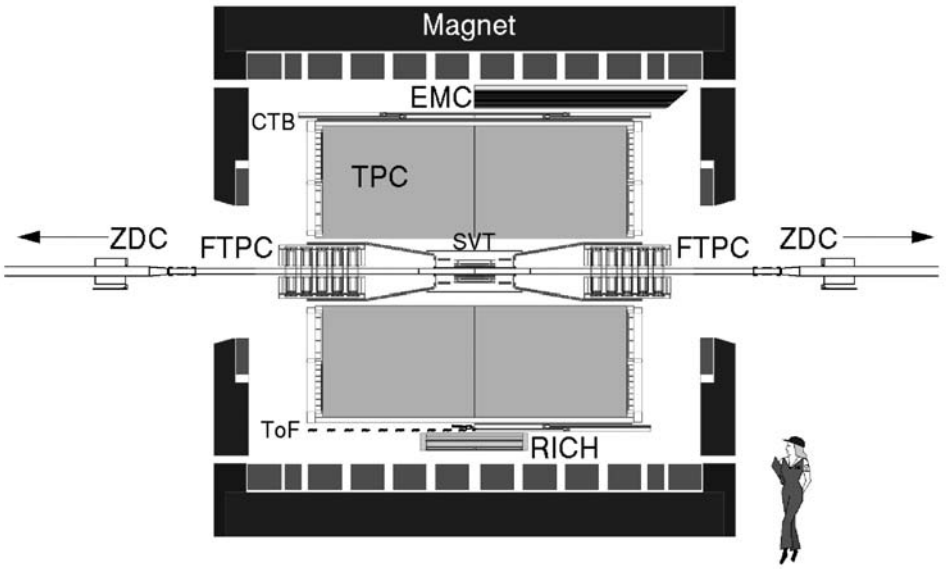

Figure 2.2: Cutaway view of the STAR detector.

particles. There are two *Forward TPC* (FTPC) detectors covering $2.5 < |\eta| < 4$ to track particles at forward and backward rapidity region. There is also a *Time-Of-Flight* (TOF) detector using *Multigap Resistive Plate Chamber* (MRPC) technology at mid-rapidity outside the TPC to extend the PID capability of STAR. The TOF detectors will replace the *Central Trigger Barrel* (CTB) trays in the near future. Outside the TOF detector, there are two *ElectronMagnetic Calorimeters* (EMC) at STAR: the Barrel EMC (BEMC) and the Endcap EMC (EEMC). The BEMC surrounds the TPC while the EEMC is in the front of TPC. These two EMCs provide full azimuthal coverage for the combined pseudorapidity $-1 < \eta < 2$. They are used to measure the electromagnetic probes - electrons and photons.

RHIC has a beam bunch crossing rate of about 10 MHz, while the slow detectors (TPC and FTPC) only operate at rates of about 100 Hz currently. Fast detectors are used to intelligently trigger and select desired events. There are some main trigger detectors: *Zero Degree Calorimeter* (ZDC), CTB and *Beam-Beam Counters* (BBC). Two ZDCs locates on each side $\sim$ 18 m away from the collision points. Each is centered at 0^o and covers $\sim$ 2.5 mrad. The ZDCs are hadronic calorimeters to detect the outgo-

ing neutrons. They are put beyond the dipole magnets which bend away the charged fragments. The ZDC signals are used for monitoring the heavy ion beam luminosity and for the experiments triggers. The CTB is a collection of scintillating tiles covering the whole barrel ektexine of the TPC. The CTB will be mostly used to select central triggered events in heavy ion collisions by measuring the occupancy of those CTB slats. The BBC subsystem covers $3.3 < |\eta| < 5.0$, measuring the "beam-jets" at high rapidity from *Non-Singly Diffractive* (NSD) inelastic $p + p$ interactions. It consists of two disk shaped scintillating detectors, with one placed at each endcap of the TPC (3.5 m from TPC center). Each BBC disk is composed of scintillating tiles that are arranged in a hexagonal closest packing. The $p + p$ NSD trigger sums the output of all tiles on each BBC and requires a coincidence of both BBC's firing above noise threshold within a time window.

In Au + Au minimum bias collisions, cuts are made on the signals in both ZDCs and the CTB. There is also a cut on the primary event vertex obtained from the ZDCs. The ZDC cuts required a coincidence between the two ZDCs of summed signal greater than about 40% of a single neutron signal. The CTB cut is used to reject nonhadronic events which removes events with a very low number of hits in the CTB. This cut rejects some of the desired events that are very peripheral and is why we do not use centralities below the 80% most peripheral. In central Au + Au collisions, there are much higher cuts on the ZDC and the CTB. There is a cut on the primary vertex obtained from the BBCs The cuts are tuned such that the events taken are about 10% of the total cross section and such that the multiplicity distribution matches the minimum bias distribution for the top 5% most central collisions. In d + Au minimum bias collisions, a cut requiring at least one spectator neutron in the outgoing Au beam direction depositing energy in the east ZDC is made.

The STAR magnet is cylindrical in design with a length of 6.85 m and has inner and outer diameters of 5.27 m and 7.32 m, respectively. It generates a field along the length of the cylinder having a maximum of $|B_z| = 0.5$ T. It allows the tracking detectors

to measure the helical trajectory of charged particles to get their momenta. Magnet field mapping is done for all three field components B_r, B_ϕ, and B_z. This was done in 36 azimuthal points, 57 axial locations. This was measured with a steerable array of Hall probes from CERN and supplemented by NMR measurements. The reproducibility of the absolute field is better than $\pm$ 0.5 Gauss. For full magnetic field (0.5 T), the maximum radial field value is $\pm$ 50 Gauss and the maximum azimuthal component is less than 3 Gauss.

2.3 Main tracker - TPC

The TPC (Time Projection Chamber) is the primary tracking device in the STAR detector [And03]. Consisting of a 4.2 m long cylinder with 4.0 m in diameter, it is the largest single TPC in the world. The cylinder is concentric with the beam pipe, and the inner and outer radii of the active volume are 0.5 m and 2.0 m, respectively. It can measure charged particles within momentum $0.15 < p_T/(\mathrm{GeV/c}) < 30$ (0.075 GeV/c low limit for 0.25 T). The TPC covers the full region of azimuth ($0 < \phi < 2\pi$) and covers the pseudorapidity range of $|\eta| < 2$ for inner radius and $|\eta| < 1$ for outer radius. Figure 2.3 shows a cutaway view of the structure of the TPC.

The TPC sits in the middle of the STAR magnet, and it is divided into two parts by the central membrane. A uniform electric field is applied to each part of the TPC, respectively. The electric field is provided by the thin central membrane, the inner and outer concentric field-cages cylinders and readout end caps on the end of the TPC. The central membrane is a disk with a central hole. It is made of 70 μm of carbon-load Kapton film. It is typically held at 28 kV high voltage, thus operated as a cathode of the TPC. The central membrane is mounted in the outer and inner cage cylinders. A chain of 183 resistors and equipotential rings along the inner and outer field cage create the uniform drift filed ($\sim$ 135 V/cm) from the central membrane to the endcap ground planes.

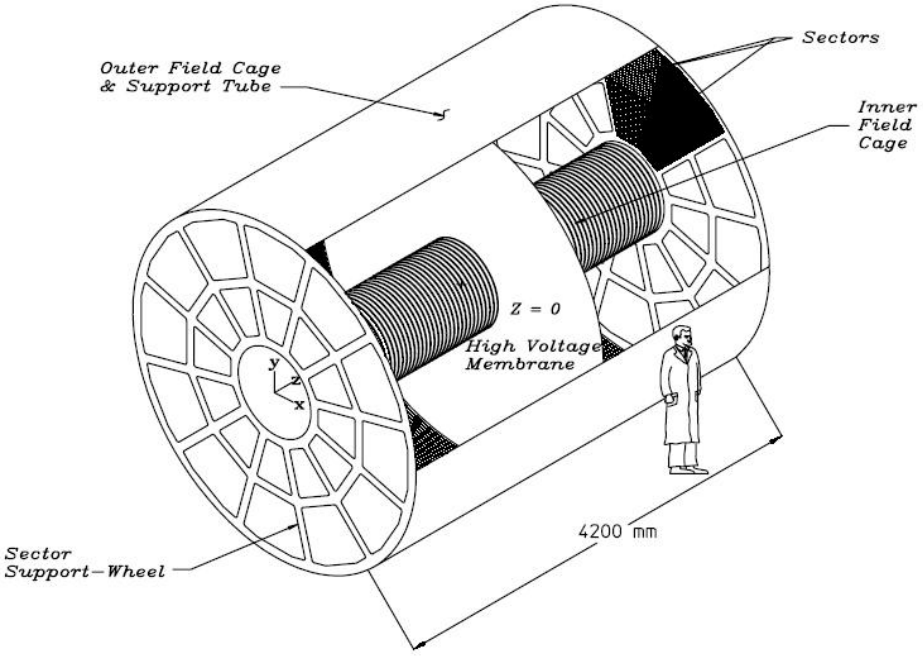

Figure 2.3: Cutaway view of the TPC detector at STAR.

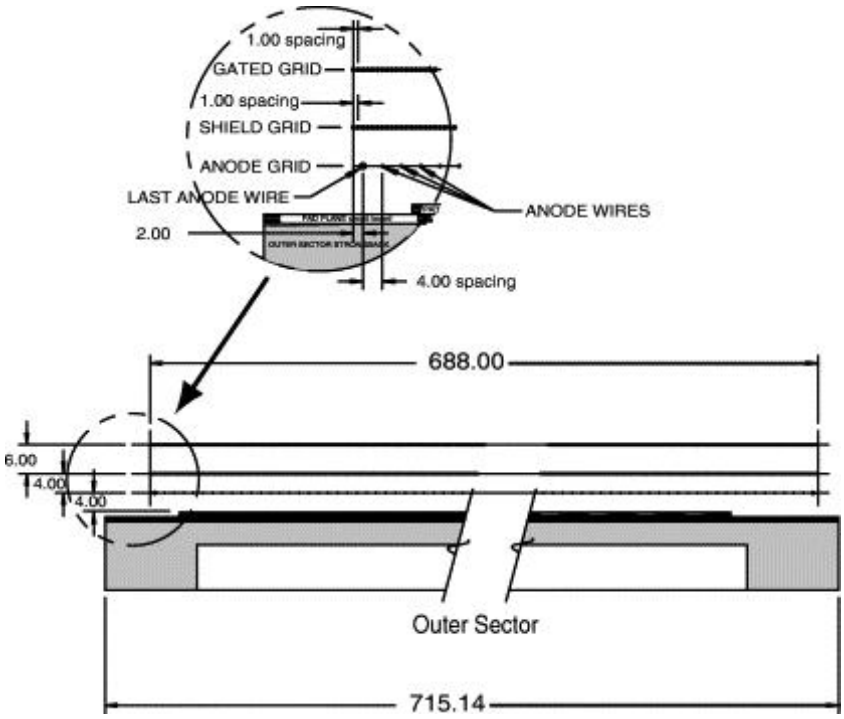

Figure 2.4: Cutaway view of the outer subsector pad and wire planes. All dimensions are in mm.

The TPC end-caps contain anodes and pad planes. The readout planes are *Multi-Wire Proportional Chamber* (MWPC) with pad readout. The chambers consist of three wire planes and a pad plane, which are organized into 12 subsectors for each sub-volume of the TPC. Figure 2.4 shows a cutaway view of the positions of the wires and the pads. The amplification and readout are done by the anode wire planes which consist of 20 μm wires. The wire direction is chosen to best determine the momentum of very high transverse momentum particles whose tracks do not curve much in the magnetic field. This places the anode wires roughly perpendicular to the radial direction. In the other direction, the resolution is limited by the wire spacing (4 mm). The pad dimensions are also optimized to the best position resolution, perpendicular to radial tracks. The pad dimensions are chosen such that the induced charge from an avalanche point on the anode wires shares most of its signal with three pads. The outer radius subsectors are optimized for the best possible energy loss resolution, while the inner radius subsectors are optimized for good two-hit resolution due to high track density in that region. Figure 2.5 shows one sector of the inner and outer pads. 136,608 readout pads provide (x, y) coordinate information, while z coordinate is provided by 512 time buckets and the drift velocity. Typical resolution is $\sim 0.5 - 1.0$ mm. The anode wires voltage is set independently for the two sectors. A ground grid plane of 75 μm wires is used to terminate the field in the avalanche region and provide additional shielding for the pads. The anodes, pad, and grounding grids make up the MWPC.

The working gas of the TPC is two gas mixture − P10 (Ar 90% + CH_4 10%) regulated at 2 mbar above the atmospheric pressure. The electron drift velocity in P10 is relatively fast, $\sim$ 5.45 cm/μs at 130 V/cm drift field. The gas mixture must satisfy multiple requirements and the gas gains are ~ 3770 and ~ 1230 for the inner and outer sectors working at normal anode voltages (1170 V for inner and 1390 V for outer), respectively.

When charged particles traverse the TPC, they liberate the electrons from the TPC gas due to the ionization energy loss (dE/dx). These electrons are drifted towards the end cap planes of the TPC. There the signal induced on a readout pad is amplified and

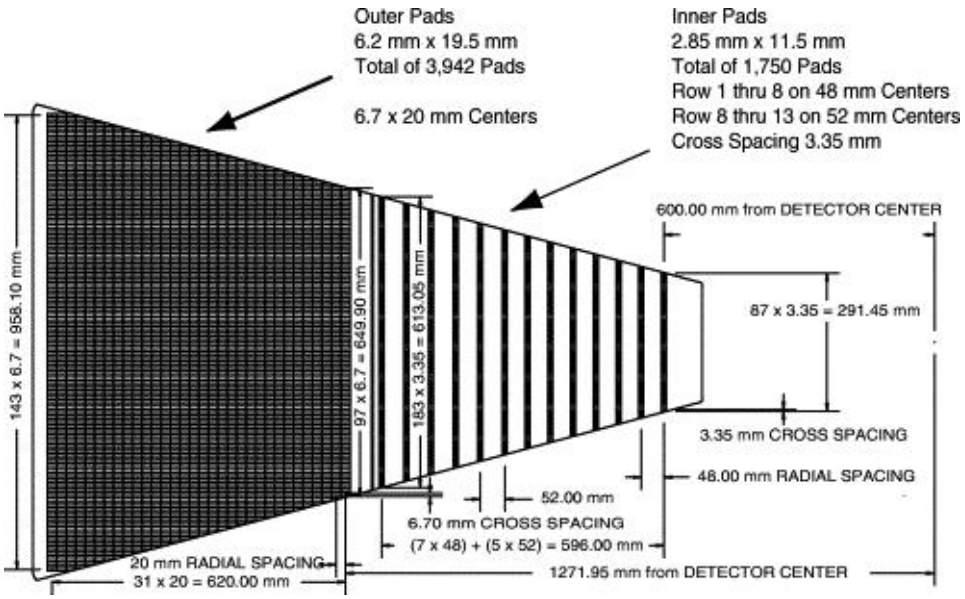

Figure 2.5: The pad plane of one TPC sector. The inner subsector is to the right and the outer subsector is to the left.

integrated by a circuit containing a pre-amplifier and a shaper. Then it is digitalized and then transmitted over a set of optical fibers to STAR *Data AcQuisition system* (DAQ).

The TPC reconstruction process begins by the 3D coordinate space points finding. This step results in a collection of points reported in global Cartesian coordinates. The *Timing Projection chamber Tracker* (TPT) algorithm is then used to reconstruct tracks by helical trajectory fit. The resulted track collection from the TPC is combined with any other available tracking detector reconstruction results and then refit by application of a Kalman filter routine − a complete and robust statistical treatment. The primary collision vertex is then reconstructed from these global tracks and a refit on these tracks with the *distance of closest approach* (*dca*) less the 3 cm is preformed by a constrained Kalman fit that forces the track to originate from the primary vertex. The primary vertex resolution is ~ 350 μm with more than 1000 tracks. The refit results are stored as primary tracks collection in the container. The reconstruction efficiency including the detector acceptance for primary tracks depends on the particle type, track quality cuts, p_T , track multiplicity *etc.* The typical value for the primary pions with $N_{fit} > 24$ and

$|\eta| < 0.7$, $dca < 3.0$ cm is approximate constant at $p_T > 0.4$ GeV/c: $>\sim 90\%$ for Au + Au peripheral collisions and $\sim 80\%$ for central collisions, respectively.

The TPC can also identify particles by the dE/dx of charged particles traversing the TPC gas. The mean rate of dE/dx is given by the Bethe-Bloch equation 2.1 [Yao06]:

$$-\frac{dE}{dx} = Kz^2\frac{Z}{A}\frac{1}{\beta^2}\left[\frac{1}{2}\ln\frac{2m_ec^2\beta^2\gamma^2T_{max}}{I^2} - \beta^2 - \frac{\delta}{2}\right] \tag{2.1}$$

The meaning of each symbol can be referred to [Yao06]. Different types of particles (different rest masses) with the same momentum have different kinematic variables β (γ), which may result in distinguishable dE/dx. The typical resolution of dE/dx in Au + Au collisions is $\sim 8\%$, which makes the π/K separation up to $p \sim 0.7$ GeV/c and proton/meson separation up to $p \sim 1.1$ GeV/c.

Additionally, a new recent technique was developed to identify high momentum ($p >$ 3 GeV/c) pions and protons in the relativistic rising region of dE/dx [Sha06] benefiting from the advantage that the mean rates of dE/dx for different particles have a visible separation in the relativistic rising region ($\sim 2\sigma$ separation for pions and protons). Due to large acceptance of the TPC, using the topology of their weak decay in the TPC, the K^0_S, $\Lambda(\bar{\Lambda})$ *etc.* can be identified across p_T region $0.3 < p_T/(\text{GeV/c}) < 7.0$ (upper edge limited by statistics). Resonances (K^*, ϕ, Δ *etc.*) can be reconstructed through the event mixing technique [Adl02b]. Figure 2.6 shows the PID capabilities up to date with the TPC. In addition, the TOF PID capability is also shown on the plot.

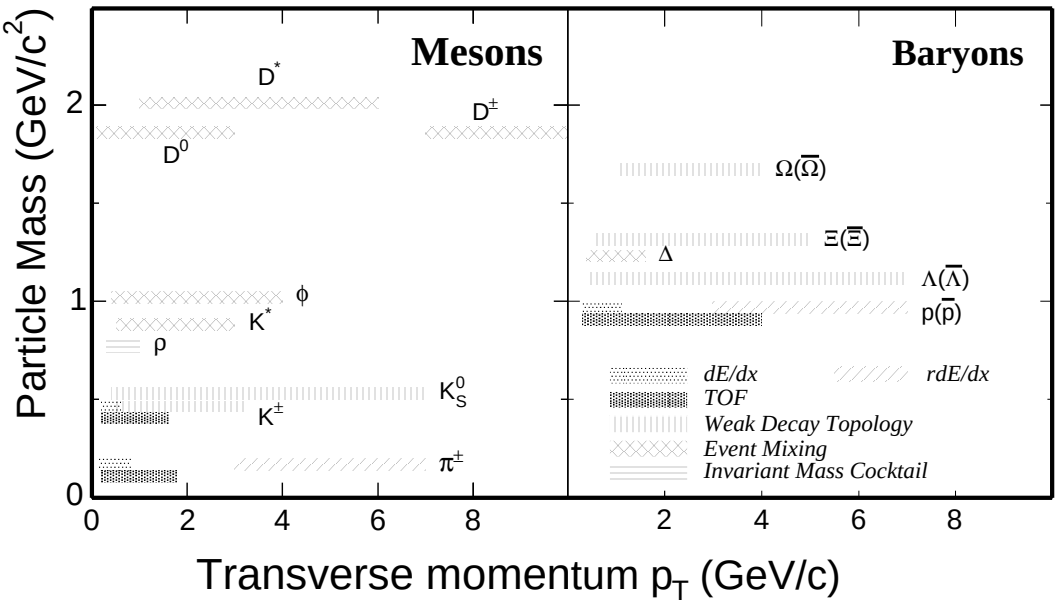

Figure 2.6: p_T reach of particle identification capability with STAR detectors for Run II and Run III configurations. The upper edges of rdE/dx, weak decay topology, event mixing are limited by statistics.

CHAPTER 3

Analysis Method

High transverse momentum (p_T) partons which evolve to final jets are valuable probes of the high energy density matter created at the Relativistic Heavy-Ion Collider (RHIC). This is because the properties of jets in elementary collisions can be calculated reliably by perturbative QCD (pQCD). The comparison between simple $p + p$ collisions and Au + Au collisions may reveal the property of jets which are modified by the dense medium created at RHIC and the properties of the medium which is affected by jets due to the strong interactions between them.

The well-known jet quenching scenario predicts that these high transverse momentum partons will interact with the medium and lose a large fraction of their energy in the medium prior to forming hadrons and the energy loss depends on the gluon density and the path-length that the away-side parton traverses. The current experimental observations on the suppression of high p_T particles and the disappearance of back-to-back jets are successfully explained by the energy loss picture predicted in jet quenching. Further investigating the path-length effect or the gluon density effect described in jet-quenching will be very interesting and meaningful.

However, in heavy-ion collisions, very large amount of particles are produced. It is not possible to reconstruct jets event by event due to the large background. So in heavy-ion collisions people reconstruct jet-like correlations through angular correlations in statistical basis. In two-particle correlations (di-hadron correlations) this is done by triggering on an intermediate or high p_T particle and studying the angular distributions of the other particles in the event with respect to the trigger particle. This is the method

used in this thesis. We concentrate the di-hadron correlations relative to reaction plane to study the dependence of correlations on the trigger particle orientation with respect to reaction plane, thus examine the path-length effect predicted in jet-quenching.

3.1 Motivation

For the di-hadron azimuthal correlations with a high p_T trigger particle, as mentioned before, we have already got several key measurements.

The strong suppression on the away-side of high p_T di-hadron correlation lends strong support for the partonic energy loss (jet quenching) picture. While the enhancement on the away-side of di-hadron correlation with softer associate particles explains where the lost energy from high p_T partons is and indicates the strong jet-medium interaction. Moreover, the first investigation from STAR experiment results on di-hadron correlation with trigger particle in plane and out of plane is consistent with the jet quenching picture and gives us a hint about the path-length effect described in jet-quenching.

Inspired by this first simple investigation, we are going to explore the path-length effect in greater details by observing the away-side modification via finer selection of trigger particle direction with respect to reaction plane. Besides the away-side study, the near-side properties relative to reaction plane may be investigated simultaneously.

3.2 Di-hadron Azimuthal Correlation

The defining characteristic of a jet is the production of a large number of particles clustered in a cone in the direction of the fragmenting parton. Traditionally, energetic jets are identified directly using standard jet reconstruction algorithms [Cat93]. In heavy ion collisions, the large amount of soft background makes direct jet reconstruction difficult. Even in d + Au or $p + p$ collisions, the range of energy accessible to direct jet reconstruction is probably limited to $p_T > 5 - 10$ GeV/c, below which the jet cone becomes

too broad and contamination from the "underlying event" background is significant.

The di-hadron(two-particle) azimuthal correlation technique provides an alternative way to access the properties of jets. It is based on the fact that the fragments are strongly correlated in azimuth ϕ and pseudorapidity η. Thus, the jet signal manifests itself as a narrow peak in $\Delta\phi$ and $\Delta\eta$ space. Jet properties can be extracted on a statistical basis by accumulating many events to build a $\Delta\phi$ distribution or a $\Delta\phi$ correlation function with known sources of background correlations subtracted.

In more details, events with at least one large transverse momentum hadron ($3 < p_T^{trig} < 4$ GeV/c or $4 < p_T^{trig} < 6$ GeV/c in this analysis), defined as a trigger particle, are used. These high p_T particles may predominantly come from jets of hard-scattering partons. The selection of high p_T particles preferentially triggers on jets. For each of the trigger particles in the event, we increment the number $N(\Delta\phi, \Delta\eta)$ of associated tracks with lower transverse momentum as a function of their azimuthal ($\Delta\phi$) and pseudorapidity ($\Delta\eta$) separations from the trigger particle. We then construct an overall azimuthal pair distribution per trigger particle,

$$D(\Delta\phi) \equiv \frac{1}{N_{trigger}} \int \frac{1}{\varepsilon(p_T, \eta)} d\Delta\eta N(\Delta\phi, \Delta\eta) \tag{3.1}$$

where $N_{trigger}$ is the observed number of tracks satisfying the trigger requirement. The correlation is normalized to per trigger particle, not per event, because we are interested in quantities on a per-jet basis. The efficiency ε for finding the associated particles is evaluated by embedding simulated tracks in real data.

Besides this tracking efficiency correction, Another 2-particle acceptance correction got from mixed-event method is also applied in this analysis: A trigger particle is selected from one event and the associated particles are taken from a different event to construct the $\Delta\phi$ distribution. Normalizing this mixed distribution may approximately obtain the pair acceptance. The mixed events must be of the same centrality as the one that the trigger particle in. And no other conditions are placed on the mixed events so that they will be referred to as inclusive events.

Applying the analysis procedure to the $p + p$ collisions where jets properties in absence of medium can be calculated and well understood by perturbative quantum chromodynamics, two approximately Gaussian-shape jet cone can be observed on the near-($\Delta\phi = 0$) and away-side ($\Delta\phi = \pi$) (see the $p + p$ results in Figure 1.17 for reference), which is contributed from di-jets.

Due to the complexity in Au + Au collisions, the comparison of the measurements with simple system $p + p$ may help us to understand the modification on jets from the medium and the nature of the medium. This comparison has been previously studied in [Ada04c]. And the comparison with system d + Au will allow us to disentangle initial state nuclear effects from other effects seen in Au + Au collisions when compared to p + p collisions. In this thesis, results from d + Au collisions are used as a reference.

3.3 Di-hadron Azimuthal Correlation With Respect to Reaction Plane

In this thesis, we study the path-length effect by exploiting non-central collisions ($20 - 60\%$) where the overlap region between the two colliding nuclei is anisotropic: the size in the reaction plane direction is shorter than that perpendicular to reaction plane. We divide the ϕ space into 6 small slices with the equal size (each slice has $\Delta\phi = 15°$, see Figure 3.1) according to the direction of reaction plane. From the in-plane direction to out-of-plane, we name it slice 1, slice 2, slice 3 ... through slice 6. Then study the di-hadron correlations requiring that the trigger particle azimuthal direction is in each slice. Thus, by selecting the trigger particle direction with respect to reaction plane, we select different path-lengths of the medium that the away-side parton traverses, providing more differential information than the inclusive jet-correlation measurements. The path-length that away-side parton traverses in the reaction plane direction is the shortest. It becomes longer when the trigger particle goes from in-plane to out-of-plane and reaches longest

one in the out-of-plane direction. This can be easily seen from the cartoon (Figure 3.1). The comparison of so measured di-hadron correlation results with trigger particles in each slice will give us the information whether there is the path-length effect.

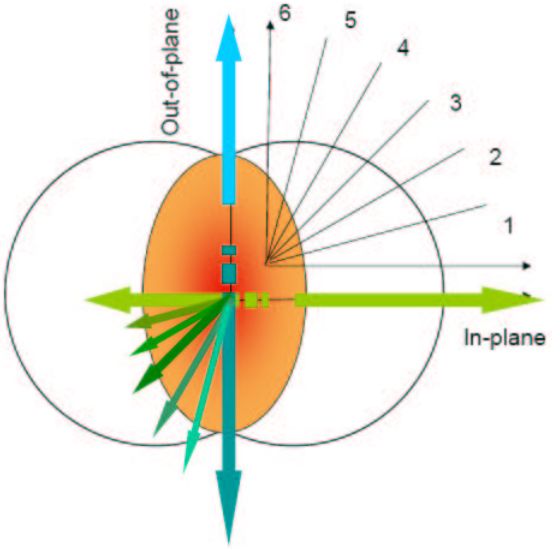

Figure 3.1: Sketch of 6 slices of trigger particle azimuthal angle relative to event plane. The path-length away-side parton transverses becomes longer from in-plane to out-of-plane.

3.4 Event and Track Selection

The data used in this analysis were taken by the STAR experiment at RHIC. The main detector used for this analysis is the Time Projection Chamber (TPC). The details of the experiment and detector have been discussed in Chapter 2.

We use the minimum bias Au + Au data and the ZDC trigger central Au + Au data in this analysis. They were from Run IV at RHIC. The reference minimum bias d + Au data used for comparison were from Run III. The nucleon-nucleon center of mass energy for both data is 200 GeV. The minimum bias triggers for Au + Au and d + Au collisions

were provided by the Central Trigger Barrel (CTB) and the Zero Degree Calorimeters (ZDC). The online central trigger for Au + Au collisions, corresponding to 12% of the total geometrical cross-section, was provided by an additional cut on the ZDC signal. The high multiplicity events selected from this ZDC trigger sample, corresponding to 5% of the total geometrical cross-section, are identical to the top 5% events from the minimum bias data sample.

The tracks are reconstructed in the TPC. There are two kinds of reconstructed tracks. One is the global track, the other is the primary track. The global track is defined by the helix fit to the TPC points one by one. The collision vertex can be identified from all the reconstructed global tracks. The primary track is defined by the helix fit to the TPC points along with the vertex. The primary event vertex was fitted by the reconstructed global tracks. Events with a primary vertex within ±30 cm of the geometric center of the TPC along the beam axis are accepted. Only primary tracks pointing to the primary event vertex within 2 cm are used in the analysis. Tracks are required to have at least 20 (out of maximum 45) hits used in track fitting. The ratio of the number of hits used in tracking fitting to the possible maximum number of hits is required to be greater than 0.51 to eliminate split tracks. The same event and track cuts are applied to particle tracks used for event plane reconstruction and for the subsequent correlation analysis. Particle tracks within the pseudo-rapidity region of $|\eta| < 1$ are used in the correlation analysis. The track cuts are listed in table 3.1.

Dca Cut	NFitPoints	NFitOverMaxPoints	Eta Cut	p_T Cut
< 2.0 cm	> 20	> 0.51	< 1.0	> 0.15 GeV/c

Table 3.1: The track cuts in this analysis for Au + Au collisions at $\sqrt{s_{NN}} = 200$ GeV. Same track cuts are used in both event plane reconstruction and the correlation analysis.

The number of tracks (i.e. multiplicity) measured by the main TPC are used to define the STAR's centrality intervals. The TPC reference multiplicity is the number of the primary tracks in the TPC with the 15 or more fit points having the pseudo-rapidity

from -0.5 to 0.5 and a distance of closet approach (DCA) to the primary vertex less than 3 cm. Nine centrality bins and the corresponding geometric cross section are listed in Table 3.2. A part of low multiplicity events are rejected due to a lower cut on CTB to reject the non-hadronic events. The geometric cross section listed in Table 3.2 is the fraction of the corrected total number of events.

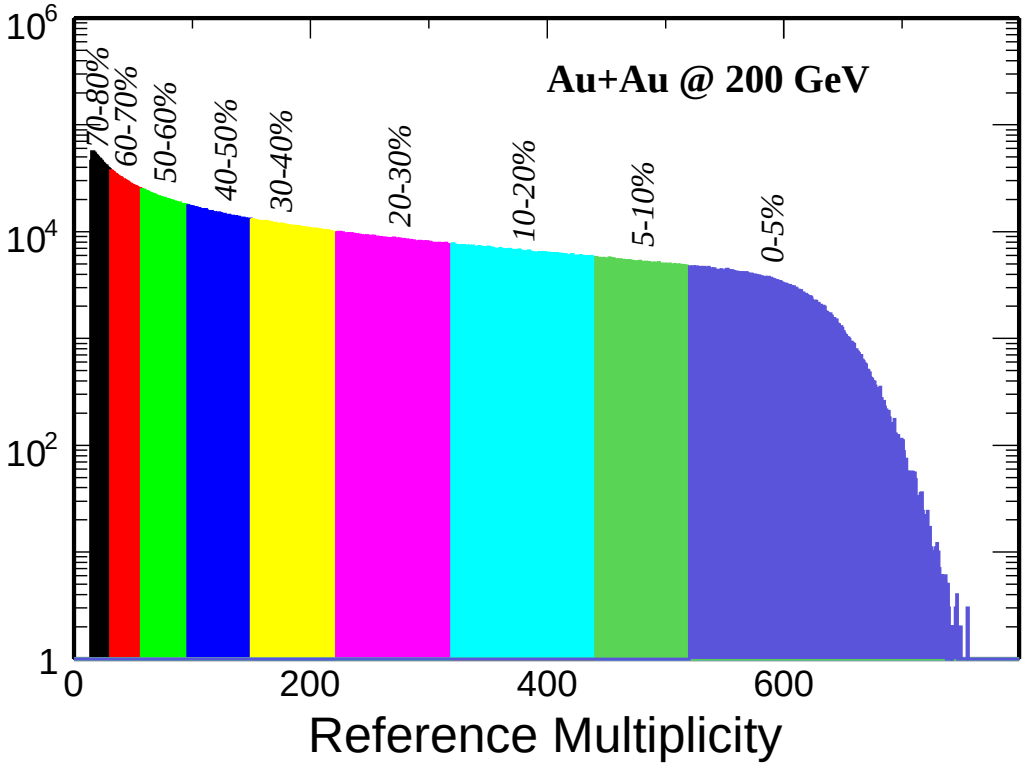

Figure 3.2: (color online) The TPC charged particle multiplicity distribution in Au + Au collisions at $\sqrt{s_{NN}}$ = 200 GeV. Different colors are for different centrality definition. x-axis indicates the number of the reference multiplicity. The geometry cross section used for this di-hadron analysis is combined from 4 centrality intervals ($20-30\%, 30-40\%, 40-50\%$ and $50-60\%$).

Figure 3.2 shows charged particle multiplicity distribution. Events with centrality bins between 20% and 60% are used in the analysis.

Centrality Bin	Multiplicity	Geometric Cross Section
1	14-31	70%-80%
2	31-57	60%-70%
3	57-96	50%-60%
4	96-150	40%-50%
5	150-222	30%-40%
6	222-319	20%-30%
7	319-441	10%-20%
8	441-520	5%-10%
9	> 520	0%-5%

Table 3.2: Run IV centrality bins in Au + Au collisions at $\sqrt{s_{NN}} = 200$ GeV.

3.5 Anisotropic Flow and Event Plane

The reconstruction of reaction plane is very important in this analysis since we study the jet modification with respect to reaction plane. Another important thing in the analysis is the well known anisotropic flow as its precision is relative to the veracity of the estimation of background. The two things are mainly discussed in this section.

3.5.1 Anisotropic Flow

In heavy ion collisions, the size and shape of the collision region depend on the distance between the centers of the nuclei in the transverse plane (impact parameter b).

In non-central collisions, the overlapping reaction zone of two colliding nuclei is not spherical, it has the shape like an almond (see Figure 3.3) . Rescatterings among the system's constituents convert the initial coordinate-space anisotropy into a momentum-space anisotropy since the pressure gradient is not azimuthally symmetric, see Figure 3.4. The spatial anisotropy is largest in early time of the evolution of the collision. As the system expands it becomes more spherical, thus this driving force quenches itself.

Therefore the momentum anisotropy is particularly sensitive to the early stages of the system evolution [Sor99]. In addition, because anisotropic flow depends on rescattering, it is sensitive to the degree of the thermalization [VP00, KSH00] of the system at early time.

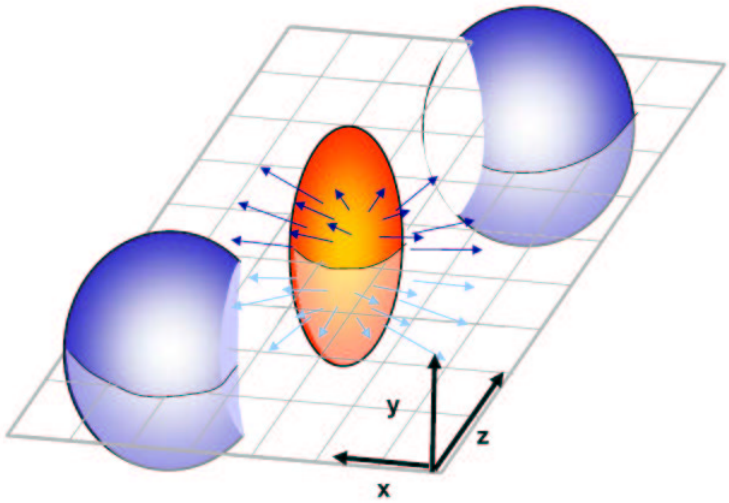

Figure 3.3: Sketch of an almond shaped fireball produced in non-central collisions, where z direction is the collision axis.

Usually, anisotropic flow is quantified by the Fourier expansion of the triple differential distribution [VZ96].

$$E\frac{d^3N}{d^3p} = \frac{1}{2\pi}\frac{d^2N}{p_T dp_T dy}(1 + \sum_{n=1}^{\infty} 2v_n \cos[n(\phi - \Psi_r)]) \tag{3.2}$$

where Ψ_r denotes the (true) reaction plane azimuthal angle. The azimuthal angle of an outgoing particle is given by ϕ and n is a positive integer corresponding to the n-th order harmonics. The sine terms vanish due to the reflection symmetry with respect to the reaction plane.

The Fourier coefficients are given by

$$v_n = \langle \cos(n(\phi - \Psi_r)) \rangle \tag{3.3}$$

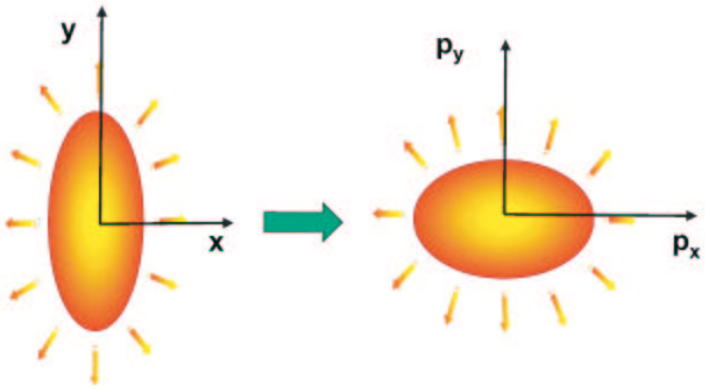

Figure 3.4: Sketch of the formation of anisotropic flow.

where $\langle ... \rangle$ indicates an average over the particles in all events under study. The first order harmonics v_1 and the second order harmonics v_2 are usually called directed flow and elliptic flow, respectively.

The general method for measuring flow is the one called event plane method. The measurement includes three steps. Firstly, the essence is to estimate the reaction plane. Secondly, the estimated Fourier coefficients in the expansion of the azimuthal distribution of emitted particles is evaluated with respect to the event plane. Thirdly, the Fourier coefficients are corrected with the event plane resolution. The event plane resolution is the limited resolution between the angle of measured reaction plane and the real reaction plane. Step 1 and 3 will be discussed in following sections.

Other methods like 4-particle and 2-particle cumulant methods avoid the reconstruction of reaction plane. The flow values given by these methods have small non-flow effect. We will not discuss the two methods in this thesis.

3.5.2 Event Plane Reconstruction

The reaction plane is defined by the impact parameter vector $\overrightarrow{b}$ and the beam direction. The estimated reaction plane we call the event plane. The reaction plane can be

reconstructed only if the final state of the interaction products retains some memory (azimuthal asymmetry) of the initial collision geometry. Usually the method uses the anisotropic flow itself to determine the event plane. It also means the event plane can be determined independently for each harmonic of the anisotropic flow.

The event plane vector $\overrightarrow{Q_n}$ and the event plane angle ψ_n from the nth harmonic of the particle's azimuthal distribution are defined by the equations

$$Q_n \cos(n\Psi_n) = X_n = \sum_i w_i \cos(n\phi_i) \tag{3.4}$$

$$Q_n \sin(n\Psi_n) = Y_n = \sum_i w_i \sin(n\phi_i) \tag{3.5}$$

$$\Psi_n = \left(\tan^{-1} \frac{\sum_i w_i \sin(n\phi_i)}{\sum_i w_i \cos(n\phi_i)} \right) / n \tag{3.6}$$

The sum goes over all the particles used in the event plane determination. These particles are called flow tracks. The w_i are weights. Usually the weights are assigned with the transverse momentum. This choice of weights is to make the reaction plane resolution the best by maximizing the flow contributions to the flow vector.

In this analysis, we use the second flow harmonic to determine the event plane angle. Note that the event plane angle Ψ_2 is in the range $0 < \Psi_2 < \pi$. The flow track selection criteria are listed in Table 3.3.

Flow track selection criteria	
nHits	> 20
nHits/nMax	> 0.51
dca	< 2 cm
transverse momentum	$0.15 < p_T < 2.0$ GeV/c
pseudo-rapidity	$\|\eta\| < 1.0$

Table 3.3: Selection criteria for flow tracks used in the event plane reconstruction

What should be mentioned here are some additional techniques used in this analysis when determining the event plane:

• Avoidance of Auto-correlation: The particles used in estimating the event plane are soft particles which p_T is below 2.0 GeV/c. However the particles used as associated particles in this analysis are also low p_T particles. The multiple use of the same particles will result in auto-correlations. To avoid auto-correlation, particles in the interesting p_T bin that are used for correlation analysis are excluded from event plane reconstruction. For example, for associated p_T^{assoc} bin of $1.0 < p_T^{assoc} < 1.5$ GeV/c, the particles used to calculate the event plane are from p_T ranges of $0.15 < p_T < 1.0$ GeV/c plus $1.5 < p_T <$ 2.0 GeV/c.

• Modified Reaction Plane: Non-flow effect such as di-jet production can influence the determination of the event plane. Imaging that a di-jet aligns with reaction plane, it will result in better event plane determination. However, a di-jet perpendicular to reaction plane will give worse event plane estimation. So taking the jet effect into account, we exclude particles within $|\Delta\eta| < 0.5$ of the highest p_T particle in the event from the event plane construction. This method is called the modified reaction plane (MRP) method [Ada05c].

• Flattening of Reaction Plane: Biases due to the finite acceptance of the detector which cause the particles to be azimuthally anisotropic in the laboratory system should be removed by making the distribution of event planes isotropic in the laboratory. There are several different methods to remove it [Pos05]. In this analysis, we use the most commonly used method. In this method, the distribution of the particles themselves is used as a measure of the acceptance [Bar97a, Bar97b, App98]. One accumulates the laboratory azimuthal distribution of the particles for all events and uses the inverse of this as weights in the calculation of the event planes. This is done centrality by centrality. Figure 3.5 shows the event plane distribution before (left) and after (right) this correction. After the ϕ angle acceptance correction, the anisotropy event plane distribution becomes flat.

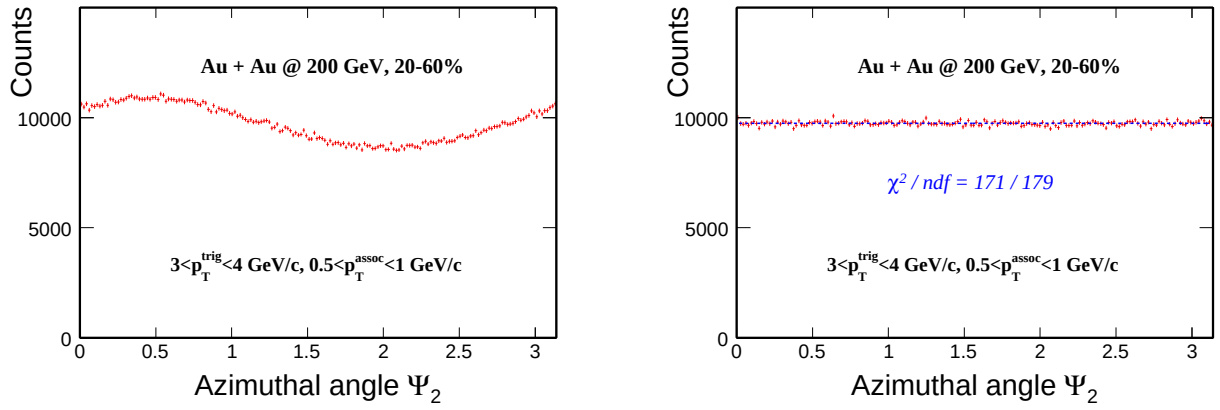

Figure 3.5: An example of event plane angle distribution before(left) and after(right) $phi-$weight correction. It's for Au + Au collisions at $\sqrt{s_{NN}}$ =200 GeV.

• p_T-weight Method: We use particles transverse momentum as weight parameter in estimating event plane. This gives better event plane reconstruction due to the stronger anisotropy at larger p_T.

3.5.3 Event Plane Resolution

As mentioned in Section 3.5.1, The general flow measurement includes three steps and the final step is that the observed anisotropic flow should be corrected by the event plane resolution. This is because the observed flow is correlated to the event plane. Due to finite multiplicity in the event plane calculation, there are some uncertainties between the event plane and real reaction plane. The observed anisotropic flow corrected by the event plane resolution, is given by Equation 3.7 [PV98].

$$v_n = \frac{v_n^{obs}}{\langle \cos[km(\Psi_m - \Psi_r)] \rangle} \tag{3.7}$$

The mean cosine deemed as the event plane resolution sums over the whole event sample. Where v_n, v_n^{obs}, Ψ_m and Ψ_r are the real v_n, observed v_n, the event plane angle calculated from the m-th harmonic flow and the real reaction plane angle. The resolution depends both on the harmonic used to determine the event plane m and the order of

the calculated coefficient n ($n = km$). It is generally true that better accuracy for the determination of v_n is achieved by using the event plane (Ψ_n) determined from the same harmonic ($m = n$). According to paper [PV98], the event plane resolution can be expressed as Equation 3.8.

$$\langle\cos[km(\Psi_m - \Psi_r)]\rangle = \frac{\sqrt{\pi}}{2\sqrt{2}}\chi_m \exp(-\chi_m^2/4) \times [I_{(k-1)/2}(\chi_m^2/4) + I_{(k+1)/2}(\chi_m^2/4)] \quad (3.8)$$

where $\chi_m \equiv v_m/\sigma$ ($= v_m\sqrt{2N}$ for number flow) and I_ν is the modified Bessel function of order ν. However, this equation indicates a circular calculation between event plane resolution and flow. The investigation on the correlation between flow angles of independent sets of particles will lighten us on this problem. If one constructs the event planes in two different windows, (a) and (b), the corresponding correlation function also can be written analytically. But more important in this case is the simple relation of such correlations,

$$\langle\cos[n(\Psi_m^a - \Psi_m^b)]\rangle = \langle\cos[n(\Psi_m^a - \Psi_r)]\rangle \times \langle\cos[n(\Psi_m^b - \Psi_r)]\rangle \quad (3.9)$$

The assumption made here is that there are no other correlations except the ones due to flow, or that such correlations can be neglected. This relation permits the evaluation of the event plane resolution directly from the data. For two sub-events with equal multiplicity, the resolution for each of them is

$$\langle\cos[n(\Psi_m^a - \Psi_r)]\rangle = \sqrt{\langle\cos[n(\Psi_m^a - \Psi_m^b)]\rangle} \quad (3.10)$$

In Equation 3.10, the expression on the left side is not computable directly due to the unknown variable Ψ_r, while we may calculate it via the expression on the right side from data. Thus, the sub-event plane resolution $\langle\cos[n(\Psi_m^a - \Psi_r)]\rangle$ is obtained. And the full event plane resolution can be calculated from the sub-event resolution by following the steps below.

Firstly, solve the Equation 3.8 but with Ψ_m^a instead of Ψ_m, χ_m^a instead of χ_m, e.g. solve the Equation 3.11 to get the value of χ_m^a.

$$\langle\cos[km(\Psi_m^a - \Psi_r)]\rangle = \frac{\sqrt{\pi}}{2\sqrt{2}}\chi_m^a \exp(-\chi_m^{a2}/4) \times [I_{(k-1)/2}(\chi_m^{a2}/4) + I_{(k+1)/2}(\chi_m^{a2}/4)] \quad (3.11)$$

Secondly, we may get χ_m from the relation of $\chi_m \equiv v_m/\sigma$ $(= v_m\sqrt{2N})$. This is because the flow signal is the same for the same event so $\chi_m = v_m\sqrt{2N} = \frac{\chi_m^a}{\sqrt{2\times\frac{N}{2}}} \times \sqrt{2N}$=$\sqrt{2}\chi_m^a$.

Finally, using the obtained χ_m and bringing it into Equation 3.8 one can get the full event plane resolution $\langle\cos[km(\Psi_m^a - \Psi_r)]\rangle$.

Actually, if the flow signal is weak, which also means that the event resolution is low, the full event plane resolution will approximately linearly increase with χ_m. Taking into account that the multiplicity of the full event is twice as large as that of the sub-event, one can write the full event plane resolution in a simple equation 3.12,

$$\langle\cos[n(\Psi_m - \Psi_r)]\rangle = \sqrt{2}\langle\cos[n(\Psi_m^a - \Psi_r)]\rangle = \sqrt{2} \times \sqrt{\langle\cos[n(\Psi_m^a - \Psi_m^b)]\rangle} \tag{3.12}$$

Generally, for this case we have

$$\langle\cos[n(\Psi_m - \Psi_r)]\rangle = C \times \sqrt{\langle\cos[n(\Psi_m^a - \Psi_m^b)]\rangle} \tag{3.13}$$

where C is a correction [PV98] for the difference in sub-event multiplicity compared to the full event.

These equations (approximate solutions Eq. 3.12 and 3.12 and rigorous solution) allow us to estimate the event plane resolution from the two sub-events which are divided from the full event into two windows (a) and (b). For each sub-event, the event plane has been evaluated independently. We call it sub-event method.

There are several ways to separate the whole event into two sub-events in sub-event method. The division may according to η or charge sign or by dividing all flow tracks into two parts randomly. For example, in charge-sign dependent dividing method two sub-event planes for the same event are reconstructed using tracks with charge > 0 and charge < 0, representing the $\Psi^a(q > 0)$ and $\Psi^b(q < 0)$, respectively. In η sign dependent dividing method one may divide the full event into two part by choosing two η range. The event plane resolution is calculated with this two independent sub-event angle according to Equation 3.13.

Finally, to emphasize here, we use the rigorous solution to get the full event plane resolution. The second harmonic flow is used to determine the reaction plane in this analysis, which means for all above equations, just simply using 2 instead of n and 1 instead of k can achieve the method of calculating event plane applied in our analysis. And our event resolution is got from the randomly dividing two sub-events method. The resolution obtained from the charge-sign dependent sub-event method is used to estimate the systematic errors in flow background caused by the uncertainty of event plane resolution.

3.6 Flow Background and v_4 Contribution

In Au + Au collisions, multiple processes can contribute to di-hadron correlation function (Equation 3.1). Primary contributions include jets, mini-jets, resonance decays and anisotropic flow. To obtain the jet information (correlations from jets), one need to subtract other sources, which we call background, contributed to the correlation function. Among these background sources, anisotropic flow is the main contributor. And all the background particles (no matter what origins they are from) are represented by the flow background. This is because on one hand, background particles, by definition, are not correlated with the trigger particle, therefore they should be represented by the inclusive events, and on the other hand, the flow measurements are done by inclusive events which include all contributors. So after subtracting the measured flow background, we may get the jet signals. In following two sections, we are going to discuss how the flow contributes to the correlation function and estimate the magnitude that the higher harmonic flow contributes respectively.

3.6.1 Flow Background Estimation

The azimuthal anisotropy in the angle difference $\Delta\phi = \phi_i - \phi_j$ $(0 \leq \Delta\phi \leq \pi)$ of particle pairs which is generated from collective flow are given by [Wan91],

$$\frac{dN^{pairs}}{\pi d\Delta\phi} = B\left(1 + \sum_{n=1}^{\infty} 2p_n(p_{Ti}y_i; p_{Tj}, y_j)\cos(n\Delta\phi)\right) \tag{3.14}$$

where B denotes the integrated inclusive pair yield and the Fourier coefficients $p_n =< \cos(n\Delta\phi) >$ for pure collective flow are given by

$$p_n(p_{Ti}y_i; p_{Tj}, y_j) = v_n(p_{Ti}, y_i)v_n(p_{Tj}, y_j) \tag{3.15}$$

Here v_n is the nth harmonic flow. However, due to the constraint of trigger particle azimuthal direction within a limited zone which has the shape like a bi-sector R (see Figure 3.6), the v_n is not the pure flow that described by inclusive integral of all interested particles in the full ϕ-space anymore, we need to introduce conditional two-particle correlations in the transverse plane.

The nth harmonic of the pair distribution, before given by Equation 3.15, is now expressed as

$$p_n^R(p_{Ti}y_i; p_{Tj}, y_j) = v_n(p_{Ti}, y_i)v_n^R(p_{Tj}, y_j) \tag{3.16}$$

Here, $v_n^R = \langle\cos[n(\phi - \Psi)]\rangle^R$ is the nth harmonic coefficient of the single-particle distribution of Equation 3.2, although the average over the azimuthal angle of the trigger particle is taken over the restricted region R that trigger particles are selected in only.

According to the calculation of paper [Bie04] in which the finite event plane resolution are also taken into account, v_n^R can be finally written as

$$\begin{aligned} v_n^R &= \frac{v_n + \delta_{n,even}\cos(n\phi_s)\frac{\sin(nc)}{nc}\langle\cos(n\Delta\Psi)\rangle + \sum_{k=2,4,6,\ldots}(v_{k+n} + v_{|k-n|})\cos(k\phi_s)\frac{\sin(kc)}{kc}\langle\cos(k\Delta\Psi)\rangle}{1 + \sum_{k=2,4,6,\ldots} 2v_k\cos(k\phi_s)\frac{\sin(kc)}{kc}\langle\cos(k\Delta\Psi)\rangle} \\ &= \frac{v_n + \delta_{n,even}\cos(n\phi_s)T_n + \sum_{k=2,4,6,\ldots}(v_{k+n} + v_{|k-n|})T_k}{1 + \sum_{k=2,4,6,\ldots} 2v_kT_k} \end{aligned} \tag{3.17}$$

where $\langle\cos(n\Delta\Psi)\rangle$ is related to the event plane azimuthal angle resolution with respect to the n-*th* harmonic, $T_k = \cos(k\phi_s)\frac{\sin(kc)}{kc}\langle\cos(k\Delta\Psi)\rangle$ is a short-hand notation, c is

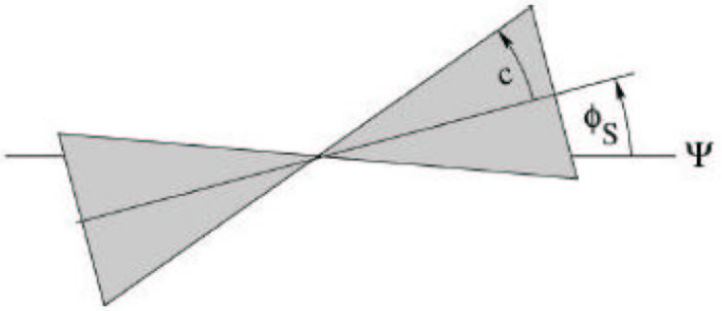

Figure 3.6: The sketch of the region R which has the same shape as the slices that the trigger particles are selected in. The region R is made up of a bisector of half-angle c that intersects the reaction plane Ψ at angle ϕ_s.

the half angle of the bi-sector, ϕ_s is the angle between the bi-sector R and the reaction plane and $\delta_{n,even} = 1$ for n even, $\delta_{n,even} = 0$ for n odd respectively.

Bringing Equation 3.17 into Equation 3.14, we get the final background estimation expression as,

$$\frac{dN^{pairs}}{\pi d\Delta\phi} = B\left(1 + \sum_{n=1}^{\infty} 2v_n^{assoc} \frac{v_n^{trig} + \delta_{n,even}\cos(n\phi_s)T_n + \sum_{k=2,4,6,\ldots}(v_{k+n}^{trig} + v_{|k-n|}^{trig})T_k}{1 + \sum_{k=2,4,6,\ldots} 2v_k^{trig}T_k}\cos(n\Delta\phi)\right) \tag{3.18}$$

This expression makes the estimation of flow background possible from the experimental observation of anisotropic flow v_n and event plane resolutions which is included in term T_k.

In case of elliptic flow ($n = 2$), neglecting higher harmonic terms with $n \geq 4$, we have

$$\begin{aligned} v_2^R &= \frac{v_2 + \cos(2\phi_s)\frac{\sin(2c)}{2c}\langle\cos(2\Delta\Psi)\rangle + v_2\cos(4\phi_s)\frac{\sin(4c)}{4c}\langle\cos(4\Delta\Psi)\rangle}{1 + 2v_2\cos(2\phi_s\frac{\sin(2c)}{2c}\langle\cos(2\Delta\Psi)\rangle} \\ &= \frac{T_2 + (1+T_4)v_2}{1 + 2T_2v_2} \end{aligned} \tag{3.19}$$

and the elliptic flow background contribution

$$\frac{dN^{pairs}}{\pi d\Delta\phi} = B\left(1 + 2v_2v_2^R\cos(2\Delta\phi)\right) = B\left(1 + 2v_2^{assoc}\frac{T_2 + (1+T_4)v_2^{trig}}{1 + 2T_2v_2^{trig}}\cos(2\Delta\phi)\right) \tag{3.20}$$

3.6.2 Contribution From v_4

In section 3.6.1, we have discussed the flow background estimation and at the end of the section given a relatively simple expression by only considering the contribution from elliptic flow. This consideration is widely used in previous di-hadron correlation study. In this section, we are going to investigate the contribution from higher harmonic flow v_4 and for the first time point out that in the di-hadron correlation with respect to reaction plane, such higher harmonic flow contribution can not be neglected.

Firstly, let's begin with writing down the expression of flow background contribution including v_2 and v_4,

$$\frac{dN^{pairs}}{\pi d\Delta\phi} = B\left(1 + 2v_2v_2^R\cos(2\Delta\phi) + 2v_4v_4^R\cos(4\Delta\phi)\right) \tag{3.21}$$

Here v_2 and v_4 are associated particle anisotropic flow, and v_2^R and v_4^R are for trigger particles.

We have been using the first term so far, up to v_2 (see Equation 3.19).

We should really consider v_4 contribution. We can supply people with following figures: the magnitude of v_2 is about 0.1, $v_4 \sim v_2^2 \sim 0.01$ and our $\frac{signal}{background}$ ratio is about $\frac{1}{100}$. It can be negligible for reaction plane integrated correction because in this case $v_n^R = v_n$ and the contribution from v_4 is $v_4 \times v_4 \sim 0.0001$, about $\times 100$ smaller than the leading effect $v_2 \times v_2$. However, for reaction plane dependent correlation, $v_n^R \neq v_n$, it is expressed by Equation 3.17, So the terms that v_4 is included are v_4, $v_2 \times v_4$ and $v_4 \times v_4$. We need to keep up to terms of $v_2 \times v_4$ since $v_2 \times v_4 \sim 0.001$ is about 10% of the signal. The terms $v_4 \times v_4$ are too small and may be neglected. According to this estimation, let's keep terms up to v_4 for v_2^R and terms up to v_2 for v_4^R, then we have:

$$v_2^R = \frac{T_2 + (1+T_4)v_2^{trig} + (T_2+T_6)v_4^{trig}}{1 + 2T_2v_2^{trig} + 2T_4v_4^{trig}} \tag{3.22}$$

and

$$v_4^R = \frac{T_4 + (T_2+T_6)v_2^{trig} + (1+T_8)v_4^{trig}}{1 + 2T_2v_2^{trig} + 2T_4v_4^{trig}} \simeq \frac{T_4 + (T_2+T_6)v_2^{trig}}{1 + 2T_2v_2^{trig}} \tag{3.23}$$

In summary, by taking v_4 contribution into account, the final flow correction of dihadron correlation with respect to reaction plane in this analysis is:

$$\begin{aligned}\frac{dN^{pairs}}{\pi d\Delta\phi} &= B\left(1+2v_2v_2^R\cos(2\Delta\phi)+2v_4v_4^R\cos(4\Delta\phi)\right)\\ &= B\left[1+2v_2^{assoc}\frac{T_2+(1+T_4)v_2^{trig}+(T_2+T_6)v_4^{trig}}{1+2T_2v_2^{trig}+2T_4v_4^{trig}}\cos(2\Delta\phi)\right.\\ &\left.+2v_4^{assoc}\frac{T_4+(T_2+T_6)v_2^{trig}}{1+2T_2v_2^{trig}}\cos(4\Delta\phi)\right]\end{aligned} \tag{3.24}$$

.

In the case of 6 slices, we have $c = 15°$, and ϕ_s for slice 1, 2, ..., 6 are equal to 7.5°, 22.5°, 37.5°, 52.5°, 67.5° and 82.5° respectively. Bringing them into Equation 3.24, we can get the flow correction for each slice.

3.7 Systematic Uncertainties

One of the most difficult things in this analysis is the estimation of systematic uncertainties. The major systematic uncertainties come from the background subtraction since the signal is sitting on a very large background and a little bias on the background estimation will affect the jet signal. For example, for the v_2 measurement, we have so far the values from event plane method, 2-particle cumulant method and 4-particle cumulant method, which one should be used? Hence, the determination of background is very critical in the analysis. We need to give the systematic errors by fully considering everything.

The flow background, as given by Equation 3.24, has three important ingredients: The event plane resolutions ($\langle\cos(2\Delta\Psi)\rangle$, $\langle\cos(4\Delta\Psi)\rangle$ and $\langle\cos(6\Delta\Psi)\rangle$), the anisotropic flow measurements v_2 and v_4, and the background magnitude B. In this section, we discuss the uncertainties from them one by one.

3.7.1 Uncertainties from Resolutions

The event plane resolutions in the analysis, $\langle\cos(k\Delta\Psi)\rangle(k = 2, 4, 6)$, are obtained from the randomly dividing sub-event method which we have talked before: The event is randomly divided into two sub-events with equal multiplicities. The two sub-events are analyzed to yield event plane angles which, ideally, should be identical. The difference between the obtained event plane angles, $\Delta\Psi$, gives the accuracy of the event plane determination. Since only the trigger events (events with at least one trigger particle) enter into our correlation measurements, the event plane resolution are measured using trigger events only.

People would naively expect that the event plane resolution should be calculated for each slice respectively (calculated from the events in which the trigger particle orientation is fixed in some slice with respect to event plane) because it would be different for different trigger particle orientations from the reaction plane due to the influence of di-jets on the event plane determination: a di-jet aligned with the reaction plane enhances the event plane construction resulting in a better resolution, whereas a di-jet perpendicular to the reaction plane reduces the accuracy of the constructed event plane resulting in a poorer resolution. However, this is a poster effect due to the selection of the trigger particle angle from the reaction plane. The resolutions used in the flow background determination, on the other hand, should be those of all trigger events before any selection of the trigger particle orientation is made.

method	$\langle\cos(2\Delta\Psi)\rangle$	$\langle\cos(4\Delta\Psi)\rangle$	$\langle\cos(6\Delta\Psi)\rangle$
randomly	0.698	0.354	0.146
charge-sign	0.680	0.332	0.124
uncertainty	2.6%	6.2%	15%

Table 3.4: Event plane resolution uncertainties and event plane resolutions for inclusive events from randomly-dividing method and charge-sign dependent method in Au + Au 20-60% collisions.

The systematic uncertainties on the event plane resolutions are estimated by comparing to the resolutions obtained by charge-sign dependent sub-event method instead of randomly dividing sub-event method. They are assessed by comparing the event resolution from trigger events only (default) and inclusive events. Table 3.4 shows the resolution values from two methods for $3 < p_T^{trig} < 4$ GeV/c and $2 < p_T^{assoc} < 3$ GeV/c. The thus estimated resolution uncertainties are 2.6% on $\langle\cos(2\Delta\Psi)\rangle$, 6.2% on $\langle\cos(4\Delta\Psi)\rangle$ and 15.1% on $\langle\cos(6\Delta\Psi)\rangle$ respectively. According to these numbers, the uncertainty from $\langle\cos(2\Delta\Psi)\rangle$ is small compared to that from v_2. Although the uncertainties from $\langle\cos(4\Delta\Psi)\rangle$ and $\langle\cos(6\Delta\Psi)\rangle$ is bigger, the contribution from these items to background is small due to the higher harmonics. So in our results we ignore the uncertainties from the resolutions.

3.7.2 Uncertainties from Flow

As discussed previously, there are several methods to measure flow. Here we want to mention two of them: One is so called Modified Event Plane Method, the other is the 4-particle Cumulant Method. The reaction plane method over predicts the v_2 due to contributions from non-flow effects (such as jets). Although the modified event plane method excludes particles within $\Delta\eta < 0.5$ to reduce the non-flow contribution from jets, it still includes some non-flow effect. The 4-particle cumulant method [PV98] is able to suppress the additional contributions from non-flow effect but under predicts the v_2 signal in the presence of v_2 fluctuations.

However, the background particles we need to subtract are all particles in the event except those correlated with the trigger particle. The anisotropy of the background is that of all background particles, including the underlying hydrodynamic type soft component and particles related to jets other than the one selected by the trigger particle. The anisotropy we need to use for the background is, therefore, not the one from hydrodynamic flow, but the one which includes partial non-flow effect due to the present background jets. In the lack of better measurement, we use the average v_2 which is the

average value between the elliptic flow from the modified reaction plane method which includes non-flow effect and that from the 4-particle cumulant method which includes minimal non-flow effect.

We compute the modified reaction plane elliptic flow, $v_2\{MRP\}$, for selected centrality and given p_T bin, using inclusive events (minimum bias events within the given centrality bin). The $v_2\{MRP\}$ from trigger events (with at least one trigger particle) only is well within the systematic uncertainty. We do not measure the 4-particle elliptic flow, $v_2\{4\}$ directly. We deduce $v_2\{4\}$ using the p_T-independent ratio of the previously measured $v_2\{MRP\}$ and $v_2\{4\}$ as a function of centrality. We then use the average v_2 as the default v_2 for our flow correction, and the range between $v_2\{MRP\}$ and $v_2\{4\}$ as systematic uncertainty due to elliptic flow. Below is the method how we get the p_T-independent ratio of $v_2\{MRP\}$ and $v_2\{4\}$.

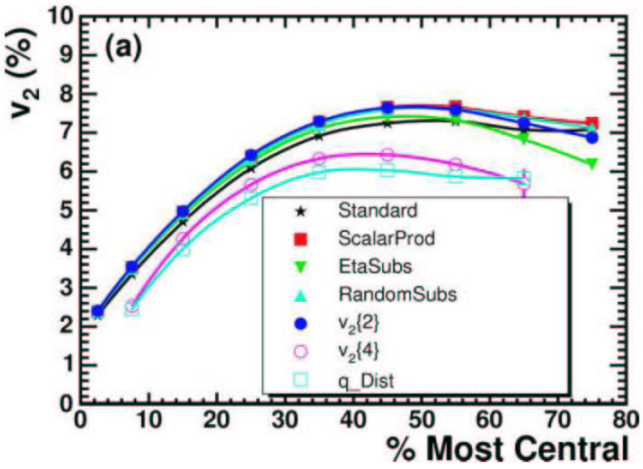

Figure 3.7: Comparison of v_2 values using different flow measurement techniques as function of centrality. "Standard" signifies the reaction plane method results and '$v_2\{4\}$ signifies the 4-particle cumulant results. Flow measurements are from Au + Au collisions at $\sqrt{s_{NN}} = 200$ GeV. Plots are from reference [Ada05c].

Figure 3.7 compares the v_2 values for the reaction plane and 4-particle cumulant methods as a function of centrality (along with the values from some other methods).

Since there are no 4 particle cumulant v_2 measurements for the top 5% and 70-80% we assume $v_2\{4\} = v_2\{MRP\}/2$ for these two centralities. This is a very conservative estimate to account for any systematic uncertainties associated with extrapolation. The ratio $v_2\{4\}/v_2\{MRP\}$ is plotted in figure 3.8 for the measured and estimated values. A second order polynomial is used to fit the ratio. This ratio is p_T independent and as function of centrality. Using this ratio, we deduce the $v_2\{4\}$ values from measured $v_2\{MRP\}$.

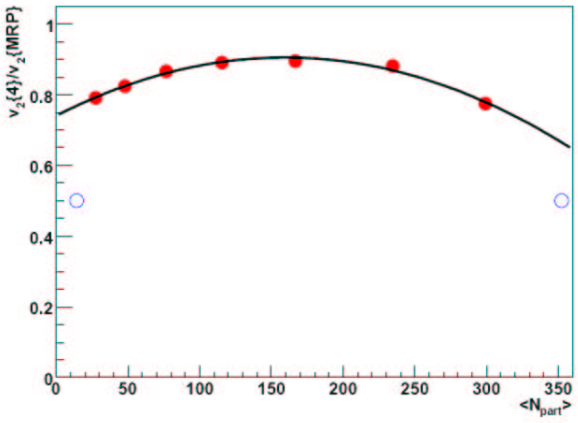

Figure 3.8: Ratio of 4-particle cumulant v_2 and reaction plane v_2. Solid points are measured. The line is a fit to a second order polynomial. The open points are a conservative estimate of the ratio for the centrality bins without 4-particle cumulant v_2 measurement. Elliptic flow values are from [Ada05c]. Plot is from [Ule07].

Besides v_2, we also use the fourth order harmonics in the background estimation. We parameterized v_4 measurement [Ada05c] within the measured p_T range of 1-3 GeV/c as $v_4 = 1.15v_2^2$ and used the parameterization for v_4 for both trigger and associated particles in our flow correction. Figure 3.9 shows the measured v_4/v_2^2. We fit the measurement of v_4/v_2^2 to a constant in the p_T range of $1 < p_T < 3$ GeV/c, yielding $v_4 = 1.15v_2^2$. The uncertainty on v_2 are propagated to v_4. Additional uncertainty of $\pm 20\%$ is applied on the trigger particle v_4 due to the extrapolation of the parameterized v_4 into the unmeasured trigger p_T region. The v_2 uncertainty due to non-flow has the largest effect

on the systematic uncertainties of the final correlation results.

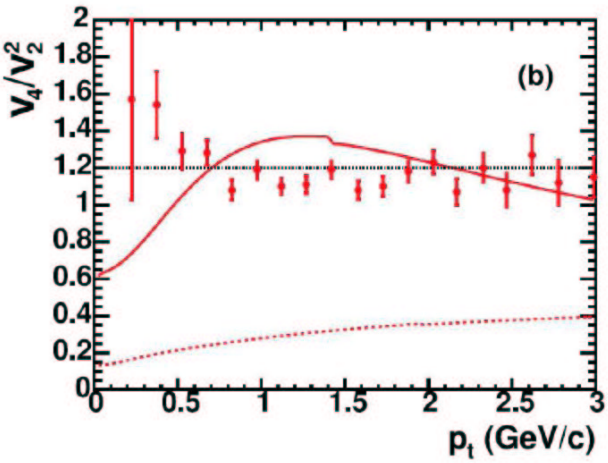

Figure 3.9: Results of v_4/v_2^2. A fit to a constant in the p_T range of $1 < p_T < 3$ GeV/c is used to parameterize v_4 in terms of v_2^2. The black line shows a fit to constant over the entire p_T range. The red curves are from blast wave fits. The plot is from [Ule07]

3.7.3 Uncertainties from Normalization Parameter B

In $p + p$ and $d +$ Au collisions at RHIC, the two-particle (di-hadron) correlation function is well described by attributing all correlations to jets/di-jets and assuming an uncorrelated(i.e. isotropic) underlying event [Rak04]. It can be described by,

$$C(\Delta\phi) = B + J(\Delta\phi) \tag{3.25}$$

where $C(\Delta\phi)$ is the raw di-hadron correlation function. $J(\Delta\phi)$ is the component of the correlation function which is due to (di)jet correlations and B is the background level of the underlying event.

However, in heavy ion collisions at RHIC, pressure gradients build up the anisotropy of the final particles which are described by anisotropic flow. Indeed, the two-particle correlation function in Au + Au collisions at RHIC can be fully described by two sources

of azimuthal correlations: (di)jet correlation $J(\Delta\phi)$ (the signal) and a harmonically modulated underlying event, due to v_2 and v_4 background (see Equation 3.24),

$$C(\Delta\phi) = B\left(1 + 2v_2v_2^R\cos(2\Delta\phi) + 2v_4v_4^R\cos(4\Delta\phi)\right) + J(\Delta\phi) \tag{3.26}$$

From Equation 3.26, It's easy to see that the jet signal $J(\Delta\phi)$ can be extracted by taking the difference between the correlation function $C(\Delta\phi)$ and the flow background,

$$J(\Delta\phi) = C(\Delta\phi) - B\left(1 + 2v_2v_2^R\cos(2\Delta\phi) + 2v_4v_4^R\cos(4\Delta\phi)\right) \tag{3.27}$$

It requires robust knowledge of flow which has been talked before and the normalization parameter B. Usually the value of B is fixed by two methods. One is the "ZYAM"(Zero Yield at Minimum) approach. It requires that the value of jet-function is zero at the minimum $\Delta\phi_{min}$.

$$J(\Delta\phi_{min}) = 0. \tag{3.28}$$

The advantage of "ZYAM" method is that no functional form for $J(\Delta\phi)$ need to be assumed and no assumption of the minimum jet signal position. The shortage is related to the statistical fluctuations due to the determination of $\Delta\phi_{min}$ with only one data point.

The other method called "Fitting" method overcomes this shortage, it is assuming that the jet signal is zero at the range around $\Delta\phi = 1$ and one may choose a reliable $\Delta\phi$ range around 1 as a fitting range that the flow background is used to fit the raw signal($C(\Delta\phi)$). In the fitting range, several data points are selected and thus reduces the fluctuation. However, it is assuming the minimum jet signal position in prior. Carefully considering these two methods, we introduce a new method to determine the normalization factor B.

Firstly, we define a new function $Y(\Delta\phi)$,

$$\begin{aligned} Y(\Delta\phi) &= \frac{C(\Delta\phi)}{1 + 2v_2v_2^R\cos(2\Delta\phi) + 2v_4v_4^R\cos(4\Delta\phi)} \\ &= B + \frac{J(\Delta\phi)}{1 + 2v_2v_2^R\cos(2\Delta\phi) + 2v_4v_4^R\cos(4\Delta\phi)} \end{aligned} \tag{3.29}$$

Again assuming at some range around $\Delta\phi_{min}$ jet yield is zero. Then try to find out the position of $\Delta\phi_{min}$. We scan the whole $\Delta\phi$ region, calculate the sum of a few(k) data points($\sum_{i=1,2,3...}^{i+k}(Y(\Delta\phi_i))$) and pick out where the sum is minimum. Thus we can get a range which includes $\Delta\phi_{min}$. Using fitting method in this $\Delta\phi$ range (including k data points) and get factor B. What's different here is that instead of using one data point as that uses in "ZYAM", k data points are used which reduces the fluctuation. And instead of fixing the the position $\Delta\phi_{min} = 1$ as in "Fitting" method, we find out the position by scanning the whole $\Delta\phi$ region which is more natural. In this analysis, we use 4(k=4, total 48 bins) data points to do the scan program and get the value of B.

Naively one would expect the background level B to be the same for all slices because the underlying background should not depend on the signal (or orientation of the trigger particle). However, due to the possible difference in jet-correlated multiplicities at different azimuthal angles and the overall constrains of centrality cuts on total reference multiplicity, there could be biases in the event samples with trigger particles at different angles, which would contain slightly different underlying background multiplicities. Thus, in our analysis we use different B values for different slices that obtained from the new method of the corresponding slice.

To measure the uncertainty from normalization parameter B, We change the number of data points (vary the size of the normalization $\Delta\phi$ range) used for scanning from 4 to 2 and 6 data points (totally we have 48 bins) respectively and the difference between them gives the systematic uncertaities from B.

All above methods make an assumption that the jet signal is zero at some $\Delta\phi$. This assumption is known as an upper limit on the background since the signal is positive definite. An assumption must be made because the true level of background is unknown a priori.

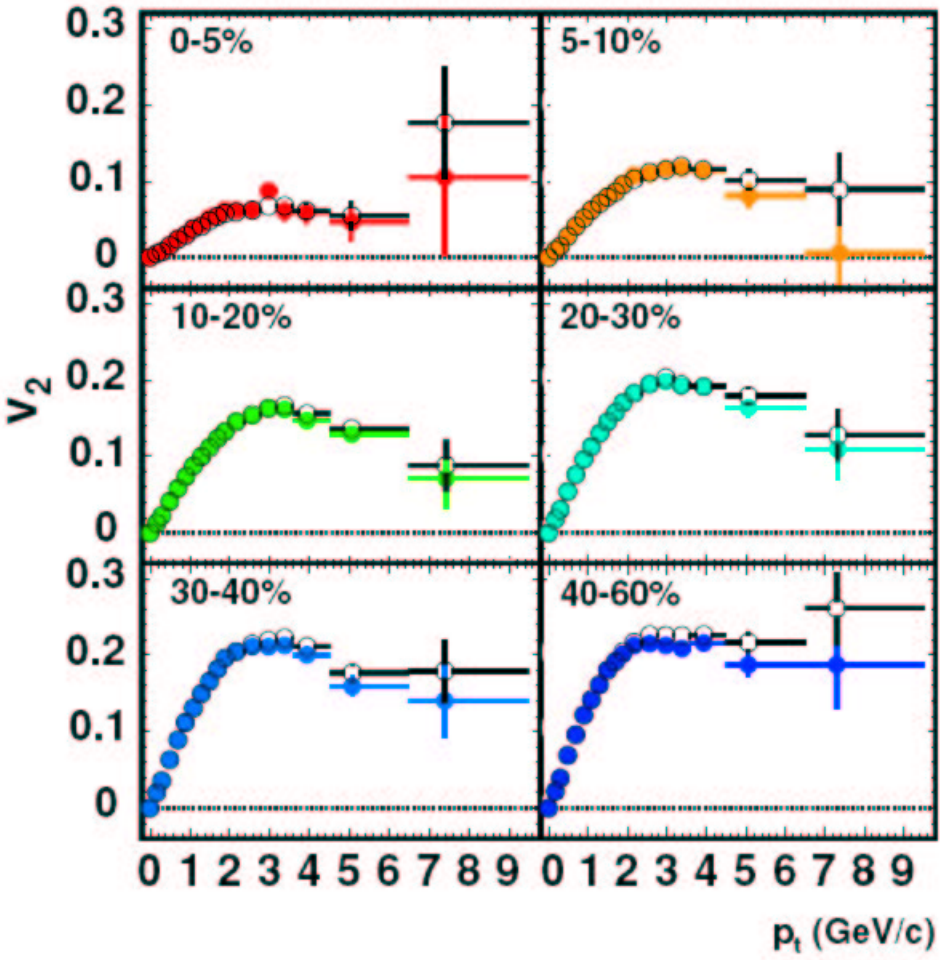

Figure 3.10: v_2 v.s. transverse momentum for charged hadrons for different centrality bins. The standard reaction plane method is shown by open symbols and the modified reaction plane method by solid symbols. Plots are from reference [Ada05c].

3.7.4 Other Uncertainties

For the results reported in this analysis, the entire $20-60\%$ Au + Au centrality range is treated as a single centrality bin in which the event plane resolutions and the elliptic flow are obtained and the azimuthal correlation is analyzed. However, the values of harmonic flow and event plane resolutions are as function of centrality. Alternatively, the analysis is repeated in each of the narrower centrality bins and the obtained correlation results are added together, weighted by the number of trigger particles in each centrality bin. The thus obtained correlation results are consistent with our default ones from a single $20-60\%$ centrality bin, which is much more smaller than the systematic uncertainties due to the flow uncertainties. This is because the measured elliptic flow v_2 are fairly constant over the entire $20-60\%$ centrality range (see Figure 3.10), so that $\langle v_2 \times v_2 \rangle \sim \langle v_2^2 \rangle$ is a very good approximation. The event plane resolutions vary with centrality by 22% from the $20-30\%$ to the $50-60\%$ centrality bin (see table 3.5) mainly due to the multiplicity change. However, the event plane resolutions enter into the flow background of Equation 3.24 linearly, and because the high p_T trigger particle multiplicity scales almost linearly with the the total multiplicity, the effect of the centrality-varying event plane resolutions is minimal in the flow correction calculated from the single $20-60\%$ centrality bin or summed from multiple narrower centrality bins.

centrality	20-30%	30-40%	40-50%	50-60%
$\langle \cos(2\Delta\Psi) \rangle$	0.74	0.721	0.662	0.573

Table 3.5: Event plane resolution measured for each centrality bins from 20-60%.

CHAPTER 4

Results

In this chapter, we present the measurements of di-hadron azimuthal correlations as a function of the trigger particle orientation relative to the event plane $\phi_s = |\phi_{trig} - \Psi_{EP}|$ and as a function of associated particle transverse momentum p_T^{assoc} in 20-60% and top 5% Au + Au collisions at $\sqrt{s_{NN}} = 200$ GeV. The trigger particle p_T range used in this analysis is $3 < p_T^{trig} < 4$ GeV/c and $4 < p_T^{trig} < 6$ GeV/c. The associate particle p_T range are $0.15 < p_T^{assoc} < 0.5$ GeV/c, $0.5 < p_T^{assoc} < 1.0$ GeV/c, $1.0 < p_T^{assoc} < 1.5$ GeV/c, $1.5 < p_T^{assoc} < 2.0$ GeV/c and $2.0 < p_T^{assoc} < 3.0(4.0)$ GeV/c respectively. We also present the values of measured v_2, event plane resolutions and normalization factor B.

4.1 Raw Signal and Flow Modulation

Figure 4.1 shows an example of the raw (not background subtracted) di-hadron correlation results with trigger particles in 6 slices of azimuthal angle relative to the event plane, $\phi_s = \phi_{trig} - \Psi_{EP}$. From left to right column, they are related to $0° < \phi_s < 15°$, $15° < \phi_s < 30°$, $30° < \phi_s < 45°$, $45° < \phi_s < 60°$, $60° < \phi_s < 75°$ and $75° < \phi_s < 90°$ respectively. The plots are for 20-60% Au + Au collisions at $\sqrt{s_{NN}} = 200$ GeV, p_T range for trigger particle is $3 < p_T^{trig} < 4$ GeV/c and for associate particles is $1.0 < p_T^{assoc} < 1.5$ GeV/c. Both the trigger and associate particles are restricted within $|\eta| < 1$. The curves are anisotropic flow modulated background. The red line is calculated with modified reaction plane $v_2\{MRP\}$, blue one is from 4-particle cumulant $v_2\{4\}$, black one is

calculated with the average v_2 which is the average of $v_2\{4\}$ and $v_2\{MRP\}$. As we mentioned, the black curves are the default flow background estimation. The red and blue curves are used as systematic uncertainties estimation. The jet signals can be achieved from the differences between the raw signal(black circles) and the flow curves.

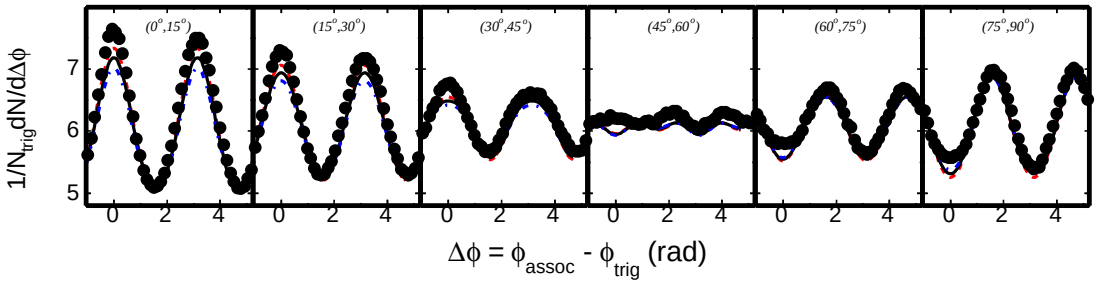

Figure 4.1: Raw di-hadron correlations with trigger particle in 6 slices of azimuthal angle relative to the event plane, $\phi_s = \phi_{trig} - \Psi_{EP}$ from left to right is corresponding to $0° < \phi_s < 15°$, $15° < \phi_s < 30°$, $30° < \phi_s < 45°$, $45° < \phi_s < 60°$, $60° < \phi_s < 75°$ and $75° < \phi_s < 90°$ respectively. The plots are from 20-60% Au + Au collisions at $\sqrt{s_{NN}} = 200$ GeV, and with $3 < p_T^{trig} < 4$ GeV/c and $1.0 < p_T^{assoc} < 1.5$ GeV/c. The curves are flow modulated background calculated with modified reaction plane $v_2\{MRP\}$(red), 4-particle $v_2\{4\}$ (blue) and the average v_2 from the two methods (black).

From this figure, we can see that the flow modulation in some slice is not exactly has the shape of $\cos(2(\Delta\phi))$ due to the contribution of v_4 terms, which gives a strong and direct evidence that v_4 terms can not be neglected.

4.2 Values for Background Estimation

In this section, we list some important measurements which are critical in the flow background estimation. These measurements are elliptic flow v_2, event plane resolutions ($\langle\cos(2\Delta\Psi)\rangle$, $\langle\cos(4\Delta\Psi)\rangle$ and $\langle\cos(6\Delta\Psi)\rangle$) as well as background normalization factor B.

Table 4.1 and table 4.2 list the default v_2 values for different p_T bins in 20-60% and top

5% Au + Au collisions respectively. Also listed are the values of event plane resolutions as function of associated p_T for trigger particle $3 < p_T^{trig} < 4$ GeV/c in 20-60% Au + Au collisions. The resolutions differ in different associated p_T bins because particles in a given associated p_T bin are excluded in the event plane reconstruction to avoid auto-correlation as aforementioned. The errors shown on the table are the systematic uncertainties.

p_T(GeV/c)	v_2±syst.	$\langle\cos(2\Delta\Psi)\rangle$	$\langle\cos(4\Delta\Psi)\rangle$	$\langle\cos(6\Delta\Psi)\rangle$
0.15-0.5	0.036±0.003	0.676	0.328	0.129
0.5-1.0	0.079±0.006	0.599	0.250	0.084
1.0-1.5	0.126±0.009	0.637	0.287	0.104
1.5-2.0	0.161±0.012	0.678	0.330	0.130
2.0-3.0	0.188±0.014	0.706	0.363	0.152
3.0-4.0	0.185±0.013	\	\	\
4.0-6.0	0.161±0.012	\	\	\

Table 4.1: Elliptic flow and event plane resolutions as a function of p_T in Au + Au 20-60% collisions. The errors are systematic uncertainties.

p_T(GeV/c)	v_2±syst.	$\langle\cos(2\Delta\Psi)\rangle$	$\langle\cos(4\Delta\Psi)\rangle$	$\langle\cos(6\Delta\Psi)\rangle$
0.15-0.5	0.0115±0.0008	0.463	0.143	0.0353
0.5-1.0	0.0259±0.0019	0.398	0.105	0.0218
1.0-1.5	0.0455±0.0031	0.426	0.121	0.0271
1.5-2.0	0.0559±0.0041	0.461	0.142	0.0348
2.0-3.0	0.0672±0.0049	0.490	0.162	0.0425
3.0-4.0	0.0657±0.0048	\	\	\
4.0-6.0	0.0510±0.0037	\	\	\

Table 4.2: Elliptic flow and event plane resolutions as a function of p_T in Au + Au top 5% collisions. The errors are systematic uncertainties.

The v_2 values and event plane resolutions for $4 < p_T^{trig} < 6$ GeV/c are not shown because they are similar to corresponding $3 < p_T^{trig} < 4$ GeV/c results since the particles used to estimate flow and reconstruct the event plane are same.

Tables 4.3 and 4.4 list the obtained background level B as a function of $\phi_{trig} - \Psi_{EP}$ and p_T^{assoc} in 20-60% Au + Au collisions for $3 < p_T^{trig} < 4$ GeV/c and $4 < p_T^{trig} < 6$ GeV/c respectively. The errors are the systematic errors.

Values of background level B for top 5% Au + Au collisions are shown in table 4.5 and 4.6. They are relative to $3 < p_T^{trig} < 4$ GeV/c and $4 < p_T^{trig} < 6$ GeV/c respectively.

4.3 Background Subtracted Results for 6 Slices

Figure 4.2 shows the background subtracted di-hadron azimuthal correlations (black circles) as a function of the trigger particle orientation relative to the event plane $\phi_s = \phi_{trig} - \Psi_{EP}$, from left to right column, it is for $0^\circ < \phi_s < 15^\circ$, $15^\circ < \phi_s < 30^\circ$, $30^\circ < \phi_s < 45^\circ$, $45^\circ < \phi_s < 60^\circ$, $60^\circ < \phi_s < 75^\circ$ and $75^\circ < \phi_s < 90^\circ$ respectively and as a function of the associated particle p_T^{assoc}, from the top down, it is related to $0.15 < p_T^{assoc} < 0.5$ GeV/c, $0.5 < p_T^{assoc} < 1.0$ GeV/c, $1.0 < p_T^{assoc} < 1.5$ GeV/c, $1.5 < p_T^{assoc} < 2.0$ GeV/c and $2.0 < p_T^{assoc} < 3.0$ GeV/c respectively. The p_T range for trigger particles is $3 < p_T^{trig} < 4$ GeV/c. The results are from 20-60% Au + Au collisions at $\sqrt{s_{NN}} = 200$ GeV. The histograms are the systematic errors due to anisotropic flows, the blue lines around zero are systematic uncertainties due to normalization factor B. The minimum bias d + Au inclusive di-hadron correlation is superimposed in red color for comparison.

Let's take a careful look at the results presented in Figure 4.2. The near-side peaks are evident for all trigger particle orientations. The shape of the near-side peak changes with ϕ_s, becoming similar to d + Au results at large ϕ_s. The previous published results have shown that the near-side correlation, while not much modified at high p_T, is modified in Au + Au collisions relative to $p + p$ and d + Au collisions at low to modest p_T. The present results indicate that the modification changes from in-plane to out-of-plane. It appears that the modification is mostly present for trigger particles oriented in-plane and modification for trigger particles oriented most out-of-plane is minimal for this centrality bin. However, we note that with the subtraction using $v_2\{MRP\}$, the modification is only modest. Unlike the near-side, the away side correlation structure evolves dramatically from in-plane to out-of-plane. The away-side is single peaked when trigger particles are oriented close to the reaction plane. Only when the trigger particle direction is far away from the reaction plane, does the double-peak structure emerge on the away side. And the away-side modification increases with increasing associated

p_T^{assoc} \ $\lvert\phi_{trig}-\Psi_{EP}\rvert$	$0-15^o$	$15-30^o$	$30-45^o$	$45-60^o$	$60-75^o$	$75-90^o$
0.15-0.5(GeV/c)	$40.175^{+0.019}_{-0.019}$	$40.157^{+0.017}_{-0.014}$	$40.129^{+0.016}_{-0.008}$	$40.048^{+0.011}_{-0.026}$	$40.035^{+0.001}_{-0.034}$	$39.999^{+0.017}_{-0.017}$
0.5-1.0(GeV/c)	$21.759^{+0.031}_{-0.022}$	$21.847^{+0.015}_{-0.011}$	$21.827^{+0.024}_{-0.017}$	$21.813^{+0.020}_{-0.028}$	$21.763^{+0.029}_{-0.006}$	$21.724^{+0.027}_{-0.012}$
1.0-1.5(GeV/c)	$6.049^{+0.010}_{-0.011}$	$6.049^{+0.010}_{-0.011}$	$6.093^{+0.012}_{-0.002}$	$6.076^{+0.020}_{-0.014}$	$6.071^{+0.010}_{-0.007}$	$6.058^{+0.011}_{-0.008}$
1.5-2.0(GeV/c)	$1.718^{+0.005}_{-0.003}$	$1.723^{+0.004}_{-0.004}$	$1.736^{+0.004}_{-0.007}$	$1.729^{+0.007}_{-0.011}$	$1.730^{+0.007}_{-0.008}$	$1.725^{+0.006}_{-0.005}$
2.0-3.0(GeV/c)	$0.6394^{+0.0026}_{-0.0025}$	$0.6444^{+0.0017}_{-0.0009}$	$0.6486^{0.0020}_{-0.0037}$	$0.6470^{+0.0031}_{-0.0012}$	$0.6452^{+0.0013}_{-0.0032}$	$0.6433^{+0.0038}_{-0.0029}$

Table 4.3: Background level B as a function of p_T^{assoc} in Au + Au 20-60% collisions. The trigger particle p_T range is $3 < p_T^{trig} < 4$ GeV/c. The errors are systematic uncertainties.

$\lvert\phi_{trig} - \Psi_{EP}\rvert$ / p_T^{assoc}	$0 - 15^o$	$15 - 30^o$	$30 - 45^o$	$45 - 60^o$	$60 - 75^o$	$75 - 90^o$
0.15-0.5(GeV/c)	$39.184^{+0.041}_{-0.045}$	$39.093^{+0.028}_{-0.062}$	$39.182^{+0.025}_{-0.046}$	$39.362^{+0.062}_{-0.08}$	$39.264^{+0.0023}_{-0.026}$	$39.216^{+0.027}_{-0.054}$
0.5-1.0(GeV/c)	$21.175^{+0.045}_{-0.036}$	$21.243^{+0.0079}_{-0.023}$	$21.319^{+0.004}_{-0.0051}$	$21.330^{+0.035}_{-0.0025}$	$21.335^{+0.047}_{-0.021}$	$21.251^{+0.039}_{-0.055}$
1.0-1.5(GeV/c)	$5.887^{+0.014}_{-0.0076}$	$5.934^{+0.015}_{-0.015}$	$5.935^{+0.011}_{-0.037}$	$5.929^{+0.024}_{-0.0032}$	$5.954^{+0.0077}_{-0.0054}$	$5.917^{+0.011}_{-0.026}$
1.5-2.0(GeV/c)	$1.679^{+0.0017}_{-0.014}$	$1.689^{+0.0025}_{-0.0052}$	$1.690^{+0.0088}_{-0.008}$	$1.680^{+0.016}_{-0.0093}$	$1.701^{+0.0003}_{-0.0033}$	$1.691^{+0.002}_{-0.011}$
2.0-4.0(GeV/c)	$0.6879^{+0.0013}_{-0.0026}$	$0.6923^{+0.0039}_{-0.0088}$	$0.6976^{0.0002}_{-0.00327}$	$0.6883^{+0.0071}_{-0.0058}$	$0.6916^{+0.0029}_{-0.0033}$	$0.6919^{+0.0045}_{-0.0054}$

Table 4.4: Background level B as a function of p_T^{assoc} in Au + Au 20-60% collisions. The trigger particle p_T range is $4 < p_T^{trig} < 6$ GeV/c. The errors are systematic uncertainties.

p_T^{assoc} \ $\lvert\phi_{trig}-\Psi_{EP}\rvert$	$0-15^o$	$15-30^o$	$30-45^o$	$45-60^o$	$60-75^o$	$75-90^o$
0.15-0.5(GeV/c)	$126.507^{+0.024}_{-0.045}$	$126.542^{+0.031}_{-0.045}$	$126.626^{+0.019}_{-0.003}$	$126.645^{+0.043}_{-0.005}$	$126.74^{+0.01}_{-0.05}$	$126.766^{+0.031}_{-0.045}$
0.5-1.0(GeV/c)	$71.945^{+0.044}_{-0.0049}$	$71.993^{+0.037}_{-0.031}$	$72.068^{+0.037}_{-0.0176}$	$72.1013^{+0.041}_{-0.0032}$	$72.150^{+0.048}_{-0.027}$	$72.165^{+0.044}_{-0.026}$
1.0-1.5(GeV/c)	$20.290^{+0.016}_{-0.012}$	$20.318^{+0.019}_{-0.019}$	$20.336^{+0.022}_{-0.012}$	$20.359^{+0.024}_{-0.0032}$	$20.354^{+0.024}_{-0.013}$	$20.365^{+0.019}_{-0.025}$
1.5-2.0(GeV/c)	$5.748^{+0.0094}_{-0.0054}$	$5.749^{+0.0096}_{-0.0047}$	$5.768^{+0.0036}_{-0.0022}$	$5.769^{+0.0081}_{-0.0049}$	$5.769^{+0.0095}_{-0.0035}$	$5.762^{+0.013}_{-0.013}$
2.0-3.0(GeV/c)	$2.032^{+0.0053}_{-0.00069}$	$2.037^{+0.0043}_{-0.0027}$	$2.041^{0.0033}_{-0.0031}$	$2.039^{+0.0051}_{-0.0024}$	$2.036^{+0.0049}_{-0.0051}$	$2.035^{+0.0019}_{-0.0002}$

Table 4.5: Background level B as a function of p_T^{assoc} in Au + Au top 5% collisions. The trigger particle p_T range is $3 < p_T^{trig} < 4$ GeV/c. The errors are systematic uncertainties.

$\lvert\phi_{trig} - \Psi_{EP}\rvert$ / p_T^{assoc}	$0 - 15^o$	$15 - 30^o$	$30 - 45^o$	$45 - 60^o$	$60 - 75^o$	$75 - 90^o$
0.15-0.5(GeV/c)	$126.297^{+0.026}_{-0.093}$	$126.345^{+0.054}_{-0.048}$	$126.429^{+0.066}_{-0.06}$	$126.551^{+0.042}_{-0.036}$	$126.609^{+0.038}_{-0.033}$	$126.587^{+0.031}_{-0.038}$
0.5-1.0(GeV/c)	$71.861^{+0.059}_{-0.11}$	$71.909^{+0.047}_{-0.0145}$	$71.968^{+0.0421}_{-0.041}$	$71.970^{+0.056}_{-0.016}$	$72.035^{+0.056}_{-0.016}$	$72.039^{+0.045}_{-0.067}$
1.0-1.5(GeV/c)	$20.255^{+0.035}_{-0.0097}$	$20.304^{+0.021}_{-0.038}$	$20.277^{+0.028}_{-0.035}$	$20.350^{+0.016}_{-0.014}$	$20.378^{+0.009}_{-0.028}$	$20.367^{+0.0066}_{-0.0085}$
1.5-2.0(GeV/c)	$5.719^{+0.016}_{-0.00048}$	$5.748^{+0.0092}_{-0.0089}$	$5.748^{+0.010}_{-0.0079}$	$5.762^{+0.0055}_{-0.0036}$	$5.763^{+0.0098}_{-0.0074}$	$5.7624^{+0.019}_{-0.014}$
2.0-4.0(GeV/c)	$2.194^{+0.0079}_{-0.0075}$	$2.204^{+0.0036}_{-0.0047}$	$2.210^{0.0038}_{-0.0038}$	$2.224^{+0.0029}_{-0.011}$	$2.210^{+0.0048}_{-0.0056}$	$2.215^{+0.0048}_{-0.0083}$

Table 4.6: Background level B as a function of p_T^{assoc} in Au + Au top 5% collisions. The trigger particle p_T range is $4 < p_T^{trig} < 6$ GeV/c. The errors are systematic uncertainties.

p_T^{assoc}. The previous results show that the away-side correlation structure is significantly modified in central Au + Au collisions, and the modification is the largest in the intermediate p_T range [Ada03]. The present result indicates that the away-side modification has a strong dependence on the trigger particle direction relative to the reaction plane. The results suggest significant difference between the medium path-lengths traversed by the away-side parton at different $\phi_s = \phi_{trig} - \Psi_{EP}$ and should provide useful input to theoretical modelling of partonic energy loss in nuclear medium.

Figure 4.3 shows the similar results in 20-60% Au + Au collisions at $\sqrt{s_{NN}} = 200$ GeV but with the higher trigger p_T range $4 < p_T^{trig} < 6$ GeV/c. In fact, the higher trigger particle p_T is selected, the more probable it is from a jet and the more well defined is the jet axis. Although it is limited by the statistics, the results and variations from trigger particles with higher p_T of $4 < p_T^{trig} < 6$ GeV/c are similar to that from $3 < p_T^{trig} < 4$ GeV/c.

The results for top 5% Au + Au collisions at $\sqrt{s_{NN}} = 200$ GeV are shown in Figure 4.4 and Figure 4.5. They are for trigger particle p_T range in $3 < p_T^{trig} < 4$ GeV/c and $4 < p_T^{trig} < 6$ GeV/c respectively. We will discuss them in next chapter.

4.4 Background Subtracted Results for 2 Slices

Besides dividing the ϕ-space into 6 slices, we also have the measurement for 2 slices situation (i.e. trigger particles are in-plane and out-of-plane).

Figure 4.6 shows the background subtracted di-hadron correlations with trigger particles in-plane (red circles) and out-of-plane (blue circles). The results are for $3.0 < p_T^{trig} < 4.0$ GeV/c (upper row) and $4.0 < p_T^{trig} < 6.0$ GeV/c (lower raw), and $1.0 < p_T^{assoc} < 1.5$ GeV/c (left column) and $2.0 < p_T^{assoc} < 3.0(4.0)$ GeV/c (right column) in 20-60% Au + Au collisions. The systematic errors due to the uncertainty of anisotropy flow are shown in histograms (solid line is the results from $v_2\{MRP\}$ and dotted line is from $v_2\{4\}$). Difference is observed between in-plane and out-of-plane for both p_T^{assoc} bins.

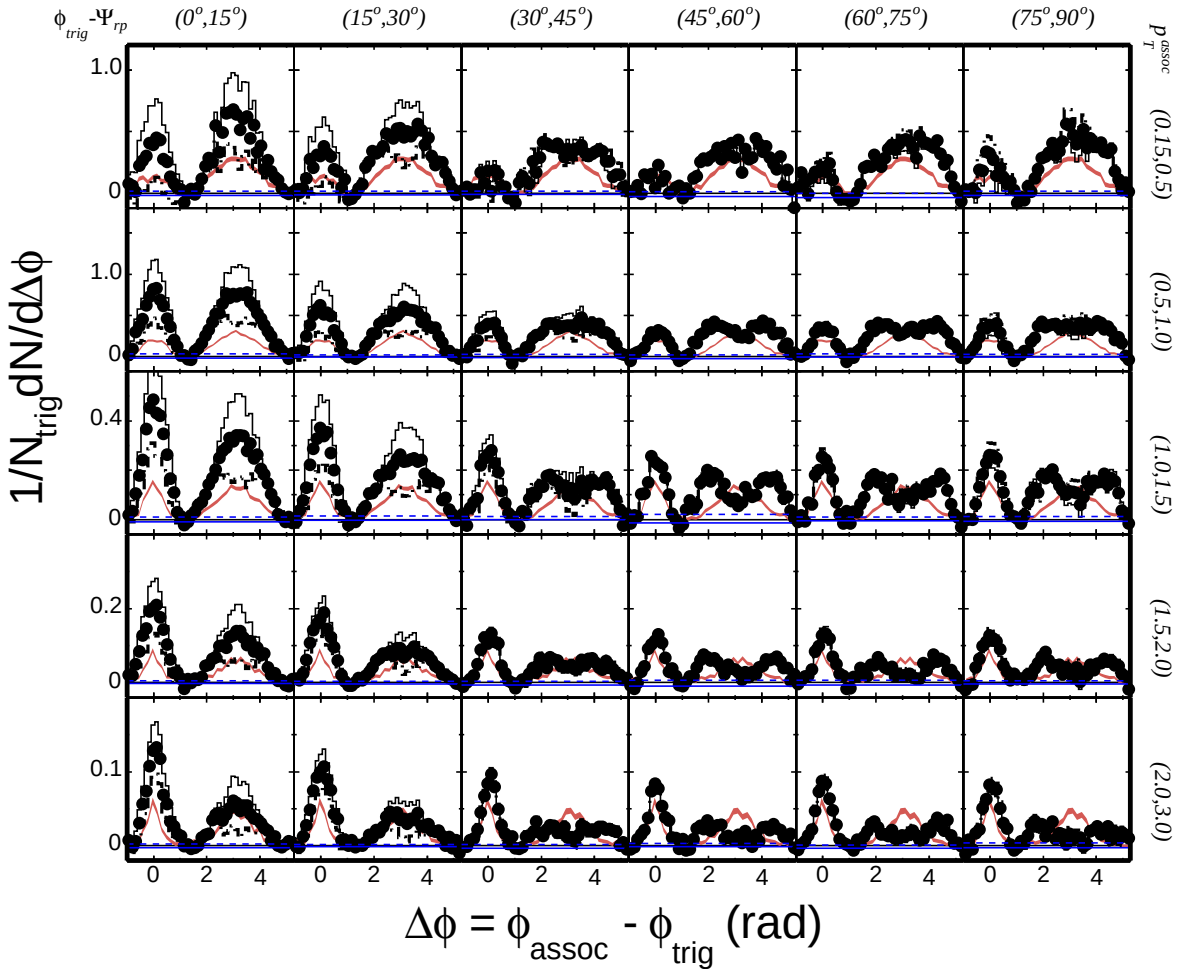

Figure 4.2: Background subtracted di-hadron correlations with trigger particle in 6 slices of azimuthal angle from the event plane, $\phi_{trig} - \Psi_{EP}$. The plots are for 20-60% Au + Au collisions at $\sqrt{s_{NN}} = 200$ GeV, $3 < p_T^{trig} < 4$ GeV/c, and five associate p_T ranges. Both the trigger and associate particles are restricted within $|\eta| < 1$. Systematic uncertainties due to flow are shown in histograms, Systematic uncertainties due to normalization factor B are shown as blue lines around zero. The inclusive di-hadron correlation from d + Au collisions is superimposed for comparison in red color, where the size of the shaded area indicates statistics errors.

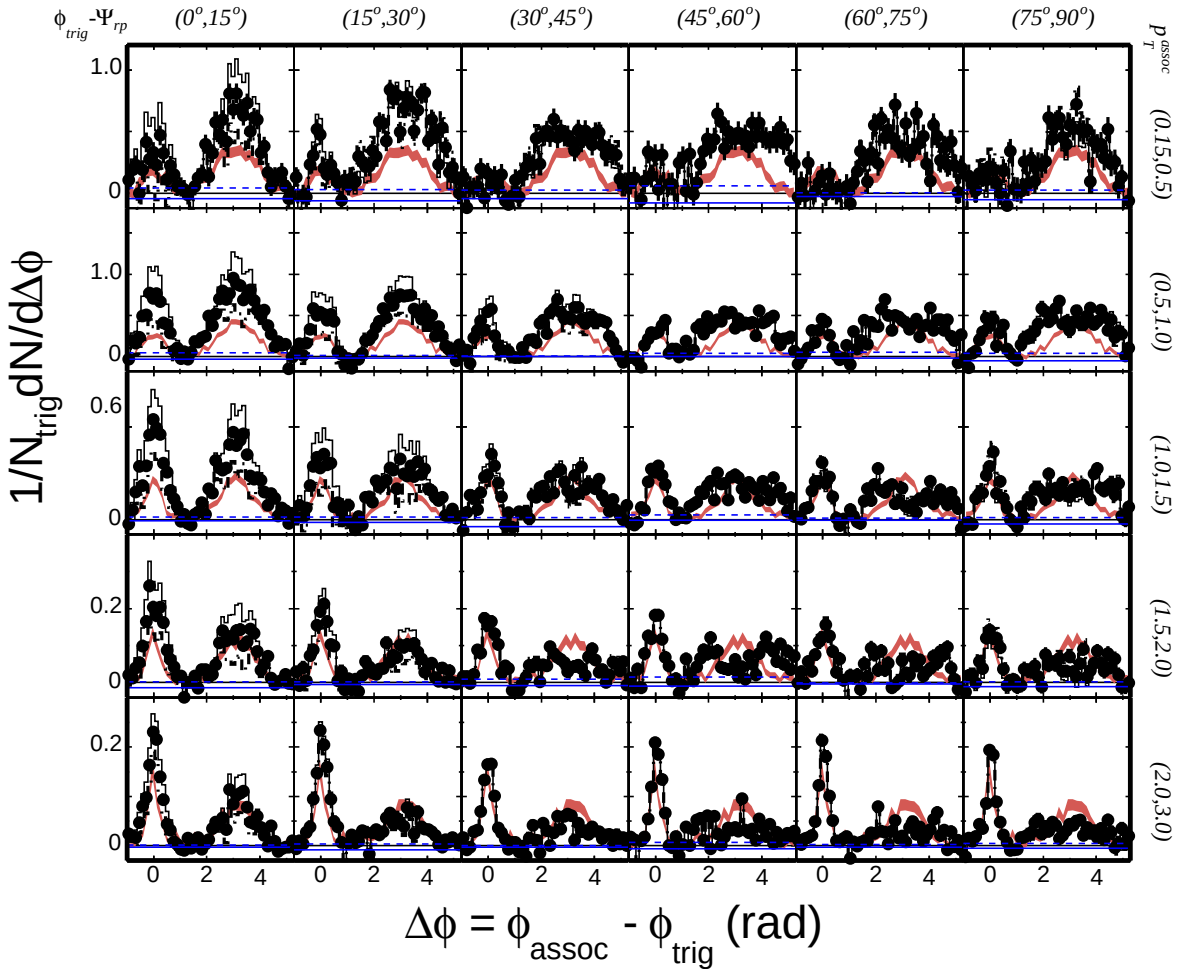

Figure 4.3: Background subtracted di-hadron correlations with trigger particle in 6 slices of azimuthal angle from the event plane, $\phi_{trig} - \Psi_{EP}$. The plots are for 20-60% Au + Au collisions at $\sqrt{s_{NN}} = 200$ GeV, $4 < p_T^{trig} < 6$ GeV/c, and five associate p_T ranges. Both the trigger and associate particles are restricted within $|\eta| < 1$. Systematic uncertainties due to flow are shown in histograms, Systematic uncertainties due to normalization factor B are shown as blue lines around zero. The inclusive di-hadron correlation from d + Au collisions is superimposed for comparison in red color, where the size of the shaded area indicates statistics errors.

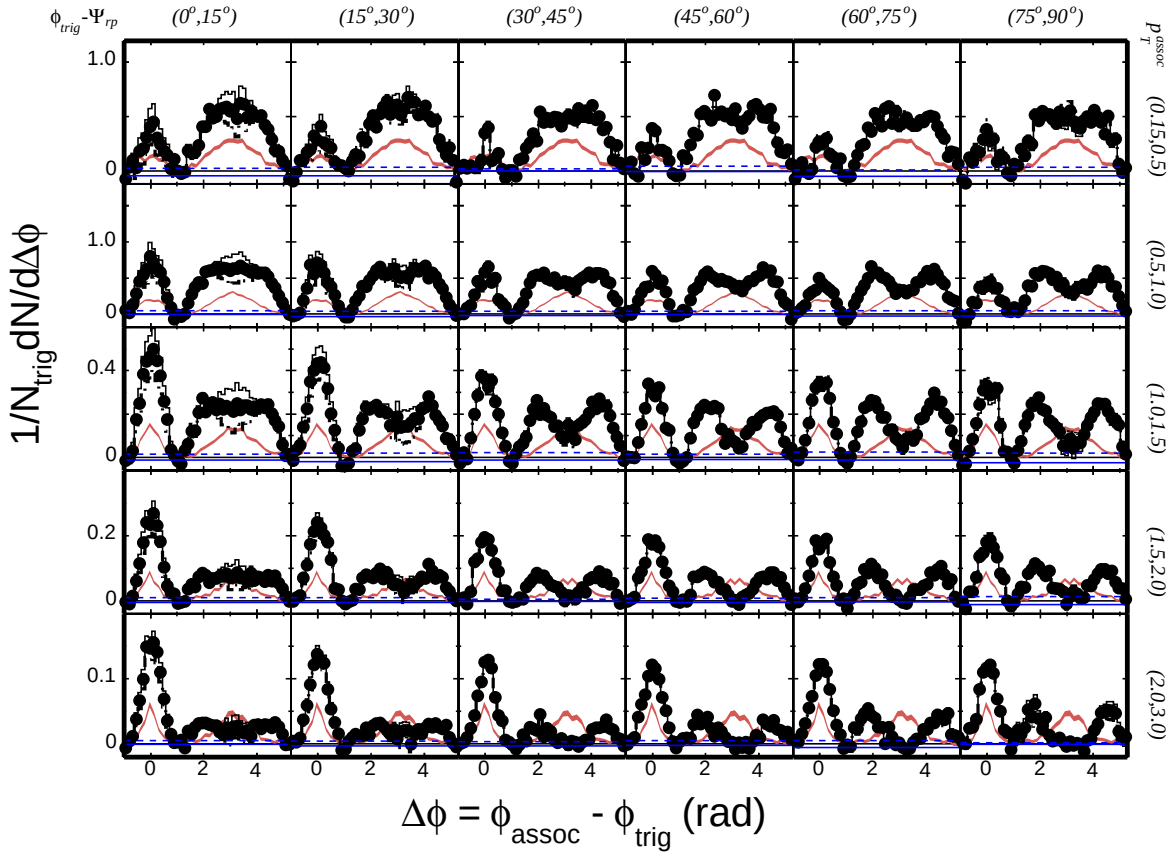

Figure 4.4: Background subtracted di-hadron correlations with trigger particle in 6 slices of azimuthal angle from the event plane, $\phi_{trig} - \Psi_{EP}$. The plots are for top 5% Au + Au collisions at $\sqrt{s_{NN}} = 200$ GeV, $3 < p_T^{trig} < 4$ GeV/c, and five associate p_T ranges. Both the trigger and associate particles are restricted within $|\eta| < 1$. Systematic uncertainties due to flow are shown in histograms, Systematic uncertainties due to normalization factor B are shown as blue lines around zero. The inclusive di-hadron correlation from d + Au collisions is superimposed for comparison in red color, where the size of the shaded area indicates statistics errors.

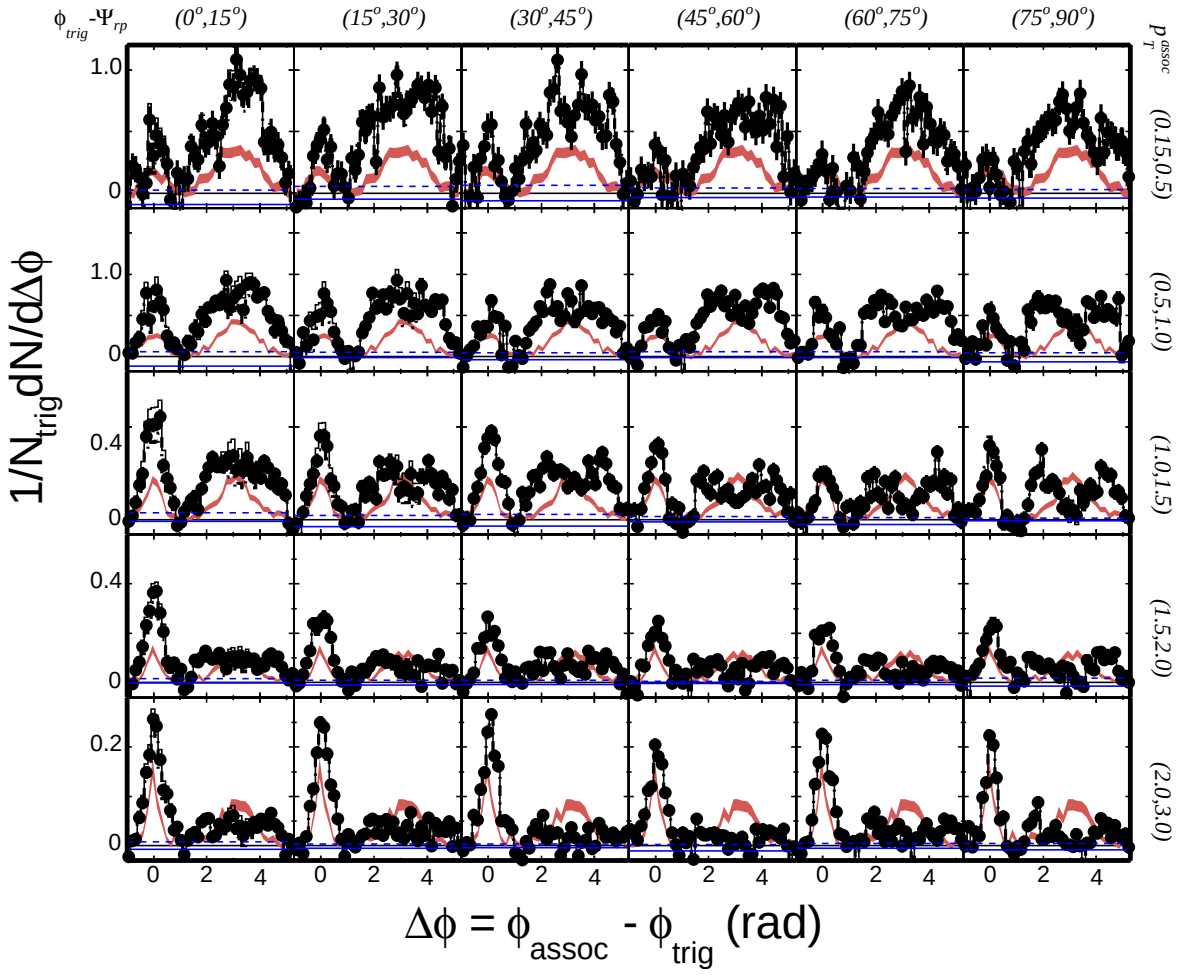

Figure 4.5: Background subtracted di-hadron correlations with trigger particle in 6 slices of azimuthal angle from the event plane, $\phi_{trig} - \Psi_{EP}$. The plots are for top 5% Au + Au collisions at $\sqrt{s_{NN}} = 200$ GeV, $4 < p_T^{trig} < 6$ GeV/c, and five associate p_T ranges. Both the trigger and associate particles are restricted within $|\eta| < 1$. Systematic uncertainties due to flow are shown in histograms, Systematic uncertainties due to normalization factor B are shown as blue lines around zero. The inclusive di-hadron correlation from d + Au collisions is superimposed for comparison in red color, where the size of the shaded area indicates statistics errors.

The difference is larger for the low p_T^{assoc} bin. The difference at high p_T^{assoc} is on the order of 1σ of systematic uncertainty. The analysis reported here(bottom right plot) differs from that published STAR results in [Ada04c] in two ways: (i) the average $v_2 = (v_2\{MRP\} + v_2\{4\})/2$ is used in this analysis while $v_2 = v_2\{MRP\}$ was used in Ref. [Ada04c], (ii) the flow correlation is corrected up to v_4 in this analysis while correction only up to v_2 was done in Ref. [Ada04c].

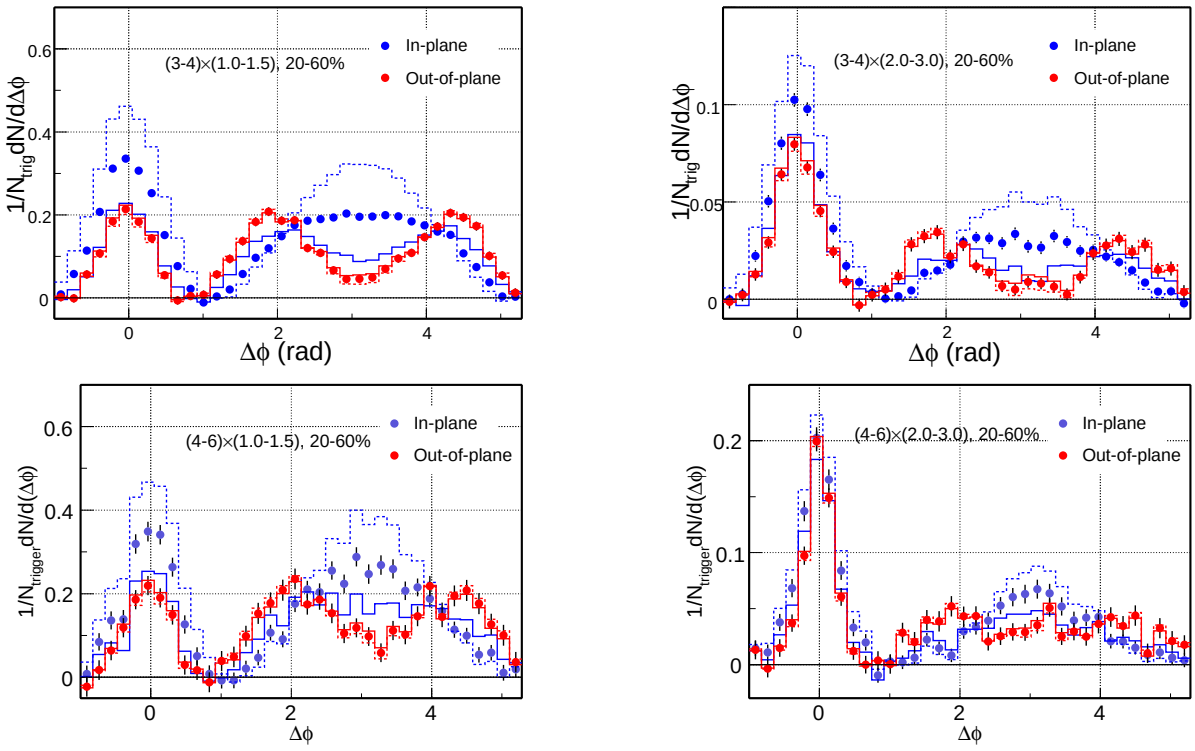

Figure 4.6: Background subtracted di-hadron correlations with trigger particles in-plane ($|\phi_{trig} - \Psi_{EP}| < \frac{\pi}{4}$, blue circles) and out-of-plane ($|\phi_{trig} - \Psi_{EP}| > \frac{\pi}{4}$, red circles). The results are for $3.0 < p_T^{trig} < 4.0$ GeV/c (upper row) and $4.0 < p_T^{trig} < 6.0$ GeV/c (lower raw), and $1.0 < p_T^{assoc} < 1.5$ GeV/c (left column) and $2.0 < p_T^{assoc} < 3.0(4.0)$ GeV/c (right column). They are from 20-60% Au + Au collisions. Both the trigger and associate particles are restricted within $|\eta| < 1$. Systematic uncertainties due to flow subtraction are shown in histograms.

CHAPTER 5

Discussions

Results presented in Chapter 4 show that both the near-side and away-side are modified and the modification depends on the trigger particle orientation relative to reaction plane. In this chapter we will discuss the modifications on near-side and away-side in more details.

5.1 Comparison Between Mid-central and Central Collisions

The away-side modifications for both $3 < p_T^{trig} < 4$ GeV/c and $4 < p_T^{trig} < 6$ GeV/c in 20-60% Au + Au collisions change from in-plane to out-of-plane and the modification becomes stronger when trigger particles move from in-plane to out-of-plane. The strong dependence on the trigger particle direction with respect to reaction plane suggests the important role the medium path-length plays in jet quenching scenario. We can further examine this results by investigating the ϕ_s dependence of the correlation function in top 5% central Au + Au collisions because if it is true, one should observe that the path-length variation with the trigger particle orientation is greatly reduced in central collisions. The results from top 5% Au + Au collisions are shown in Figure 4.4 and Figure 4.5.

To make a careful comparison, we present the results from two centrality bins with one associate p_T bin $1.0 < p_T^{assoc} < 1.5$ GeV/c in Figure 5.1 and compare them carefully.

The upper plot is from 20-60% Au + Au collisions and the lower one is from top 5% Au + Au collisions. The trigger particle p_T range is $3 < p_T^{trig} < 4$ GeV/c. The reference results from d + Au collisions is superimposed in red. In mid-central collisions, away-side structure evolves from single-peak ($\phi_s = 0°$) to double peak ($\phi_s = 90°$). However, although sizeable change is observable, the change from in-plane to out-of-plane is not dramatic in central collisions, as what we expected. The double-peak structure seems already present for trigger particles oriented in-plane(at small ϕ_s) due to the relatively larger path-length away-side parton traverse in the reaction plane direction in central collisions and for trigger particles mostly perpendicular to reaction plane(large ϕ_s) there is little difference between these two centrality bins since the path-lengths are almost same on the direction perpendicular to reaction plane between the two centrality bins. These results are consistent with the path-length effect in jet quenching scenario qualitatively.

5.2 Away-side

Evolutions from single-peak to double-peak on the away-side structure are obviously observed in 20-60% Au + Au collisions while the evolution is observed not as significant in top 5% central Au + Au collisions as that in mid-central collisions. To quantify this modification, we focus on the broadness and amplitude of the away-side respectively in this section.

5.2.1 Away-side Broadness

A variable away-side 'RMS' is defined to quantify the away-side broadness as,

$$RMS = \sqrt{\frac{(\sum_i \Delta\phi_i - \pi)^2 y_i}{\sum_i y_i}} \tag{5.1}$$

where i denotes the ith bin in the $\Delta\phi$ region. y_i is the value of correlation function for ith bin. The sum is within $|\Delta\phi - \pi| < 2\pi - 1$. RMS describes the degree of the

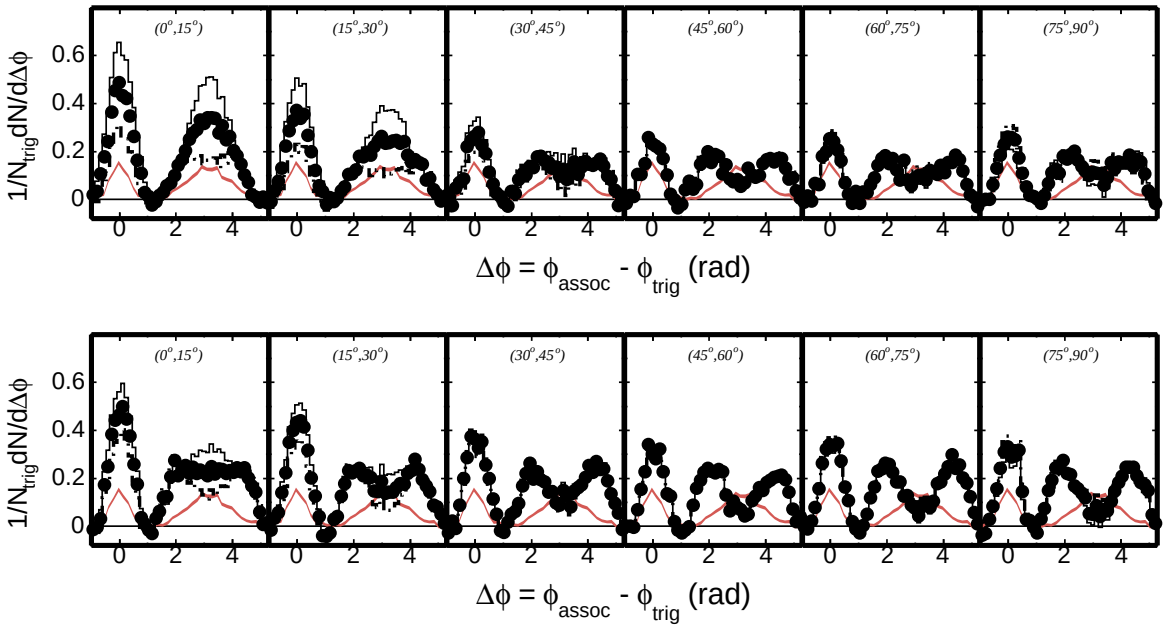

Figure 5.1: (color online) Background subtracted di-hadron correlations with trigger particle in 6 slices of azimuthal angle from the reaction plane, $\phi_s = \phi_T - \Psi_{EP}$. The plots are for 20-60% (upper one) and top 5% (lower one) Au + Au collisions, $3 < p_T^{trig} < 4$ GeV/c and $1.0 < p_T^{assoc} < 1.5$ GeV/c. Both the trigger and associate particles are restricted within $|\eta| < 1$. Systematic uncertainties due to flow subtraction are shown in histograms. The inclusive di-hadron correlation from d + Au collisions (in red) is superimposed for comparison, where the size of the shaded area indicates statistics errors.

broadness on the away-side: the bigger RMS is, the more broadness (or double-peaked) that the away-side appears, the stronger modification there is.

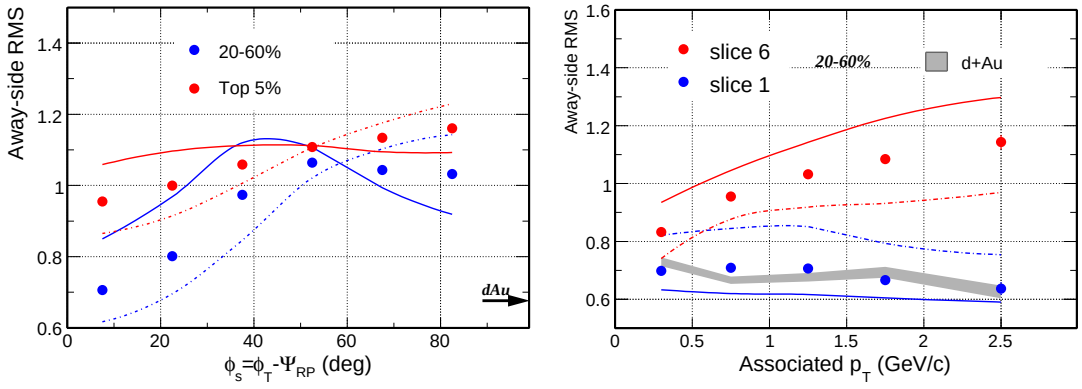

Figure 5.2: (Color online)Left: The di-hadron correlation function away-side RMS as a function of the trigger particle azimuthal angle from the event plane, ϕ_s, in 20-60% (blue) and top 5% (red) Au + Au collisions for $1.0 < p_T^{assoc} < 1.5$ GeV/c. Right: The away-side RMS for slice 1 and 6 as a function of associated p_T^{assoc} in 20-60% Au + Au collisions. The trigger p_T range is $3 < p_T^{trig} < 4$ GeV/c for both panels. The curves indicate systematic uncertainties due to flow subtraction. The corresponding d + Au results is indicated by the arrow in the left panel and by the shaded area in the right panel.

Figure 5.2 left panel shows the RMS of the away-side correlation function within $|\Delta\phi - \pi| < 2\pi - 1$ as a function of the trigger particle orientation ϕ_s for 20-60% and top 5% Au + Au collisions in blue and red circles, respectively. The p_T range for trigger and associated particles are $3 < p_T^{trig} < 4$ GeV/c and $1.0 < p_T^{assoc} < 1.5$ GeV/c. The solid and dotted lines are the systematic errors due to flow background subtraction from $v_2\{MRP\}$ and $v_2\{4\}$ respectively. The reference d + Au results are indicated by the arrow on the right. The away-side RMS increases with ϕ_s, which means the away-side distribution becomes more double-peaked as ϕ_s increases and the rate of increase is smaller in central than mid-central collisions. If we look at the RMS for slice 1 (the first data points), it is not much larger than d + Au in mid-central collisions. However, in 5% central collisions, the away-side with trigger particles in slice 1 already shows marked broadening compared to d + Au . This is consistent with the different

pathlengths in the reaction plane direction between the two centrality bins. For the RMS in slice 6 (the last data point on the plot), the results are not much different between the two centralities. This is perhaps again consistent with the collision geometry - the difference in the pathlengths perpendicular to the reaction plane between the two collision centralities is not significant.

The right panel of Figure 5.2 shows the away-side RMS as a function of the associated p_T^{assoc} for slice 1 (blue) and 6 (red) in 20-60% centrality. The corresponding d + Au result is indicated by the shaded area. The RMS remains constant for slice 1, and is not much broader than the d + Au result. The RMS for slice 6 increases with p_T^{assoc}. The double-peak structure is the strongest when the trigger particle is perpendicular to the reaction plane and the associated particle is hardest. Results for other slices vary smoothly between those shown for slice 1 and 6, and the top 5% centrality data also lie in-between.

5.2.2 Away-side Amplitude

Figure 5.3 shows the average correlation amplitude on the away-side in the center region ($|\Delta\phi-\pi| < 0.42$) and in the double-peak region ($0.78 < |\Delta\phi-\pi| < 1.65$) as a function of ϕ_s in 20-60% (left panel) and top 5% (right panel) Au + Au collisions. The amplitudes in the π region are similar between the two centrality bins, both drop with ϕ_s. The double-peak region amplitude remains constant over ϕ_s and the amplitude in top 5% is higher than that in 20-60% Au + Au collisions. The relative amplitudes between the two regions indicate the degree of the double-peak structure: For mid-central collisions, the amplitude for π region is higher than that for double-peak region at small ϕ_s and becomes lower at large ϕ_s, which means the away-side evolves from single-peak to double-peak. However, for top 5% central collisions, the amplitude of π region and double-peak region are similar at small ϕ_s, then the amplitude of π region becomes higher than that of double-peak region, which indicates that the away-side appears double-peak structure at the small ϕ_s.

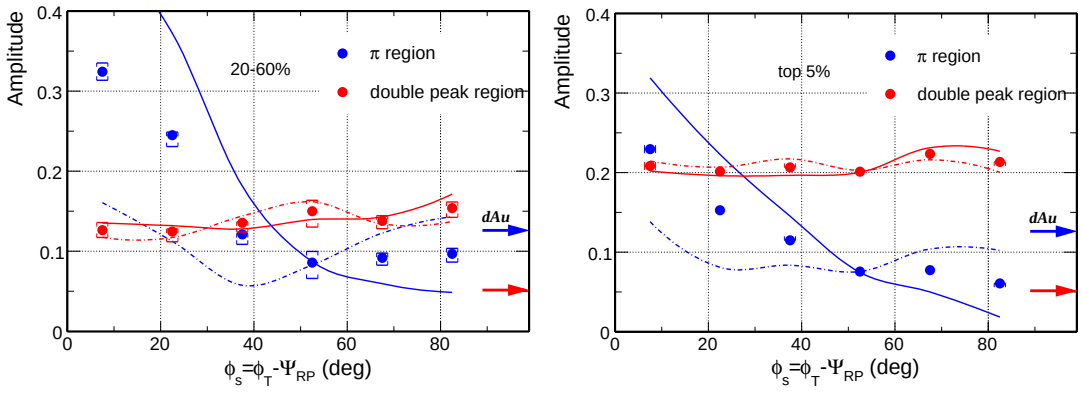

Figure 5.3: (Color online) The away-side di-hadron correlation amplitudes in π region ($|\Delta\phi - \pi| < 0.42$) and double-peak region ($0.78 < |\Delta\phi - \pi| < 1.65$) as a function of the trigger particle azimuthal angle from the event plane,ϕ_s, in 20-60% (left) and top 5% (right) Au + Au collisions. The curves and square brackets indicate systematic uncertainties due to flow subtraction from v_2 and B uncertainties, respectively.

5.3 Near-side

The near-side peak are found changes with ϕ_s. To see it clearly, Figure 5.4 plots the average amplitude of near-side correlation. It is rather counterintuitive as the near-side jet predominately emerges outward from the surface of the medium due to jet quenching. It experiences minimal amount of medium which should not vary much from in-plane to out-of-plane. Yet, the results demonstrate a significant change in the near-side peak amplitude. The near-side amplitude drops with ϕ_s. For the 20-60% centrality, the amplitude at large ϕ_s is not much different from the d + Au results, perhaps indicating minimal medium modification. On the other hand, the amplitude at small ϕ_s appears larger than d + Au suggesting significant medium modification.

In section 3.1, it has been shown in the inclusive di-hadron correlation that the near-side correlation strength is enhanced in Au + Au with respect to p + p and d + Au collisions, and the enhancement is mainly due to the large contribution from the ridge [Put07]. In order to investigate the underlying physics mechanism for the near-side structure changing with trigger particle orientation, we try to separate contributions

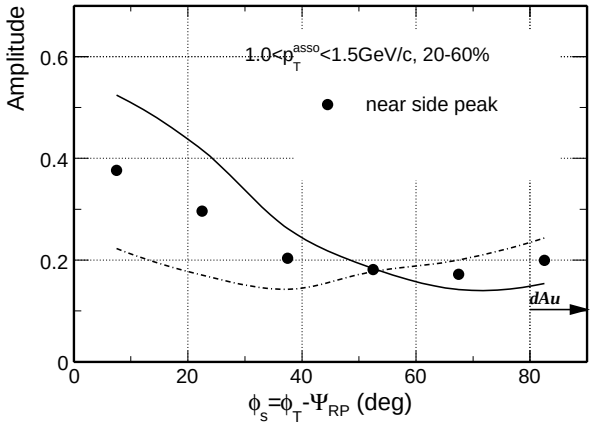

Figure 5.4: The near-side di-hadron correlation amplitudes as a function of the trigger particle azimuthal angle from the event plane in 20-60% Au + Au collisions with $3 < p_T^{trig} < 4$ GeV/c and $1.0 < p_T^{assoc} < 1.5$ GeV/c. The curves indicate systematic uncertainties due to flow subtraction from v_2.

from the ridge and the jet by analyzing the correlation data in two different $\Delta\eta$ regions: $|\Delta\eta| > 0.7$ where the ridge is the dominant contributor (two black boxes) and $|\Delta\eta| < 0.7$ where both the ridge and the jet contribute (red and pink boxes) (see Figure 5.5 for reference).

To gain the ridge part (two black boxes on figure 5.5), one can just do the flow background subtracted di-hadron correlation function from $|\Delta\eta| > 0.7$. The near-side correlation got in this way is considered to be due to ridge because the jet contribution is mostly confined within $|\Delta\eta| < 0.7$.

For the jet part (red box on the plot), one may take the difference between the raw (not background subtracted) correlations from the two $\Delta\eta$ regions after multiplying a coefficient C onto the $|\Delta\eta| > 0.7$ raw correlation, such that the resultant correlation on the away-side is zero. The coefficient may also got from the triangle $\Delta\eta$ acceptance distribution (The acceptance distribution is triangle because the single particle η distribution is flat in measured η region) by taking the acceptance ratio between $|\Delta\eta| < 0.7$ and $|\Delta\eta| > 0.7$. Such measured coefficient value is about 1.44. And the coefficient got from such two ways are almost equivalent. Here raw correlation results are used instead

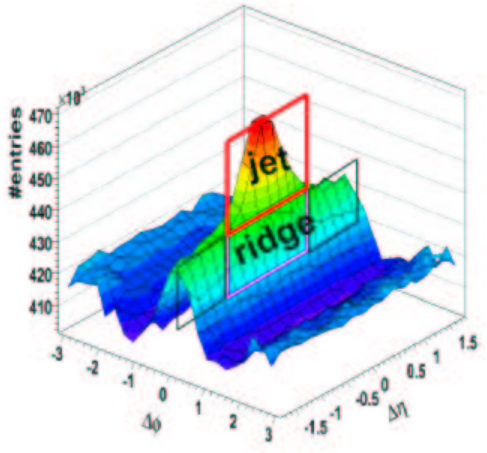

Figure 5.5: An illuminating plot for separating the jet and ridge parts on the near-side correlations.

of background subtracted correlation results because we want to avoid the uncertainties from measured flow background. Since the flow contribution is symmetric in two $\Delta\eta$ regions, it is auto-cancelled by taking the difference between the correlations in two $\Delta\eta$ regions. An assumption that the ridge is uniform in the measured $\Delta\eta$ range is made here so that the resultant difference should represent the di-hadron correlation for the jet part on the near-side above the flat ridge.

Figure 5.6 shows the di-hadron correlations for jet part and ridge part with trigger particles in each slice in 20-60% and top 5% Au + Au collisions. The upper plot is the result from 20-60% collisions. The lower plot is the top 5% collision result. For each of these plots, the top raw is the results corresponding to ridge and the bottom raw is corresponding to jet part. For each raw, the 6 mini-plots are relative with the trigger particles in slice 1, 2, ..., 6. The trigger and associated particles p_T range for both plots are $3 < p_T^{trig} < 4$ GeV/c and $1.5 < p_T^{assoc} < 2.0$ GeV/c. The ridge correlation shows a significant changes with ϕ_s. It decreases firstly and then almost saturates at larger ϕ_s. However, the jet correlation behaves differently. Small changes on the near-side from in-plane to out-of-plane in mid-central collisions and almost little changes of the near-side

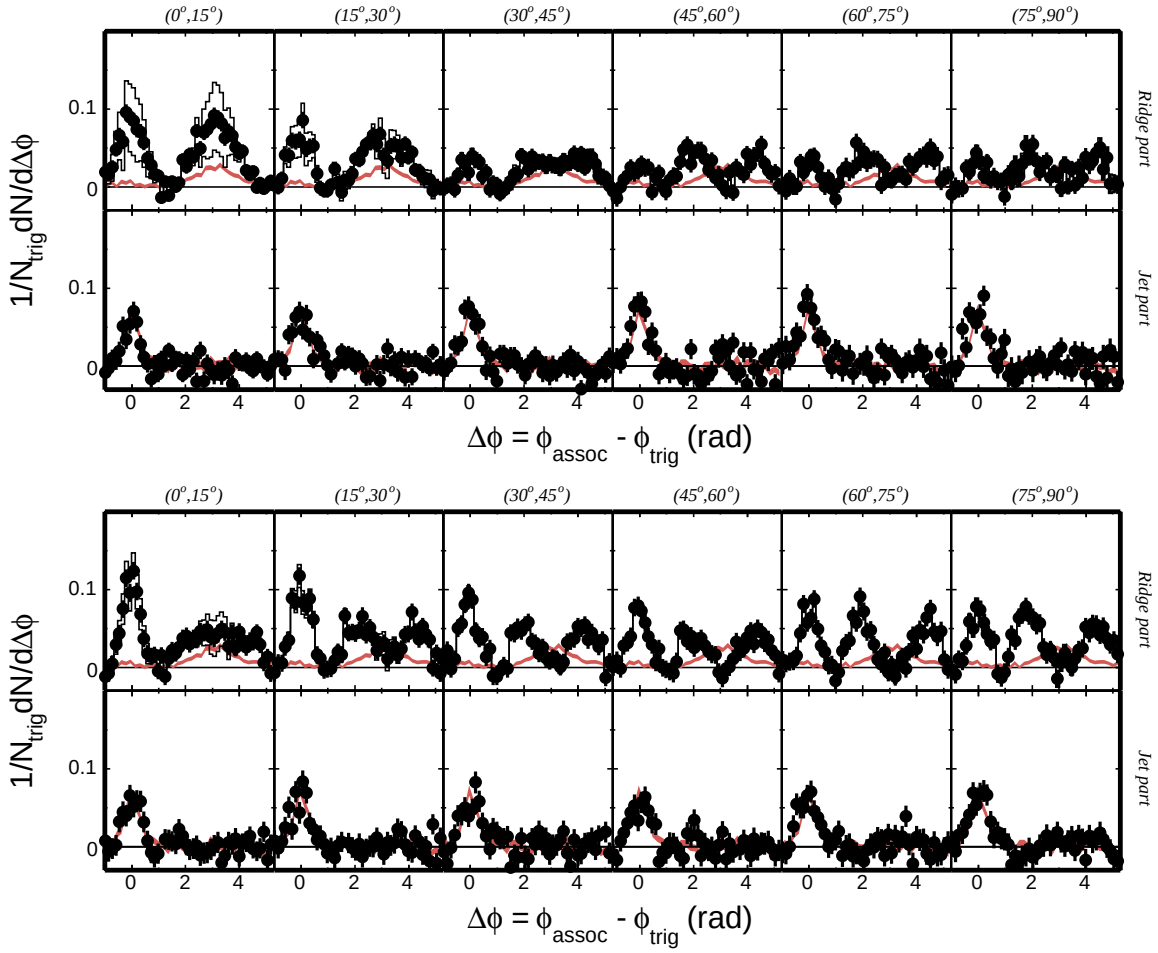

Figure 5.6: Di-hadron correlations for ridge part (Top row in each plot) and jet part (bottom row in each plot) in 20-60% (upper plot) and top 5% (lower plot) Au + Au collisions, respectively. The results are for $3 < p_T^{trig} < 4$ GeV/c and $1.5 < p_T^{assoc} < 2.0$ GeV/c. The inclusive di-hadron correlation from d + Au collisions (in red) is superimposed for comparison.

correlation with ϕ_s in top 5% central collisions.

To quantify the near-side modification, we show in Figure 5.7 the total yield on the near-side ($|\Delta\phi| < 1.0$) as a function of ϕ_s for the 'ridge' part (blue points)in the 20-60% centrality (left plot) and top 5% centrality (right plot), respectively. The systematic uncertainties from the uncertainties of v_2 and background level B on the ridge yields are indicated by the curves and square brackets, respectively. Here we only present one result as an example with the p_T ranges for trigger and associated particles are $3 < p_T^{trig} < 4$ GeV/c and $1.5 < p_T^{assoc} < 2.0$ GeV/c. The ridge yield decreases with ϕ_s. And the decrease appears to be more significant in the 20-60% centrality bin than the top 5% centrality bin.

Figure 5.7 also shows the near-side yield as a function of ϕ_s for the 'jet' part (red points) in mid-central (left plot) and central (right plot) collisions, respectively. The systematic uncertainty on the jet yield is small because the large uncertainties due to v_2 are cancelled assuming v_2 is constant over $\Delta\eta$. This should be a very good assumption because PHOBOS shows that v_2 is rather constant within the η acceptance of the STAR TPC (dropping only outwards large $|\eta|$), and moreover, even if v_2 drops with η in our measured range, the effect is mostly washed out in the difference variable $\Delta\eta$. Other sources of systematic uncertainties, however, may be present. One such source is that the ridge amplitude (after acceptance correction) may not be constant over over measured $\Delta\eta$ but drops with increasing $|\Delta\eta|$. If so, our 'jet' measurement constrains residual ridge contribution. However, we expect this to be a rather small fraction of the measured ridge yield. Nevertheless, this effect would cause the real 'jet' part to be smaller than shown in Figure 5.7 and more so at smaller ϕ_s. Another source of systematic uncertainties is that the jet peak may be wide so the $|\Delta\eta| < 0.7$ cut may not contain the whole jet part, and moreover the fraction that leaks out of the $\Delta\eta$ cut gets subtracted. Such an effect would be larger in the top 5% centrality than the 20-60% centrality because of jet broadening, if any, is expected to increase with centrality. We expect this uncertainty does not depend much on ϕ_s although the jet width is not a priori necessarily the same

over ϕ_s.

Given the above caveats in the systematic uncertainties, the 20-60% results shown in Figure 5.7 left panel may suggest that the near-side jet in the reaction plane direction interacts with the medium, losing energy and generating a sizeable ridge over a long $\Delta\eta$ range. The near-side jet perpendicular to the reaction plane suffers minimal interaction with the medium, with no significant ridge and with the correlated multiplicity only slightly higher than that in d + Au . The initial jet energy selected by the trigger particle is likely the highest at small ϕ_s and decreases with increasing ϕ_s, approaching that in d + Au . The results in the top 5% central collisions shown in Figure 5.7 right panel are qualitatively similar, but the variation with ϕ_s is much smaller, consistent with the more spherical collision geometry in central collisions.

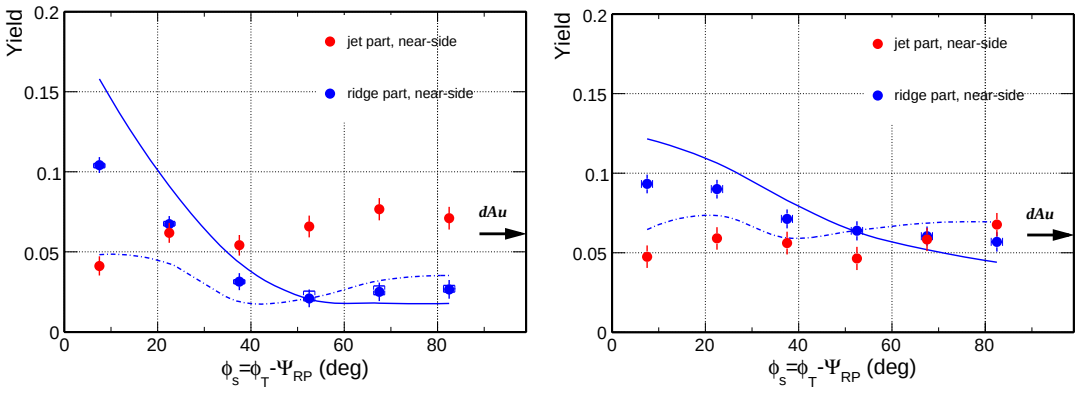

Figure 5.7: (color online) The di-hadron correlation total yield on the near-side ($|\Delta\phi| < 1.0$) for jet part (red) and ridge part (blue) as a function of trigger particle azimuthal angle from the event plane, $\phi_s = |\phi^{trig} - \Psi_{EP}|$. The systematic uncertainties on the ridge data due to the uncertainties of flow subtraction from v_2 and background level B are indicated by the curves and square brackets, respectively, while those on the jet data are small. The results are for $3 < p_T^{trig} < 4$ GeV/c and $1.5 < p_T^{assoc} < 2.0$ GeV/c in 20-60% (left) and top 5% (right) Au + Au collisions. The jet signal from d + Au data is indicated by the arrow on the right.

An interesting phenomena appears by taking the ridge yield from the two centrality bins together. This comparison is presented in Figure 5.8 as an example with one associated p_T bin of $1.5 < p_T^{assoc} < 2.0$ GeV/c for $3 < p_T^{trig} < 4$ GeV/c (left panel) and we

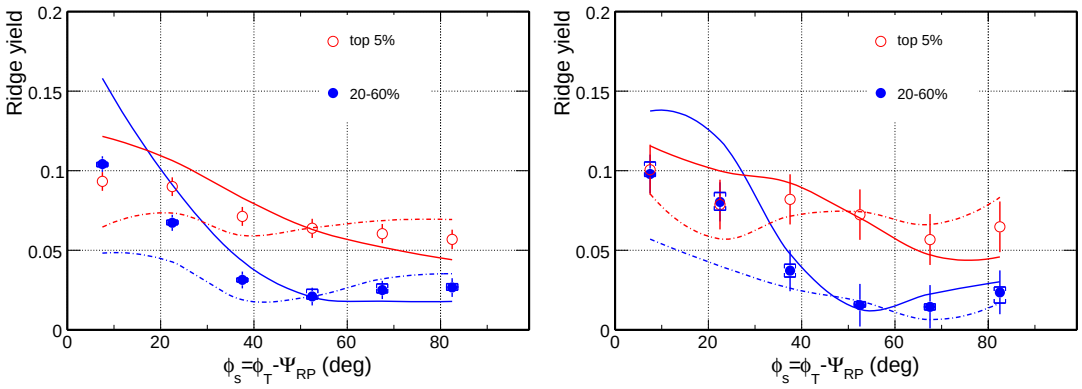

Figure 5.8: The comparison of ridge yield in two centrality bins. Blue and red circles are represented for 20-60% and top 5% results, respectively. The left plot is for $3 < p_T^{trig} < 4$ GeV/c, the right one is for $4 < p_T^{trig} < 6$ GeV/c. The p_T range for associated particles is $1.5 < p_T^{assoc} < 2.0$ GeV/c for both plots.

also compare the ridge yield for the higher trigger $4 < p_T^{trig} < 6$ GeV/c (right panel) . Both the results show that at the small ϕ_s ($0^\circ < \phi_s < 15^\circ$), the ridge yields are similar in these two centralities. As we know, the collision geometry is similar in the reaction plane direction but different in the direction perpendicular to the reaction plane, as shown in cartoon 5.9. So does the gluon density behave in the two directions between the two centralities. Naturally, one may imagine that the similar ridge yields in the two centrality bins may not be a coincidence, it may depend on the collision geometry or the gluon density. However, further evidences are needed to testify this thought.

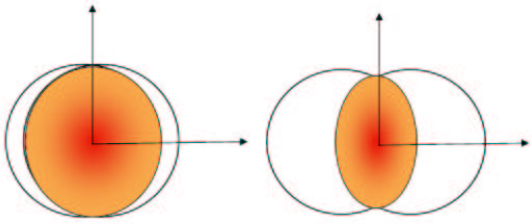

Figure 5.9: A cartoon of collision geometry in two centrality bins. The left cartoon shows the collision geometry for central collisions and the right one is for mid-central collisions.

CHAPTER 6

Summary and Outlook

In this thesis, we present the di-hadron azimuthal correlations in Au + Au collsions at $\sqrt{s_{NN}}$ =200 GeV from STAR experiment as a function of the trigger particle azimuthal angle from the event plane ($\phi_s = |\phi^{trig} - \Psi_{EP}|$) in six equal size slices. The background subtraction method is discussed in details. The flow correction is carried out to the order of $v_2 v_4$. The systematic uncertainties in the background subtraction are extensively discussed. The $|\phi^{trig} - \Psi_{EP}|$ dependences of the di-hadron correlation signals, as well as the trigger and associated p_T dependences, are studied. Both the mid-central 20-60% and the top 5% central Au + Au collisions are investigated. The minimum bias d + Au collision data are presented for baseline comparison. The correlation functions are also obtained from small and large $|\Delta\eta|$ regions separately, in attempt to isolate the jet and ridge contributions to the near-side correlation strength and study their behavior in $|\phi^{trig} - \Psi_{EP}|$.

The di-hadron correlations are strongly modified in Au + Au collisions with respect to minimum bias d + Au collisions. The modifications strongly depend on the trigger particle orientation relative to the event plane and evolve with associated p_T^{assoc}. No significant changes are observed as a function of the trigger particle p_T^{trig} in the measured range of $3 < p_T^{trig} < 6$ GeV/c. The qualitative trend of the correlation function with $|\phi^{trig} - \Psi_{EP}|$ appears similar in central and mid-central collisions; quantitatively, the $|\phi^{trig} - \Psi_{EP}|$ dependence of the correlation function is stronger in the middle central collisions. The p_T^{assoc} dependences of the correlation function are quantitatively similar in the two centrality selections.

The away-side correlation broadens from in-plane to out-of-plane, and broadens with increasing associated p_T^{assoc} for most $|\phi^{trig} - \Psi_{EP}|$ slices. For 20-60% Au + Au collisions, the away-side correlation for $|\phi^{trig} - \Psi_{EP}| < \pi/6$ is single-peaked, independent of p_T^{assoc}, and not much wider than d + Au , however, the amplitude is larger than the d + Au data. For $|\phi^{trig} - \Psi_{EP}| > \pi/6$, the away-side double-peak structure starts to develop and becomes stronger for increasing $|\phi^{trig} - \Psi_{EP}|$ and increasing p_T^{assoc}. For top 5% central Au + Au , the away-side correlation seems already double-peaked and quite different from d + Au in the first $|\phi^{trig} - \Psi_{EP}|$ slice, and becomes more strongly double-peaked with increasing $|\phi^{trig} - \Psi_{EP}|$ and increasing p_T^{assoc}. The away-side correlation widths for slice 6 are similar between 20-60% and top 5% centrality bins. The correlation amplitude at $\Delta\phi = \pi$ drops from in-plane to out-of-plane for both two centralities, and the correlation amplitude in the double-peak region remains constant over ϕ_s in both centralities but with higher amplitude in central collisions. The trends of the away-side modification underscore the importance of the path-length that the away-side parton transverses in the medium. The away-side medium path-length in the reaction plane direction in 20-60% Au + Au collisions is quite modest and not enough to generate significant modification to jet correlation, while that in the top 5% collisions is long enough to cause significant jet modification. The strongest modification is found for trigger particles perpendicular to the reaction plane where the away-side medium path-length is the longest, and this path-length appears to be not very different in 20-60% and top 5% Au + Au collisions.

The near-side correlation amplitude decreases with $|\phi^{trig} - \Psi_{EP}|$. The decrease comes entirely from the decrease in the long range $\Delta\eta$ correlation (ridge). The ridge yield decreases significantly with $|\phi^{trig} - \Psi_{EP}|$ in the 20-60% centrality, while significant ridge yields persist over all slices in top 5% collisions. The jet contribution to the near-side correlation is extracted from the difference of small and large $\Delta\eta$ correlations, subject to small experimental systematic uncertainties. The jet contribution in the 20-60% centrality appears to remain constant or somehow slightly increase from in-plane to out-

of-plane. The $\phi_s \simeq 90^\circ$ near-side correlation is found to be slightly larger than that measured in minimum bias d + Au collisions. The near-side jet parallel to the reaction plane appears to have suffered significant interactions with the medium, which reduces the real jet correlated multiplicity and produces a long range $\Delta\eta$ ridge containing a large number of hadrons. The near-side jet perpendicular to the reaction plane, on the other hand, appears to suffer minimal medium modification, generating small amount of ridge. The top 5% results are qualitatively similar, but the significant ridge contribution persists over all $|\phi^{trig} - \Psi_{EP}|$, and the variations of the jet and ridge magnitudes in $|\phi^{trig} - \Psi_{EP}|$ is significantly smaller, consistent with the more spherical collision geometry.

To summarize our main findings, in mid-central Au + Au collisions the di-jet parallel to the reaction plane suffers medium interactions on both the near- and away-side. The near-side interactions generate the long range $\Delta\eta$ ridge; the away-side interactions appear modest although perhaps stronger than the near-side. The di-jet perpendicular to the reaction plane fragments on the near-side with only slightly larger multiplicity than in d + Au with small amount of ridge generation, and on the away-side suffers maximal interactions with the medium generating strong double-peak correlation structure. The top 5% centrality shows smaller variations with $|\phi^{trig} - \Psi_{EP}|$ consistent with the more spherical geometry. The near-side ridge persists over all $|\phi^{trig} - \Psi_{EP}|$ slices, and the away-side correlation is significantly modified over all $|\phi^{trig} - \Psi_{EP}|$ and the modification increases with $|\phi^{trig} - \Psi_{EP}|$. At $|\phi^{trig} - \Psi_{EP}| \simeq 90^\circ$ the away-side correlations are similar between the two centralities consistent with similar away-side path-length. The similar near-side ridge yields at $|\phi^{trig} - \Psi_{EP}| \simeq 0^\circ$ in two centralities may suggest the dependence of the collision geometry or the gluon density since both of them are similar in the reaction plane direction in the two centralities.

The main results presented in this thesis are with $3 < p_T^{trig} < 4$ GeV/c. The results from trigger particles with higher p_T is necessary to check the results since they are more probably coming from jet fragmentation. In the future RHIC run with the TPC DAQ1000 upgrade, we are able to accumulate more than ten times statistics of the data

sample in Run IV, used in this thesis. It provides us the possibility of investigating the correlations with high p_T trigger particles in the future.

Due to the limited event plane resolutions, there must be some smearing in the correlation study: Some trigger particles should have come from some slice, here slice 2 for example, maybe miscount in slice 3 or 1. So the next step for correction of the limited event resolutions in correlation function is needed. And we have already attempted to do the corrections in some simple Monte-Carlo simulations.

APPENDIX A

Kinematic Variables

Let us introduce some useful kinematic variables that are commonly used in heavy ion physics.

For two body colliding system, the beam direction is usually defined as z-axis. And the p_T (transverse momentum) is defined as:

$$p_T = \sqrt{p_x^2 + p_y^2} \tag{A.1}$$

p_T is a Lorentz invariant variable since both p_x and p_y are unchanged under a Lorentz boost along z axis. For identified particles the transverse mass is defined as

$$m_T = \sqrt{p_T^2 + m^2} \tag{A.2}$$

where m is the particle mass and the transverse kinetic energy of the particle is $m_T - m$.

Another commonly used variable in heavy ion collisions is the rapidity, defined as

$$y = \frac{1}{2} \ln \left(\frac{E + p_z}{E - p_z} \right) \tag{A.3}$$

The rapidity is useful in that one can switch between reference frames along the z-axis and the only change in rapidity is an additive constant. If particle mass is much smaller than its momentum, it is convenient to use pseudorapidity η which is approximately the rapidity. The definition for pseudorapidity is,

$$\eta = \frac{1}{2} \ln \left(\frac{|\overrightarrow{p}| + p_z}{|\overrightarrow{p}| - p_z} \right) \tag{A.4}$$

APPENDIX B

Backup Figures

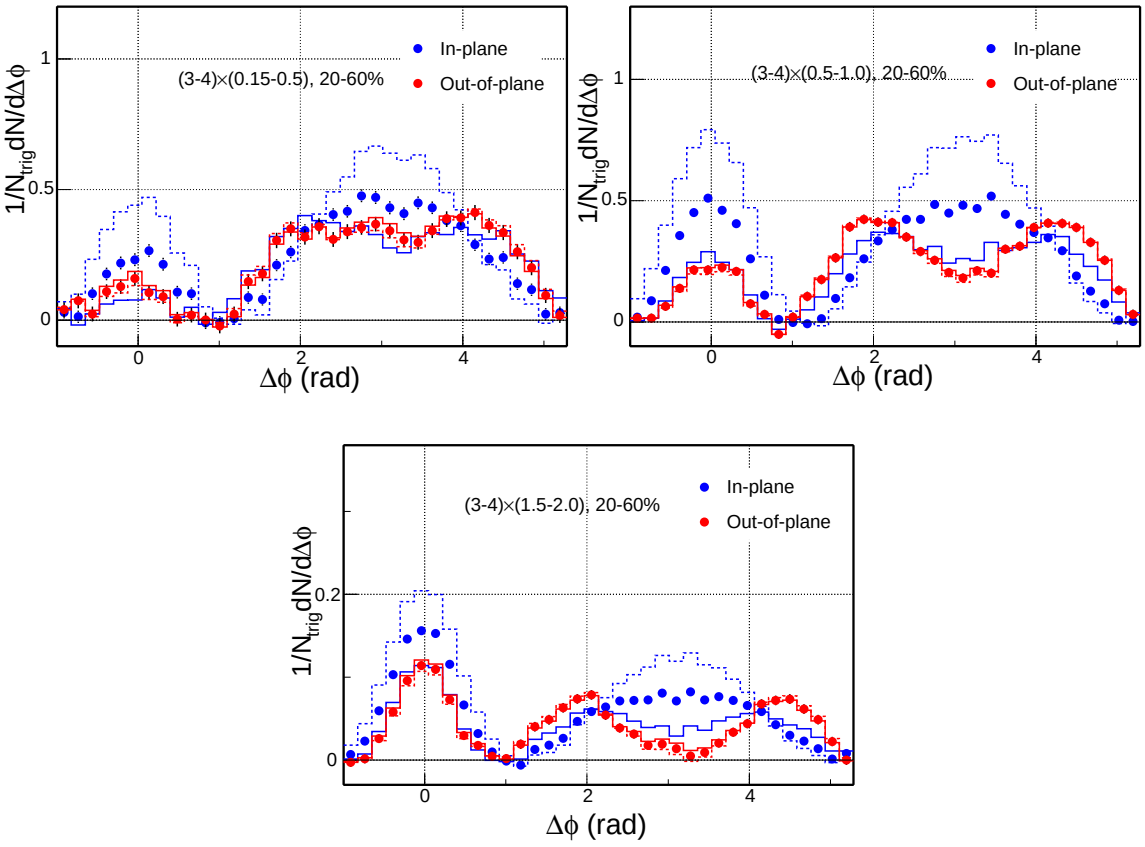

Figure B.1: (color online) Same as Figure 4.6 with $3 < p_T^{trig} < 4$ GeV/c in 20-60% Au + Au collisions, but for other 3 associated p_T ranges: $0.15 < p_T^{assoc} < 0.5$ GeV/c, $0.5 < p_T^{assoc} < 1.0$ GeV/c and $1.5 < p_T^{assoc} < 2.0$ GeV/c.

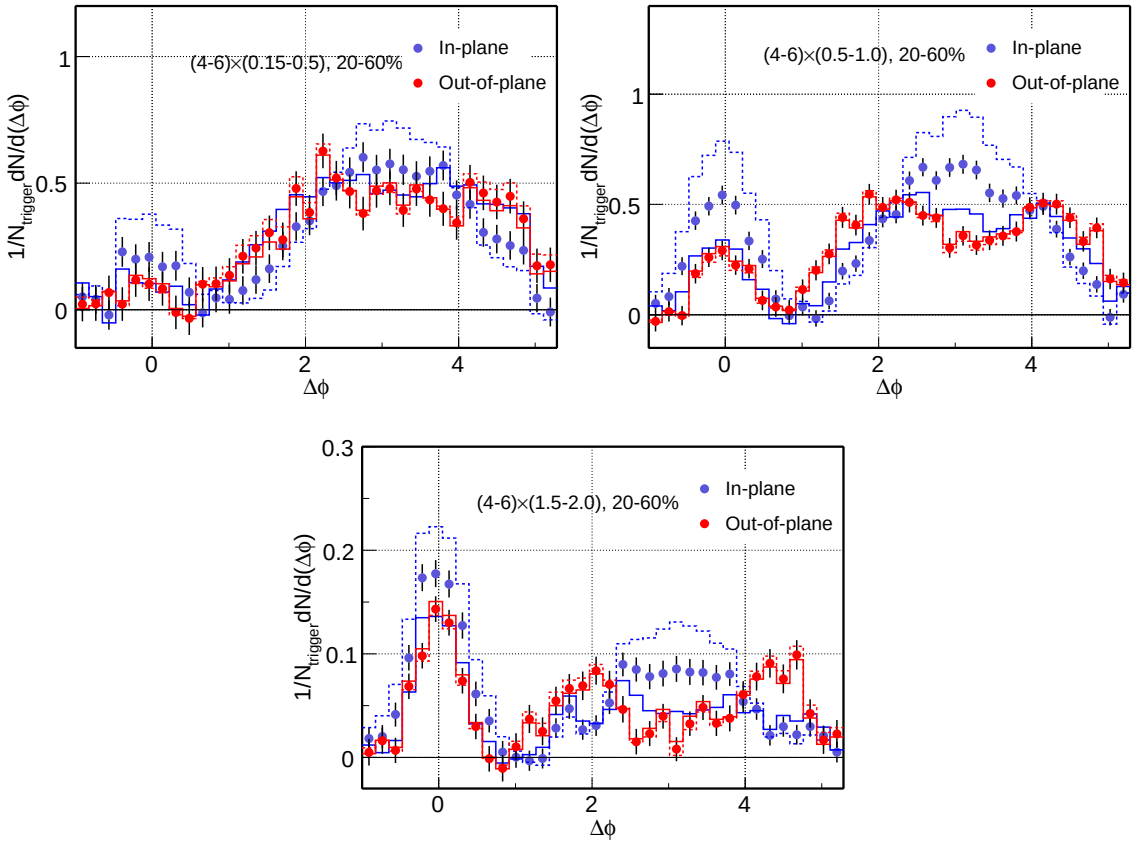

Figure B.2: (color online) Same as Figure 4.6 with $4 < p_T^{trig} < 6$ GeV/c in 20-60% Au + Au collisions, but for other 3 associated p_T ranges: $0.15 < p_T^{assoc} < 0.5$ GeV/c, $0.5 < p_T^{assoc} < 1.0$ GeV/c and $1.5 < p_T^{assoc} < 2.0$ GeV/c.

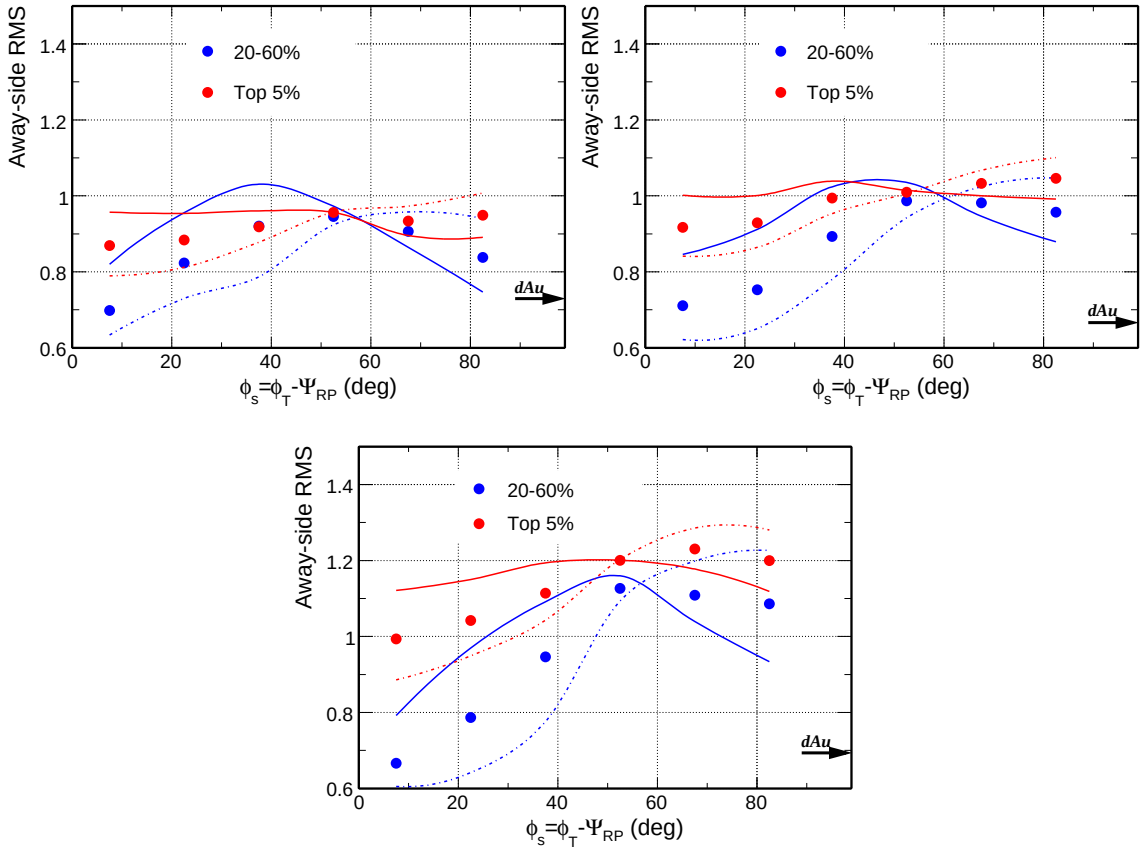

Figure B.3: (color online) Same as Figure 5.2 with $3 < p_T^{trig} < 4$ GeV/c in 20-60% Au + Au collisions, but for other 3 associated p_T ranges, from up to down, they are: $0.15 < p_T^{assoc} < 0.5$ GeV/c, $0.5 < p_T^{assoc} < 1.0$ GeV/c and $1.5 < p_T^{assoc} < 2.0$ GeV/c, respectively.

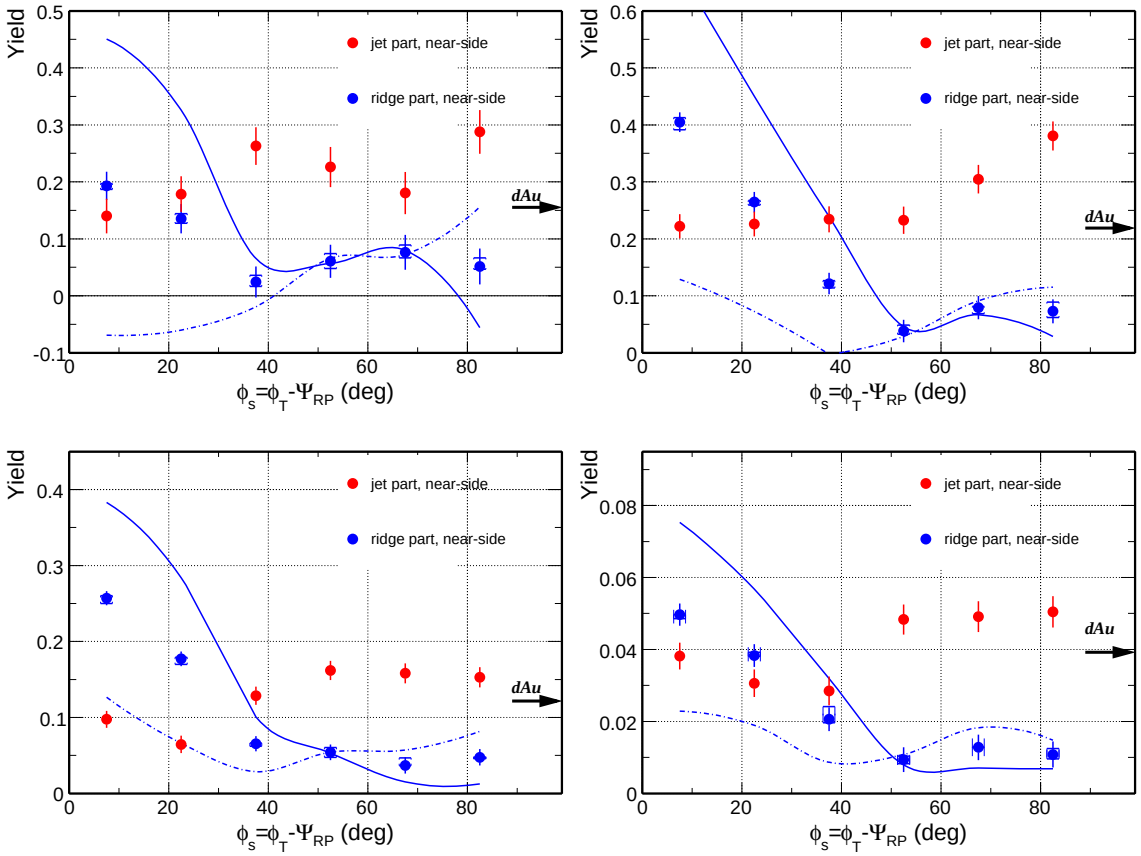

Figure B.4: (color online) Same as Figure 5.7 with $3 < p_T^{trig} < 4$ GeV/c in 20-60% Au + Au collisions, but for other 4 associated p_T ranges: $0.15 < p_T^{assoc} < 0.5$ GeV/c, $0.5 < p_T^{assoc} < 1.0$ GeV/c, $1.0 < p_T^{assoc} < 1.5$ GeV/c and $2.0 < p_T^{assoc} < 3.0$ GeV/c, respectively.

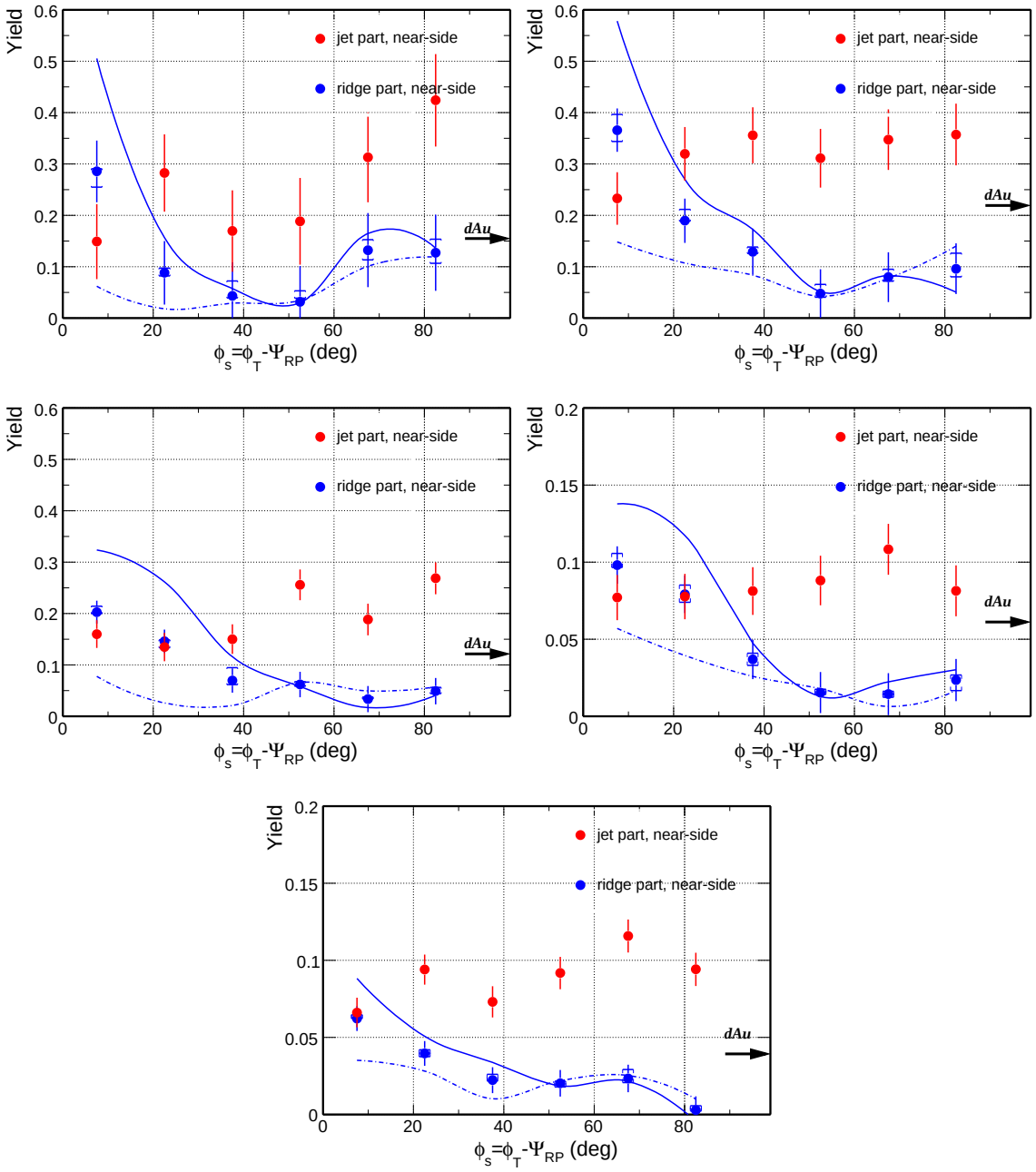

Figure B.5: (color online) Same as Figure 5.7 in 20-60% Au + Au collisions, but for $4 < p_T^{trig} < 6$ GeV/c and all associated p_T ranges: $0.15 < p_T^{assoc} < 0.5$ GeV/c, $0.5 < p_T^{assoc} < 1.0$ GeV/c, $1.0 < p_T^{assoc} < 1.5$ GeV/c, $1.5 < p_T^{assoc} < 2.0$ GeV/c and $2.0 < p_T^{assoc} < 34.0$ GeV/c, respectively.

References

[Abe06] B.I. Abelev et al. *Phys. Rev. Lett.*, **97**:252001, 2006.

[Abe07] B.I. Abelev et al. *Phys. Rev. Lett.*, **99**:112301, 2007.

[Ada03] J. Adams et al. *Phys. Rev. Lett.*, **91**:072304, 2003.

[Ada04a] J. Adams et al. *Phys. Rev. Lett.*, **92**:112301, 2004.

[Ada04b] J. Adams et al. *Phys. Rev. Lett.*, **92**:052302, 2004.

[Ada04c] J. Adams et al. *Phys. Rev. Lett.*, **93**:252301, 2004.

[Ada05a] J. Adams et al. *Phys. Lett. B*, **612**:181, 2005.

[Ada05b] J. Adams et al. *Phys. Rev. Lett.*, **95**:152301, 2005.

[Ada05c] J. Adams et al. *Phys. Rev. C*, **72**:014904, 2005.

[Ada05d] J. Adams et al. "STAR white paper." *arXiv: nucl-ex/0501009*, 2005.

[Adc04] K. Adcox et al. "PHENIX white paper." *arXiv: nucl-ex/0410003*, 2004.

[Adl02a] C. Adler et al. *Phys. Rev. Lett.*, **89**:202301, 2002.

[Adl02b] C. Adler et al. *Phys. Rev. C*, **66**, 2002.

[Adl04] S.S. Adler et al. *arXiv: nucl-ex/0409015*, 2004.

[And03] M. Anderson et al. *Nucl. Instr. Meth. A*, **499**:659, 2003.

[App98] H. Appelshäuser et al. *Phys. Rev. Lett.*, **80**:4136, 1998.

[Arm04] N. Armesto et al. *Phys. Rev. Lett.*, **93**:242301, 2004.

[Bar97a] J. Barrette et al. *Phys. Rev. C*, **55**:1420, 1997.

[Bar97b] J. Barrette et al. **56**:3254, 1997.

[Bea04] I.G. Bearden et al. *Phys. Rev. Lett.*, **93**:102301, 2004.

[Bie04] J. Bielcikova et al. *Phys. Rev. C*, **69**:021901, 2004.

[Bjo83] J.D. Bjorken. *Phys. Rev. D*, **27**:140, 1983.

[Bra01] P. Braun-Munzinger. *Nucl. Phys. A*, **681**:119c, 2001.

[Cas04] J. Castilllo et al. *J. Phys. G*, **30**:S1207, 2004.

[Cat93] S. Catani et al. *Nucl. Phys. B*, **406**:187, 1993.

[DKS03] G. Dissertori, I. Knowles, and M. Schmelling. *Quantum Chromodynamics - High Energy Experiments and Theory*. Oxford University Press, 2003.

[FK02] Z. Fodor and S.D. Katz. *J. High Energy Phys.*, **0203**:014, 2002.

[Gup98] R. Gupta. *arXiv: hep-lat/9807028*, 1998.

[Hwa05] R.C. Hwa and C.B. Yang. *Phys. Rev. C*, **72**:034903, 2005.

[Kar02a] F. Karsch. *Lect. Notes Phys.*, **583**:209, 2002.

[Kar02b] F. Karsch. *Nucl. Phys. A*, **698**:199, 2002.

[KH03] P.F. Kolb and U. Heinz. *arXiv: nucl-th/0305084*, 2003.

[KLP00] F. Karsch, E. Laermann, and A. Peikert. *Phys. Lett. B*, **478**:447, 2000.

[KSH00] P. Kolb, J. Sollfrank, and U. Heinz. *Phys. Rev. C*, **62**:054909, 2000.

[Lin96] Z. Lin. Ph.D. Thesis, Columbia University, 1996.

[LK02] Z. Lin and C.M. Ko. *Phys. Rev. Lett.*, **89**:202302, 2002.

[Ma06] G.L. Ma et al. *arXiv: nucl-th/0608050*, 2006.

[Maj04] A. Majumder et al. *Phys. Rev. Lett.*, **99**:042301, 2004.

[MV03] D. Molnar and S.A. Voloshin. *Phys. Rev. Lett.*, **91**:092301, 2003.

[Pic95] A. Pich. *arXiv: hep-ph/9505231*, 1995.

[Pos05] A. Poskanzer. *Talk at STAR Collaboration Meeting*, 2005.

[Put07] J. Putschke. *J. Phys. G*, **34**:S679, 2007.

[PV98] A. M. Poskanzer and S. A. Voloshin. *Phys. Rev. C*, **58**:1671, 1998.

[Rak04] J. Rak et al. *J. Phys. G*, **30**:S1309, 2004.

[Sat00] H. Satz. *Rep. Prog. Phys.*, **63**:1511, 2000.

[Sha06] M. Shao et al. *Nucl. Instr. Meth. A*, **558**:419, 2006.

[Sor99] H. Sorge. *Phys. Rev. Lett.*, **82**:2048, 1999.

[Sor03] P.R. Sorensen. Ph.D. Thesis, UC Los Angeles, 2003. arXiv: nucl-ex/0309003.

[SSH93] E. Schnedermann, J. Sollfrank, and U. Heinz. *Phys. Rev. C*, **48**:2462, 1993.

[Ule06] J. Ulery. *arXiv: nucl-ex/0609047*, 2006.

[Ule07] J. Ulery. Ph.D. Thesis, Purdue University, 2007.

[VP00] S. A. Voloshin and A. M. Poskanzer. *Phys. Lett. B*, **474**:27, 2000.

[Vol06] S. A. Voloshin. *Phys. Lett. B*, **632**:490, 2006.

[VZ96] S. Voloshin and Y. Zhang. *Z. Phys. C*, **70**:665, 1996.

[Wan91] S. Wang et al. *Phys. Rev. C*, **44**:1091, 1991.

[Won94] C.-Y. Wong. *Introduction to High-Energy Heavy-Ion Collisions*. World Scientific Publishing Co. Pte. Ltd., 1994.

[Won07] C.-Y. Wong. *arXiv: hep-ph/0712.3282*, 2007.

[Yao06] W.-M. and Yao. "Review of Particle Physics." *Journal of Physics G*, **33**:1+, 2006.

Presentations and publication List

Presentations

1. Away-side Modification and Near-side Ridge Relative to Reaction Plane at RHIC.

   X National Particle Physics Meeting, Nanjing, China, April 24-29, 2008.

2. Away-side Modification and Near-side Ridge Relative to Reaction Plane.

   20th International Conference on Nucleus Nucleus Collisions (Quark Matter 2008), Jaipur, India, Feb. 4-10, 2008

3. Di-Hadron Azimuthal Correlations Relative to the Reaction Plane.

   2007 APS April Meeting, Jacksonville, USA, April 14-17, 2007.

4. Measurements of Charge Fluctuation in High Energy Collisions (in Chinese)

   IX National Particle Physics Meeting, Chongqing, China, May 9-13, 2005.

5. Recent Measurements of Charge Fluctuations in Nuleonic and Nuclear Collisions

   XI Vietnam School of Physics, Danang, Vietnam, Dec. 27, 2004 - Jan. 7, 2005.

Publication list

1. **Aoqi Feng** (for the STAR Collaboration), "Away Side Modification and Near Side Ridge Relative to the Reaction Plane". QM2008 proceedings, to be published in *J. Phys. G.*

2. **Aoqi Feng**, Na Li, Jinghua Fu and Yuanfang Wu. "Rapidity Dependence of Charge Fluctuations and Correlations in Hadronic and Nuclear Collisions", *Int. J. Mod. Phy. A*, **22** 2909, 2007.

3. **Aoqi Feng**, Yuanfang Wu. "Measures of Charge Fluctuation in High Energy Collisions", *High Energy Physics and Nuclear Physics* (in Chinese), Vol. **29 (08)** 766, 2005.

4. B.I. Abelev *et al.*, STAR Collaboration. "Forward Λ Production and Nuclear Stopping Power in d + Au Collisions at $\sqrt{s_{NN}}$ = 200 GeV", *Phys. Rev. C*, **76** 064904, 2007.

5. B.I. Abelev *et al.*, STAR Collaboration. "Measurement of Transverse Single-Spin Asymmetries for Di-Jet Production in Proton-Proton Collisions at $\sqrt{s}$ = 200 GeV ", *Phys. Rev. Lett.*, **99** 142003, 2007.

6. B.I. Abelev *et al.*, STAR Collaboration. "Global Polarization Measurement in Au + Au collisions", *Phys. Rev. C*, **76** 024915, 2007.

7. B.I. Abelev *et al.*, STAR Collaboration. "Energy Dependence of π, p and $\bar{p}$ Transverse Momentum Spectra for Au + Au Collisions at $\sqrt{s_{NN}}$ = 62.4 and 200 GeV", *Phys. Lett. B*, **655** 104, 2007.

8. B.I. Abelev *et al.*, STAR Collaboration. "Patonic Flow and ϕ-meson production in Au + Au collisions at $\sqrt{s_{NN}}$ = 200 GeV", *Phys. Rev. Lett.*, **99** 112301, 2007.

9. B.I. Abelev *et al.*, STAR Collaboration. "Strangelet Search in Au + Au Collisions at 200 GeV", *Phys. Rev. C*, **76** 011901, 2007.

10. B.I. Abelev *et al.*, STAR Collaboration. " Transverse Momentum and Centrality Dependence of High-p_T Nonphotonic Electron Suppression in Au+Au Collisions at $\sqrt{s_{NN}}$ = 200 GeV", *Phys. Rev. Lett.*, **98** 192301, 2007.

Acknowledgements

Please permit me to give my faithful appreciations to all peoples who give me a lot of help during my PhD reseach!

Firstly, I would like to thank Professor Lianshou Liu who guides me to enter the holy palace of high energy physics. From him, I got the basic physics knowledge and the determination to continue studying physics. I am grateful for the chance he provides me to start my high energy physics career and the continuous support he gives me on my master and Ph.D researches.

I'm grateful my supervisors Professor Yuanfang Wu and Professor Fuqiang Wang. Without their help, this thesis would never come out in this present form. Fang first led me to know how to do science research work. Fuqiang guides me to do some more detailed research work and let me know how to do a serious research. Many thanks to his guide, detailed discussions, help and big support. Their punctilious spirits and wholehearted attitudes towards science will be encouraging me all the time!

Many thanks to Professor Nu Xu. Students may think he is a strict teacher, but on the back of his strictness what I see are his love and hope to the students. I will never forget his support and kind concern on my study and life.

Thanks to Professor Feng Liu, a kind and patient teacher. He gives students a lot of opportunities to begin their study on computer and heavy ion physics.

Thanks Gang Wang for his rich discussions and friendship. And I am also grateful Professor Huanzhong Huang for his encouragement.

Thanks all the people in Purdue heavy ion physics group and LBL RNC group.

Thanks Jason Ulery, Terry Tarnowsky, Brijesh Srivastava, Rolf Scharenberg, Mike Skoby, Pawan Netrakanti, Andrew Hirsch, Guoliang Ma, Quan Wang, Grazyna Odyniec, Ernst Sichtermann, Hans Georg Ritter, Art Postkanzer, Vinham Tram, Xiangming Sun, Xinghua Shi, Qinhua Xu, Wei Zhou, Zebo Tang and Yichun Xu. Thanks them for the

fruitful discussions and the happy time we spent together.

Thanks spectra physics working group and the convenors, Bendanga Mohanty and Olga Barannikova.

Thanks also go to every member of the STAR collaboration.

Thanks all the teachers and students in IOPP. Thanks Zhiming Li to help me face the difficulties on charge correlation study. Thanks Zhixu Liu to teach me how to solve problems on codes. Thanks Mingmei Xu, Xiaoyan Lin, Xiuwen Xing, Yan Lv, Meiling Yu, Yanping Huang, Na Li, Kejun Wu, Jiayun Chen, Meijuan Wang, Jiaxin Du, You Zhou, Hongwei Ke, Ling Yu, Fei Xie, Lin Li, Lizhu Chen for their friendship.

Finally, I'd like to thank my dear father and mother for their supports all the time. They are the best parents in the world. Thousands thanks can not express my appreciations. I would also like to give my special thanks to my fiance Xin Dong who has been giving me a lot of courage when I am depressed or sad and bringing me plenty of happiness. Thanks his brightness, broad breast, concern, understanding and support. Thanks also to my brother Jie Dong for his support on the back and the share of my happiness and sadness.